FINAL TECHNICAL REPORT

on

FRETTING CORROSION IN AIRFRAME RIVETED AND PINNED CONNECTIONS

(Grant No. F49620-93-1-0488)

by

George T. Hahn and Carol A. Rubin

Department of Mechanical Engineering
Vanderbilt University
Nashville, Tennessee 37235

March 20, 1998

DISTRIBUTION STATEMENT A
Approved for public release;
Distribution Unlimited

Submitted To

Air Force Office of Scientific Research
110 Duncan Avenue, Suite B115
Bolling AFB, DC 20332-0001

DTIC QUALITY INSPECTED 3

19980421 153

Approved for public release,
distribution unlimited

AFRL-SR-BL-TR-98-

0339

REPORT DOCUMENTATION PAGE

Public reporting burden for this collection of information is estimated to average 1 hour per response, including the time for reviewing instructions, searching existing data sources, gathering and maintaining the data needed, and completing and reviewing the collection of information. Send comments regarding this burden estimate or any other aspect of this collection of information, including suggestions for reducing this burden, to Washington Headquarters Services, Directorate for Information Operations and Reports, 1215 Jefferson Davis Highway, Suite 1204, Arlington, VA 22202-4302, and to the Office of Management and Budget, Paperwork Reduction Project (0704-0188), Washington, DC 20503.

1. AGENCY USE ONLY *(Leave blank)*	2. REPORT DATE	3. REPORT TYPE AND DATES COVERED
	20 March 1998	Final Technical 1 Aug. 93 - 31 Jul. 97

4. TITLE AND SUBTITLE	5. FUNDING NUMBERS
Fretting Corrosion in Airframe Riveted and Pinned Connections	G F49620-93-1-0488
6. AUTHORS George T. Hahn and Carol A. Rubin	
7. PERFORMING ORGANIZATION NAME(S) AND ADDRESS(ES) Department of Mechanical Engineering Box 1592, Station B Vanderbilt University Nashville, TN 37235	8. PERFORMING ORGANIZATION REPORT NUMBER
9. SPONSORING/MONITORING AGENCY NAME(S) AND ADDRESS(ES) Air Force Office of Scientific Research 110 Duncan Ave., Suite B115 Bolling A.F.B., D.C. 20332-0001	10. SPONSORING/MONITORING AGENCY REPORT NUMBER

11. SUPPLEMENTARY NOTES

12a. DISTRIBUTION/AVAILABILITY STATEMENT	12b. DISTRIBUTION CODE
Approved for public release, distribution unlimited	

13. ABSTRACT *(Maximum 200 words)*

This 4-year, URI-Initiation project examined the fretting and corrosion response of multiple rivet, one and two rivet-row, lap joints. Tribological parameters governing fretting as well as the effects of intereference and clamping on fretting wear and fretting fatigue have been evaluated using 2-D and 3-D finite element analyses. A piezoelectrically-driven fretting wear machine that can simulate the fretting conditions in connections has been constructed. In this way the specific fretting wear rates of 7075-T6 and 2024-T3 in contact with aluminum and hardened steel under dry and corrosive conditions have been measured. Finally, small, one-rivet-row and 2-rivet-row lap joints have been cyclically tested under dry and corrosive conditions and examined for fretting damage.

14. SUBJECT TERMS	15. NUMBER OF PAGES
Fatigue, fretting corrosion, wear, lap joint, riveted/joint, rivet, butt joint countersunk rivet, cyclic loading finite element analysis	167
	16. PRICE CODE

17. SECURITY CLASSIFICATION OF REPORT	18. SECURITY CLASSIFICATION OF THIS PAGE	19. SECURITY CLASSIFICATION OF ABSTRACT	20. LIMITATION OF ABSTRACT
unclassified	unclassified	unclassified	UL

NSN 7540-01-280-5500 Computer Generated STANDARD FORM 298 (Rev 2-89)
Prescribed by ANSI Std 239-18
298-102

DTIC QUALITY INSPECTED 8

FINAL TECHNICAL REPORT

on

FRETTING CORROSION IN AIRFRAME RIVETED AND PINNED CONNECTIONS

(Grant No. F49620-93-1-0488)

by

George T. Hahn and Carol A. Rubin

Department of Mechanical Engineering
Vanderbilt University
Nashville, Tennessee 37235

March 20, 1998

Submitted To

Air Force Office of Scientific Research
110 Duncan Avenue, Suite B115
Bolling AFB, DC 20332-0001

FINAL TECHNICAL REPORT
on

FRETTING CORROSION IN AIRFRAME RIVETED AND PINNED CONNECTIONS

(Grant No. F49620-93-1-0488)

by

George T. Hahn and Carol A. Rubin
Department of Mechanical Engineering
Vanderbilt University
Nashville, Tennessee 37235

ABSTRACT

This 4-year, URI-Initiation project on fretting corrosion terminated July 31, 1997. The project examined the basic mechanics and tribological, and corrosion response of multiple rivet, one and two rivet-row, lap joints. 2-D and 3-D finite element analyses of the joint have been used to calculate the tribological parameters governing fretting as well as the effects of intereference and clamping on fretting wear and fretting fatigue parameters. A piezoelectrically-driven fretting wear machine that can simulate the fretting conditions in connections has been constructed. In this way the specific fretting wear rates of 7075-T6 and 2024-T3 in contact with aluminum and hardened steel under dry and corrosive conditions have been measured. Finally, small, one-rivet-row and 2-rivet-row lap joints have been cyclically tested under dry and corrosive conditions and examined for fretting damage.

TABLE OF CONTENTS

Page

1. PROJECT SCOPE 4

2. EXECUTIVE SUMMARY 5

   2.1 Finite Element Analyses of One and Two Rivet-Row Lap Joints ... 5
   2.2 Location of Fatigue and Fretting Critical Regions and the Effects of Interference and Clamping 5
   2.3 Analyses of Fretting Fatigue Lives 10
   2.4 Piezoelectric-Actuated Fretting Wear Machine 11
   2.5 Specific Fretting Wear Rates of Airframe Materials 11
   2.6 Cyclic Loading Test of Laboratory-Scale Riveted Lap Joints Under Dry and Accelerated Corrosion 11

3. CONCLUSIONS 15

4. REFERENCES 16

5. PROJECT STAFF 17

6. PROJECT PUBLICATIONS 17

7. PATENT DISCLOSURE 18

8. APPENDICES 19

   APPENDIX A: K. Iyer, P. C. Bastias, C. A. Rubin and G. T. Hahn, "Influence of Interference and Clamping on Fretting Fatigue in Aluminum, Single Rivet-Row Lap Joints; Part I: Non-Countersunk Rivet"
   APPENDIX B: K. Iyer, P. C. Bastias, C. A. Rubin and G. T. Hahn, "Influence of Interference and Clamping on Fretting Fatigue in Aluminum, Single Rivet-Row Lap Joints; Part 2: Countersunk Rivet"
   APPENDIX C: M. Xue, J. Wert, P. Bastias and G. Hahn, "A Piezoelecric-Actuated Fretting Wear Machine"
   APPENDIX D: M. Xue, J. Wert, P. Bastias and G. Hahn, " Fretting Corrosion of 2024-T3 Aluminum Alloy"
   APPENDIX E: M. Xue, J. Wert, P. Bastias and G. Hahn, "Fretting Corrosion of 7075-T3 Aluminum Alloy"

1. PROJECT SCOPE

The project had 2 general objectives. One was to generate analytical and experimental capabilities for treating fretting in riveted connections. The second was to assess the contributions of fretting to the corrosive deterioration of aging airframes. To accomplish this, the drivers for fretting wear and frettiing fatigue in riveted connections were calculated and the specific fretting wear rates of aluminum alloy under the appropriate conditions were measured. These quantities provide a basis for predicting the fretting wear damage in the riveted connection. Such predictions have been compared with tests on laboratory-size, 1-rivet-row and 2-rivet-row lap joints.

The work drew on the advances of a second, concurrent AFOSR Project (F49620-93-1-0268) which devised 2D and 3D finite element analyses of cyclically loaded, one rivet-row, and two rivet-row lap joints have been devised. The present project employed these analyses to evaluate the mechanical features controlling fretting damage. These include the contact pressures at the rivet-panel and panel-panel interfaces, the local slip amplitudes and the tangential cyclic tensile stresses. The effects of interference and clamping on these features and on the drivers for fretting wear and fretting fatigue were also calculated.

The combined effects of the fretting drivers can be expressed approximately by F_1 and F_2:

Fretting wear; depth of the wear scar, $y = N (W_S / \mu) F_1$
Fretting fatigue; the cyclic life, $N_f = f(1/F_2)$

where: F_1 (fretting wear parameter) = $\mu \cdot p \cdot \delta$; F_2 (fretting fatigue parameter) = $F_1 \cdot \sigma$; μ is the coefficient of friction, p is the contact pressure, δ is the slip amplitude, W_S is the specific fretting wear rate, N is the number of fretting cycles and N_f is the fretting fatigue life. The quantities: p, δ, and σ were derived from the finite element analyese; μ and W_S from the measurements. Alternatively, the stress fields defined by the finite element analyses could be inserted into the more detailed analysis of fretting fatigue currently being developed with AFOSR support by Farris and coworkers at Purdue University. The quantity W_S, the specific fretting wear rate, depends on the nature of the contacting material, the slip amplitude and the corrosive environment.

A piezoelectrically-driven fretting wear machine that can simulate the fretting conditions in connections has been constructed. The machine has been used to measure the friction coefficients and the specific fretting wear rates of 7075-T6 and 2024-T3 in contact with aluminum and hardened steel under dry and corrosive conditions. Finally, small, one-rivet-row and 2-rivet-row lap joints have been cyclically tested under dry and corrosive conditions and examined for fretting damage.

The analyses developed here identify the locations and the local conditions reponsible for fatigue and fretting damage. They advance the understanding of the mechanisms of failure of lap joints and their performance and point to the locations where sensitive NDE can detect early signs of damage. Finally, the modelling provides a tool for optimizing the design of joints and rivets.

2. EXECUTIVE SUMMARY

2.1 Finite Element Analyses of One and Two Rivet-Row Lap Joints

The analysis of a riveted lap joint is a complex, 3-dimensional problem which has only recently become tractable with advanced computational facilities. The only other 3-D analyses of riveted connections reported thus far were performed by Fung and Smart (4.1) in Britain contemporary with the work of this project. This project drew on the advances made by a second AFOSR project (F49620-93-1-0268) which developed a more refined 2-D model and several 3-D models of a one and two rivet-row lap joints with conventional and countersunk rivet heads (4.2-4.10). The 2-D model is valid representation of a butt joint with stiff pins. The 3-D models treat the out-of-plane bending and rivet tilting that accompany the loading of a lap joint and which have important consequences for both fatigue and fretting. Results showing the bending, tilting and the distribution of stress in lap joints are presented in Figure 1 and Table 1 (4.7-4.10). Fung and Smart report the stresses generated in the rivet and panels of a 1-rivet-row lap joint, but have not examined the mechanical parameters that promote the fretting of a cyclically loaded connection (4.1). These were evaluated by the present project for the first time and include the local contact pressures and slip amplitudes at the rivet panel and panel-panel interfaces and the adjacent, tangential, cyclic stresses as well as the values of F_1. and F_2. These quantities not only depend on load and the rivet and joint geometry, but also on the amounts of interface friction, interference and clamping.

2.2 Location of Fatigue and Fretting Fatigue Critical Regions and the Effects of Interference and Clamping

The finite element calculations (see Appendix A and B) identify the 3 general sites for fretting fatigue identified in Figure 2. Examples of the variations of the local contact pressure, slip amplitude, the cyclic stress ajacent to the interface and F_2 at location A are illustrated in Figure 3. Figure 4 shows examples of fretting fatigue in locations A. Figures 3a and 3b, for a single rivet-row lap joint, illustrate the effects of interference and clamping on the variations of the in-plane contact pressure and slip with angular location and depth (t). The effects of interference and clamping on $\Delta\sigma$ and F_2, the drivers for conventional, in-plane fatigue and fretting fatigue (at the rivet-panel interface) are shown in Table 1 (see entries 5,6 and 7, and also 13 and 14) and Figure 3b and 3c. An example of this type of fretting fatigue is shown in Figure 4a. Qualitatively similar results are obtained for the 2 rivet-row joint. Other findings are listed below; those with design implications are printed in italics:

(i) The quantities: $\Delta\sigma$, p, δ, and F_2 display gradients in the out-of-plane direction (Figure 3a). The drivers for fatigue and fretting usually peak at the interior panel-panel interface because of panel bending (see Figure 1).

(ii) *The angular locations of the fatigue critical regions depend on the contribution of*

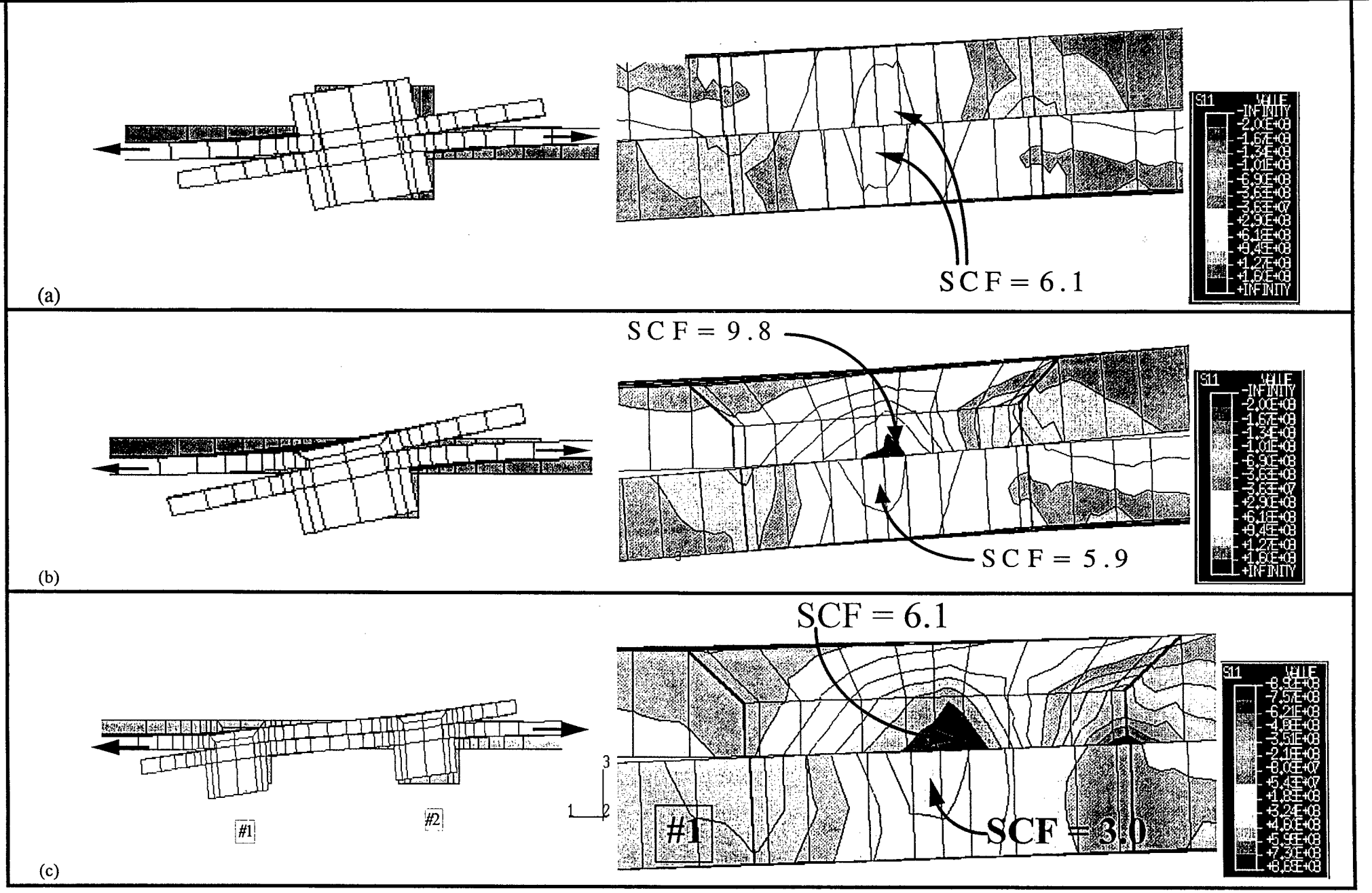

Figure 1. Results of finite element calculations of the distortion and local panel stresses of riveted lap joints: (a) single rivet-row with conventional rivets, (b) single rivet-row with countersunk rivets and (c) double rivet-row with countersunk rivets. Displacements are magnified 3x. The contour plots on the right describe the σ_{11} - stress field and identify the (peak) stress concentration factor (SCF) and its physical location.

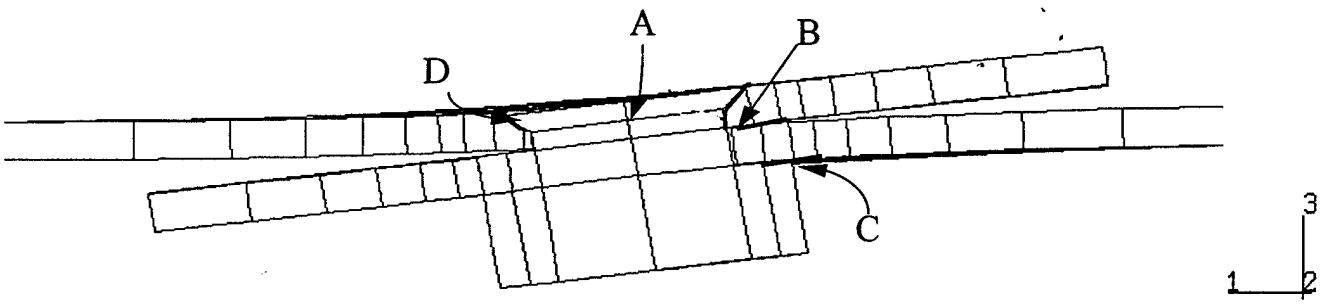

Figure 2. Regions of the joint interfaces where contact pressure and slip are combined with cyclic tension favorable for fretting fatigue: (A) rivet shank-panel interface (near the $\theta = 0°$ and $\theta = 180°$ angular locations) and (B) panel-panel interface where the edge of the lower panel hole rubs against the upper panel. Contact in regions (C) and (D) is attended by low values of cyclic tension and produce only fretting wear.

Table 1. SUMMARY OF PEAK STRESS CONCENTRATIONS AND THEIR ANGULAR LOCATIONS

#	Joint Type	μ	% Interference (I) and Clamping (C)	Tensile SCF	
				value	θ range , °
1	Single rivet-row with non-countersunk aluminum rivets	0.4	0 I, 0 C	5.3	-14.9° to 8.6°
2	Single rivet-row with non-countersunk aluminum rivets	0.4	1 I, 0 C	4.3	4.3° to 8.6°
3	Single rivet-row with non-countersunk aluminum rivets	0.4	1 I, 0.5 C	4.1	4.3° to 8.6°
4	Single rivet-row with countersunk (100°, 1/2 panel depth) steel rivets	0.2	0 I, 0 C	8.8*	-13.5° to 11.2°
5	Single rivet-row with countersunk (100°, 1/2 panel depth) aluminum rivets	0.4	0 I, 0 C	5.8	-11.4° to 5.4°
6	Single rivet-row with countersunk (100°, 1/2 panel depth) aluminum rivets	0.4	1 I, 0 C	5.0	8.7° to 22.5°
7	Single rivet-row with countersunk (100°, 1/2 panel depth) aluminum rivets	0.4	2 I, 0.5 C	4.3	15.6° to 22.5°
8	Single rivet-row with countersunk (61.6°, full panel depth) aluminum rivets	0.2	0 I, 0 C	10.5*	-17.4° to 5.4°
9	Single rivet-row with countersunk (100°, full panel depth) aluminum rivets	0.2	0 I, 0 C	12.1*	-12.7° to 0°
10	Double rivet-row with non-countersunk aluminum rivets	0.2	0 I, 0 C	4.4*	-10.9° to 6.2°
11	Double rivet-row with countersunk (100°, 1/2 panel depth) aluminum rivets	0.2	0 I, 0 C	6.1*	-15.6° to 9.8°
12	Double rivet-row with countersunk (100°, 1/2 panel depth) steel rivets	0.2	0 I, 0 C	5.9*	-13.2° to 10.7°
13	Double rivet-row with countersunk (100°, 1/2 panel depth) aluminum rivets	0.4	0 I, 0 C	5.6	-15.6° to -4.3°
14	Double rivet-row with countersunk (100°, 1/2 panel depth) aluminum rivets	0.4	1 I, 0 C	5.0	4.3° to 15.6°

* value obtained from elastic calculation. The remaining values are obtained from elastic-plastic calculations

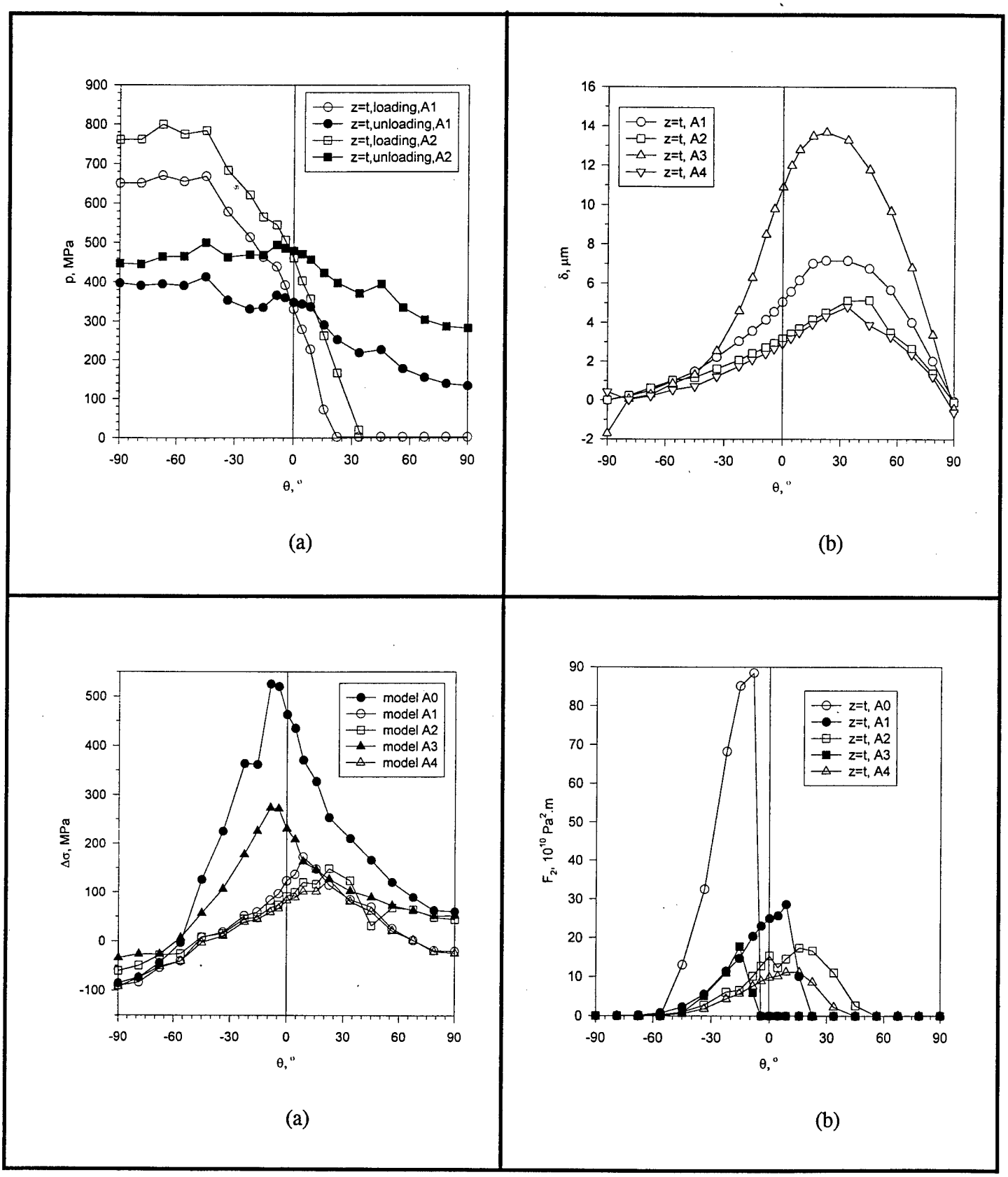

Figure 3. Effects of interference and clamping on the contact conditions and fatigue and fretting drivers at the rivet shank-panel interface of a lap joint (at the depth of the interior panel interface) including the angular variation of: (a) contact pressure, p, (b) slip amplitude, δ, (c) panel hole circumferential stress range, Δσ, and (d) fretting fatigue parameter, F_2. The curves were obtained for a single rivet-row joint with conventional, non-countersunk rivet heads for 5 combinations of interference (I) and clamping (C): (A0) I = 0%, C = 0%; (A1) I = 1%, C = 0%; (A2) I = 2%, C = 0%; (A3) I = 0%, C = 0.5%; (A4) I = 1%, C = 0.5%.

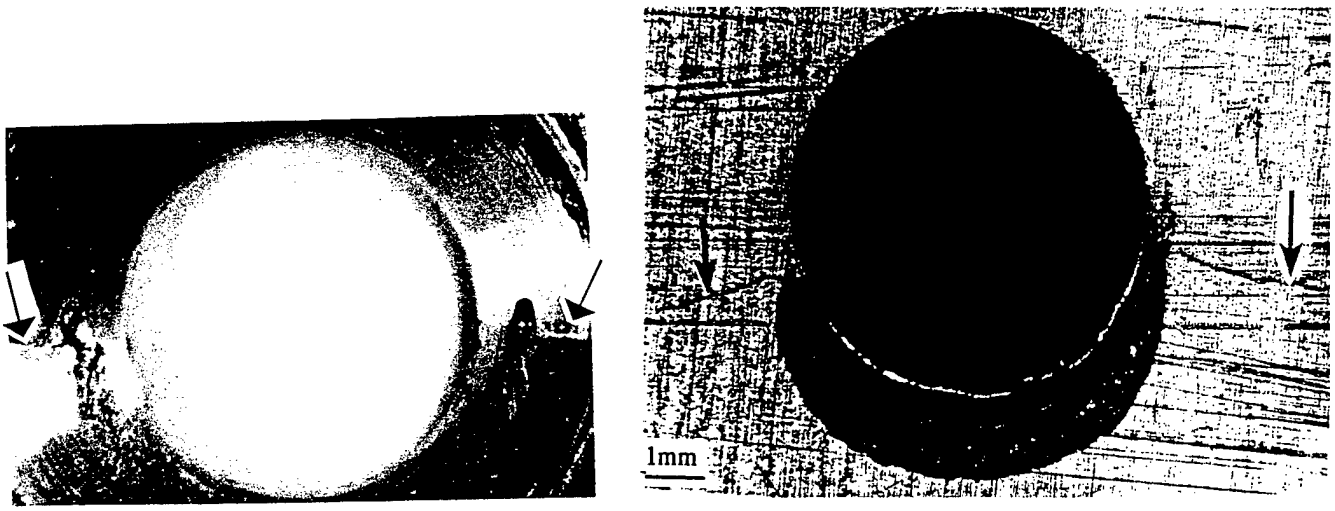

(a) (b)

Figure 4. Examples of fretting fatigue at different locations of a single rivet-row lap joint: (a) fretting fatigue at the countersunk rivet shank-panel interface near $\theta = 0°$ and $\theta = 180°$ (location A in Figure 2), (b) fretting fatigue at the rivet shank-panel interface (location B in Figure 2). Fretting at the rivet shank-panel interface at $\theta = 90°$ (location D in Figure 2) produces wear but no fatigue cracks. Arrows point to fretting fatigue cracks.

fretting as well as on interference and clamping (Figures 3c and 3d).

(iii) Interference and clamping dramatically reduce the drivers for in-plane fatigue and fretting fatigue (Figures 3a - 3d). *However, the interference produced by a uniform expansion of the rivet shank is not optimum at the panel-panel interface location.*

(iv) Large slip amplitudes at the panel-panel interface coupled with out of plane movement of the rivet head *and a compliant panel hole-edge* promote fretting fatigue at the panel-panel interface (Figures 2 and 4b).

(v) *The stresses generated in the rivet bodies are sensitive to rivet and panel geometry.*

2.3 Analyses of Fretting Fatigue Lives.

The present analyses, which allow the evaluation of peak values of F_2, provide a rough measure of the fretting fatigue life. This is based on the findings of Novell and Hills (4.11) who demonstrate the following relation between F_2 and the cyclic life, N for an aluminum alloy:

$$N > 10^7 \quad \text{when } F_2 < 4 \cdot 10^9 \text{ Pa}^2\text{m} \quad \text{and}$$
$$N << 10^7 \quad \text{when } F_2 > 4 \cdot 10^9 \text{ Pa}^2\text{m}.$$

Viewed in this light, the F_2-values given in Table 2 for a nominal cyclic stress of 90 MPa provide rough estimates of the joint fretting fatigue lives of the various lap joints. These results indicate that only the double rivet-row joint with interference is likely to display a long life. In this case, the nominal cyclic stress must be reduced by more than 50% to compensate for the absence of interference because $F_2 \propto \Delta\sigma^3$. The lives of the single rivet-row joint at this stress will be very short even with interference. Consistent with this prediction, single row lap joint specimens with the same geometry as the finite element model and with interference, failed after as few as $N = 3 \cdot 10^3$ stress cycles at a nominal cyclic stress of 65 MPa.

TABLE 2. PEAK F_2-VALUES CALCULATED FOR DIFFERENT CONNECTIONS

Fretting Fatigue Driver	0% Interference		1% Interference	
	Single Rivet-Row	Double Rivet-Row	Single Rivet-Row	Double Rivet-Row
Peak F_2, 10^{10} Pa^2.m	297.4	75.1	30.0	0.12

2.4 Piezoelectric-Actuated Fretting Wear Machine

A piezoelectric crystal-driven fretting wear machine has been constructed that can generate the fretting wear conditions found in connections, e. g., contact pressures up to ~1 GPa and the wide range of slip amplitudes from 1 μm to 80 μm. A complete description and drawings of the device can be found in Appendix C (4.12). Tests can be performed either in laboratory air, in an atmosphere, under corrosive conditions or vacuum. Profilometer measurements of the wear scar define the specific fretting wear rate (see Appnedices D and E). The device is also instrumented to measure the friction force-slip hysteresis loop which is used to define the friction condition (stick, mixed slip-stick, etc.) and the friction coefficient. Examples are reproduced in Figure 5.

2.5 Specific Fretting Wear Rates of Airframe Materials

Values of the friction coefficient and specific fretting wear rates for contact between the following couples:2024-T3 / 2024-T3, 7075-T6 / 7075-T6, 2024-T3 / hardened steel, and 7075-T6 / hardened steel under dry and corrosive conditions have been obtained. Examples of the results can be found in Figure 6 and in Appendices D and E. Corrosive conditions elevate the specific wear rate by 20-fold.

2.6. Cyclic Loading Tests of Laboratory-Scale Riveted Connections Under Dry and Accelerated Corrosion

Tests of one rivet-row and 2 rivet-row lap joints have been performed in air and with the joint immersed in salt water and subject to anodic current to accelerate corrosion. These samples have been examined after testing for signs of fretting, corrosion and fatigue. Recent results for a set of tests of 3 rivet/one-rivet row lap joints fastened with steel bolts subjected to both a nominal cyclic stress of 50 MPa (R = 0.1) in 3.5% saline solution at 0.1 Hz and imposed EMFs are summarized below. Both the cyclic lives in the table and the appearance of the failed samples point to very different failure mechanisms. In samples 1 and 2, fretting damage is reduced by both the larger panel gage which reduces hole edge crimping and by the larger clamping forces achieved with the stiff steel fasteners. As a result, large stresses are not communicated to the panel hole, and the failure is remote from the hole (see Figure 7). Nevertheless, the corrosive conditions of Sample 2 produced a 4-fold reduction in the cyclic life. Samples 3 and 4, which are thinner, show signs of fretting damage of the type illustrated in Figure 3 and lives reduced by the corrosive condition. The studies conducted so far indicate that fretting combined with corrosion accelerates fretting-assisted fatigue and may promote the general, hidden corrosion that plagues airframes.

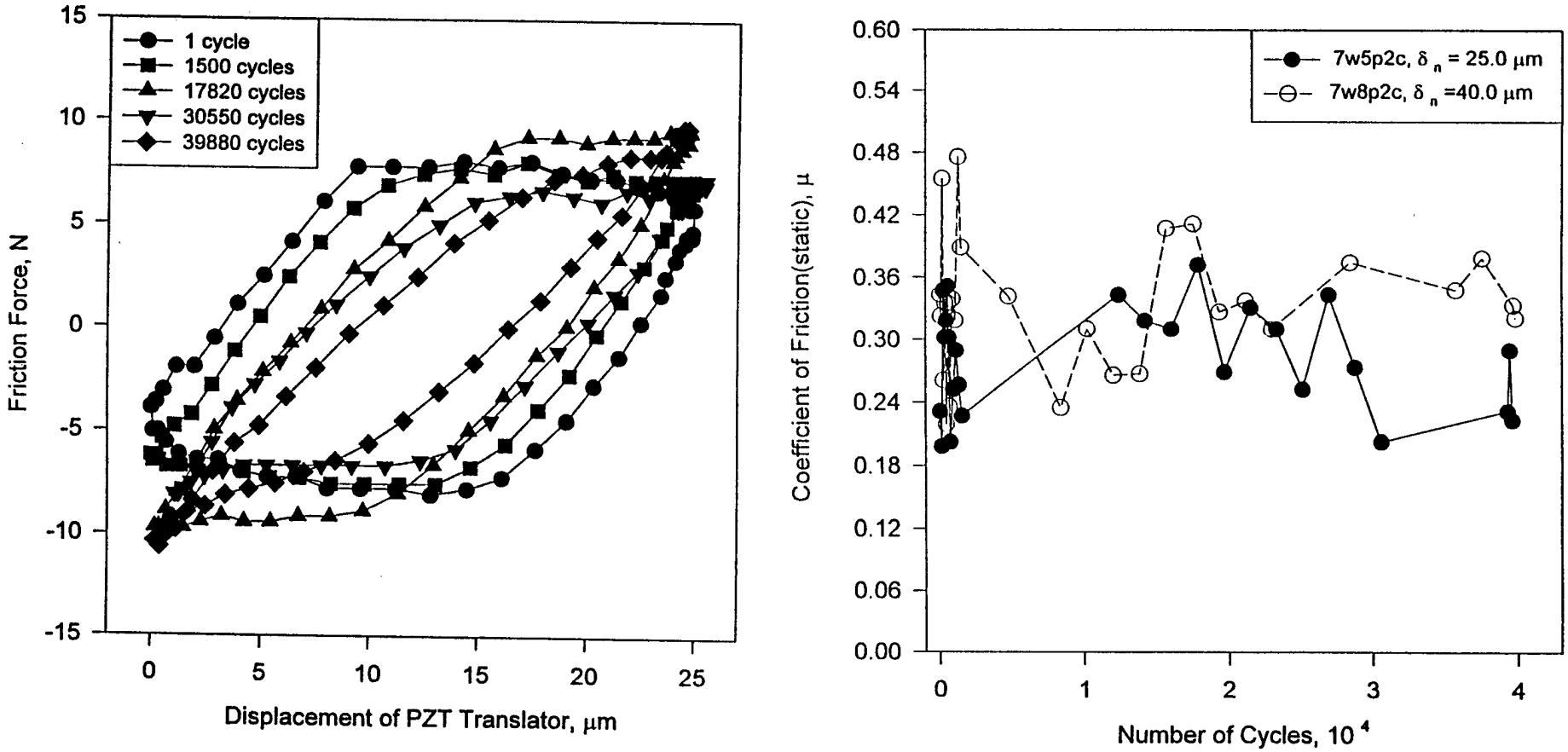

Figure 5 Results of friction measurements performed with the piezoelectric fretting wear machine. The measurements are for a 7075-T6 sphere in contact with a 7075-T6 flat at a contact pressure of 988 MPa and slip amplitudes of 25 μm and 40 μm in saline solution: (a) variation of friction force with applied displacement after different numbers of stress cycles and (b) the corresponding variation of the friction coefficient with number of stress cycles at the 2 slip amplitudes.

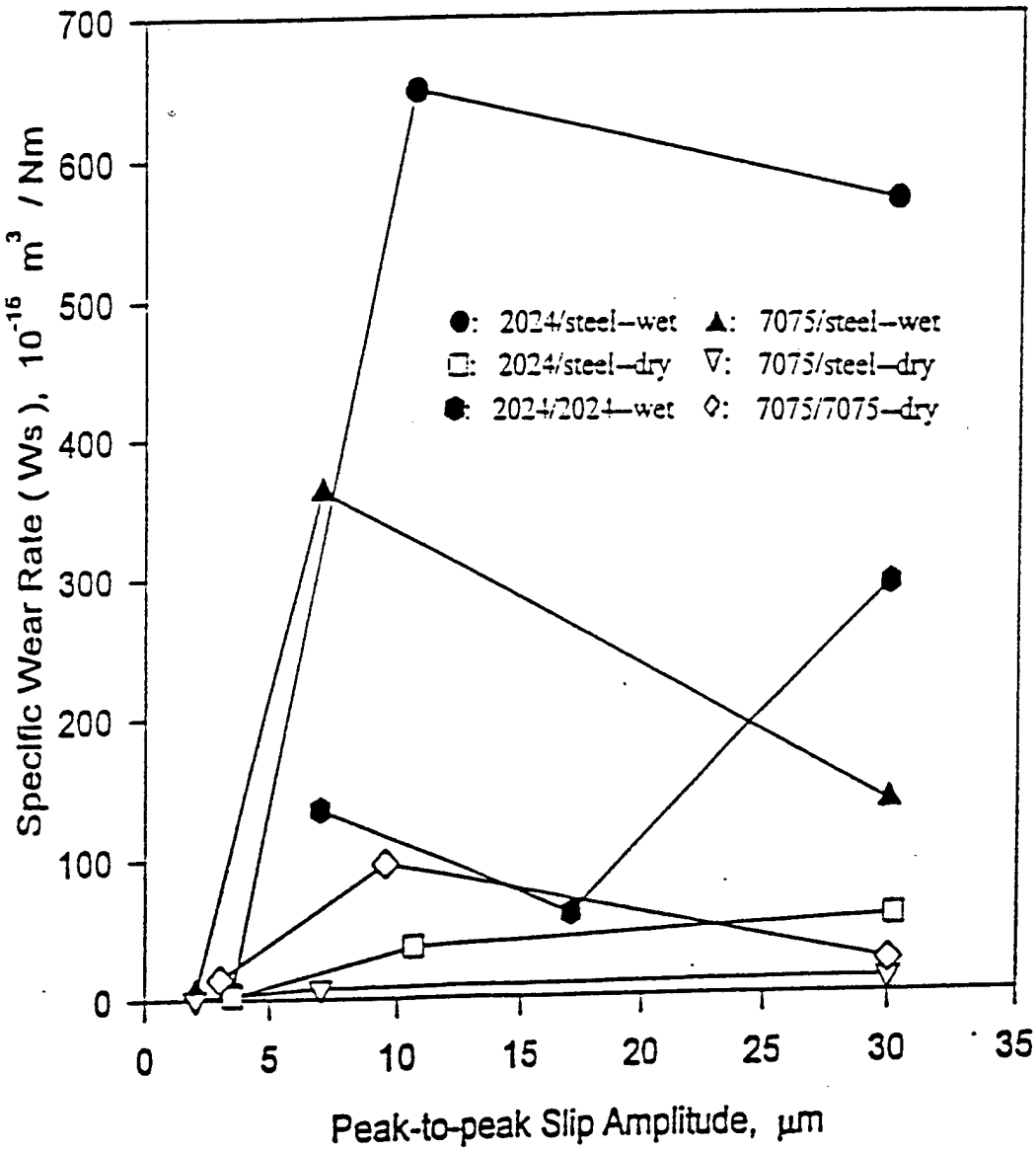

Figure 6 Variation of the specific fretting wear rate with slip amplitude for aluminum sheet alloys in contact with either aluminum or hardened steel and subjected to a nominal contact pressure of 408 GPa in laboratory air and 3.5% NaCl solution.

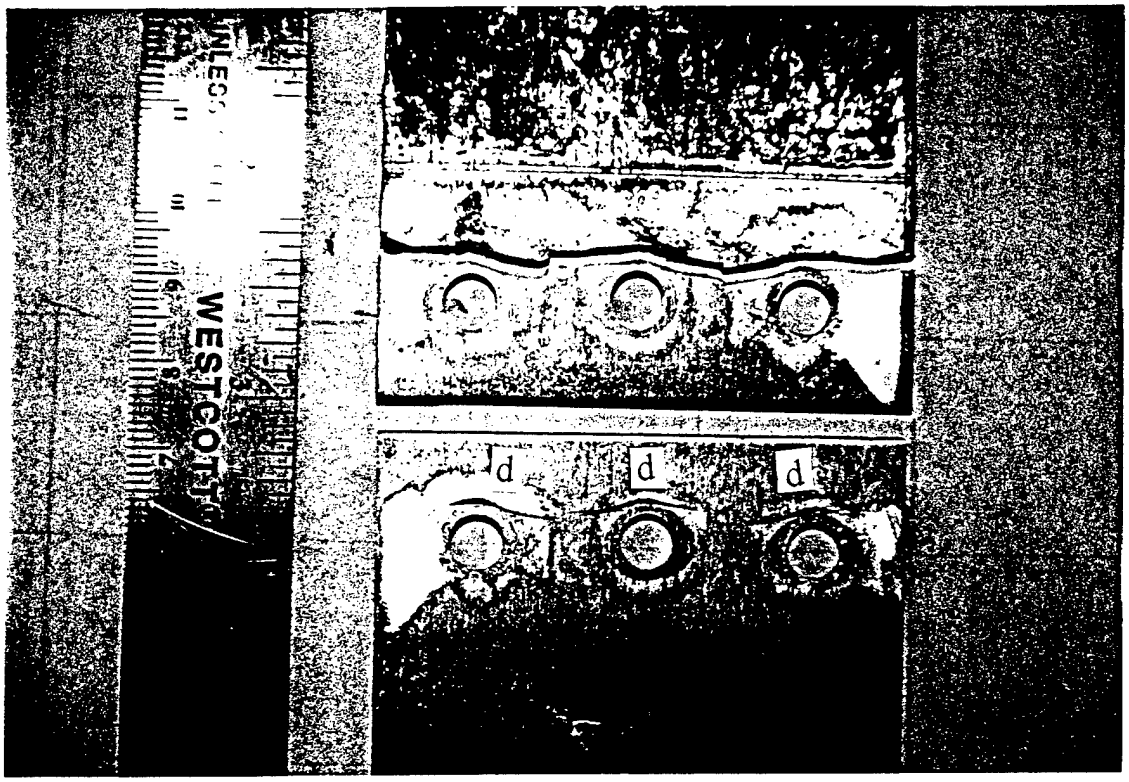

Figure 7 Failure of 3-rivet, 1-rivet-row test sample (sample 2 in Table 1) subjected to cyclic loading with a frequency of 0.1 Hz to a nominal stress of 50 MPa (R = 0.1) in 3.5% NaCl with an imposed anodic emf. The sample failed after 26,070 stress cycles compared with > 100,000 cycles for a cathodically protected sample (sample 1 in Table 1). Both samples were assembled with steel fasteners and dislayed the same type of fracture.

Unlike the failures illustrated in Figure 3 where the failure originated at the hole edge of the upper, countersunk panel (refer to Figure 1) of a joint fastened with aluminum rivets, this failure originated remote from the hole in the lower, noncountersunk panel. The failure is believed to be related to the high stresses at the interior surface of the lower panel (see location B in Figure 2), and the effects of the lateral clamping produced by the stiffer, steel fasteners. Fretting wear damage produced by the fracture edge is visible at (d).

Table 1. Results of Accelerated Corrosion Tests on 3-Rivet, One-Rivet-Row Test Samples.

Sample No. & (Thickness, in)	Imposed EMF, Volt	Cyclic Life	Mechanism of Failure
1 (0.085)	-1 (cathodically protected)	> 100,000	Cyclic bending of the interior (non countersunk) panel remote from hole and at washer edge
2 (0.085)	+1 (anodically dissolved)	26,070	Same as Sample 1
3 (0.063)	+2 (anodically dissolved)	8,430	Superposition of cyclic tension and fretting stresses at the fastener hole
4 (0.063)	+2 (anodically dissolved)	8,448	Same as Sample 3.

3. CONCLUSIONS

3.1 A piezoelectric-actuated fretting wear and fretting corrosion machine has been devised. The built-in, closed-loop feedback control system offers constant nominal displacements in the range 1 μm to 100 μm, cyclic frequencies in the range 0.05 to 30 Hz, and constant, contact forces that produce nominal contact pressures in the range 200 MPa to 1000 MPa for a 500 μm-diameter contact patch. The coefficient of friction and the specific wear rate in air and corrosive media can be measured under these conditions.

3.2 The coefficient of friction for 2024-T3 and 7075-T6 aluminum in fretting contact with 52100 steel dependson the slip amplitude and applied normal force. The specific wear rates are nearly 10-times higher in NaCl solution than in dry air with plastic deformation, adhesion, abraision, corrosion and fatigue the main damage mechanisms. For 7075-T6, the specific wear rate in air is initially high for small number of fretting cycles and then diminshes to about $W_S = 10^{-13}$ m^3 /Nm. The specific wear rate is the highest for 7075-T6 fretting against 7075-T6 in saline solution, followed by 7075-T6 against steel in saline solution; the lowest wear rate is observed for 7075-T6 fretting against steel in air.

3.3 Interference in a single, rivet-row lap joint with non-countersunk rivet heads elevates the contact pressure and decreases the slip amplitude at the rivet shank-panel hole interface. Interference also increases the cyclic mean stress and decreases the cylic stress range in the panel immediately adjacent and parallel to the hole surface.

3.4 Tests of small, laboratory size riveted lap joint inidicate that fretting combined with corrosion accelerates fretting-assisted fatigue and may promote the general, hidden corrosion that plagues airframes.

3.5 Clamping reduces the peak contact pressure and slip amplitude at the rivet shank-panel hole interface. Clamping also inhibits unloading of the joint and decreases the cyclic mean stress and stress range in the panel.

3.6 Both interference and clamping improve the resistance of the joint to fretting wear and crack initiation, as indicated by the parameters F_1 and F_2. The combination of interference and clamping is better than either, considered singly, in postponing crack initiation in non-countersunk and countersunk installations. .

3.7 Interference shifts the peaks of the fatigue and fretting fatigue parameters at and around the shank hole interface towards the loading end. Clamping has a very marginal effect, if any, on the peak location.

3.8 The value of F_2, generated in single rivet-row lap joints subject to a cyclic nominal stress of 125 MPa exceeds the critical value for fretting fatigue proposed by Nowell and Hills by at least an order of magnitude. This favors early initiation of fretting fatigue cracks.

3.9 In the absence of interference, fretting fatigue crack initiation will occur first in the countersunk panel. For some values of interference, the fretting fatigue conditions are more severe in the non-countersunk panel with the non-countersunk rivet head.

3.10 The fretting wear prameter, F_1 , is a reliable indicator of fretting wear zones.

3.11 Installing adacent rivets in the same row with different amounts of interference and clamping may offset the crack initiation locations and crack growth trajectories. This could postpone the interaction of adjacent cracks growing toward each other and increase the cyclic life.

4. REFERENCES

4.1 C. P. Fund and J. Smart, "An Experimental and Numerical Analysis of Riveted Single Lap Joints", Proc. Inst. Mech.. Eng. Part G, J. Aerospace Eng., Vol. 208, 1994, pp 79-90.

4.2 K. Iyer, G. T. Hahn, P. C. Bastias and C. A. Rubin, "Analysis of Fretting in Pinned Connections", Wear, Vol. 181-183, 1995, pp. 524-530.

4.3 K. Iyer, M. Xue, R. Kasinadhuni, P. C. Bastias, C. A. Rubin, J. J. Wert and G. T. Hahn, "Contribution of Fretting to the Fatigue and Corrosive Deterioration of a Riveted Lap Joint", Structural Integrity in Aging Aircraft, C.I. Chang and C.T. Sun Eds., pp. 35-62, AD-Vol. 47 (ISBN 0-7918-1724-5), ASME, New York, 1995.

4.4 K. Iyer, M. Xue, R. Kasinadhuni, P. C. Bastias, C. A. Rubin, J. J. Wert and G. T. Hahn, "Contribution of Fretting to the Fatigue and Corrosive Deterioration of a Riveted Lap Joint"Proc. Air Force 3rd Aging Aircraft Conference, WPAFB, 1995.

4.5 K. Iyer, M. Xue, P.C. Bastias, C.A. Rubin and G.T. Hahn, "Analysis of Fretting and Fretting Corrosion in Airframe Riveted Connections", to be presented at the May 6-7, 1996 AGARD Specialists' Meeting on "Tribology for Aerospace Systems", Sesimbra. Portugal.

4.6 K. Iyer, "Three-Dimensional Finite Element Analyses of the Local Mechanical Behavior of Riveted Lap Joints", PH.D. Dissertation, Vanderbilt University, May 1997.

4.7 K Iyer, G. T. Hahn and C. A. Rubin , "Three-Dimensional Analyses of Single Rivet-Row Lap Joints - Part I: Elastic Response" (to be published).

4.8 K Iyer, G. T. Hahn and C. A. Rubin , "Three-Dimensional Analyses of Single Rivet-Row Lap Joints - Part I: Elastic-Plastic Response" (to be published).

4.9 K. Iyer, G. T. Hahn and C. A. Rubin, "Three-Dimensional Analyses of Double-Rivet-Row Lap Joints - Part I: Non-Countersunk Rivets" (to be published)

4.10 K. Iyer, G. T. Hahn and C. A. Rubin, "Three-Dimensional Analyses of Double-Rivet-Row Lap Joints - Part II: Countersunk Rivets" (to be published)

4.11 D. Novell and D. A. Hills, "Crack Initiation Criteria in Fretting Fatigue" Wear, Vol. 136, pp. 329-343, 1990.

4.12 M. Xue, "Fretting Wear and Fretting Corrosion of Aeronautical Aluminum Alloys", M.S. Thesis, Vanderbilt University, December 1997.

5. PROJECT STAFF

The following Vanderbilt faculty members and graduate studentsl participated in the project:

George T. Hahn (P.I.), Professor of Materials Science and Mechanical Engineering.
James J. Wert, Professor of Materials Science and Mecanical Engineering
Carol A. Rubin, Professor of Mechanical Engineering.
Pedro C. Bastias, Research Assistant Professor of Materials Engineering
Kaushik Iyer, Graduate student (Completed Ph.D. degree in May 1996)
Miangue Xue, Graduate student (Completed M.S. degree in December 1997)

6. PROJECT PUBLICATIONS

6.1 K. Iyer, G. T. Hahn, P. C. Bastias and C. A. Rubin, "Analysis of Fretting in Pinned Connections", Wear, Vol. 181-183, 1995, pp. 524-530.

6.2 K. Iyer, M. Xue, R. Kasinadhuni, P. C. Bastias, C. A. Rubin, J. J. Wert and G. T. Hahn, "Contribution of Fretting to the Fatigue and Corrosive Deterioration of a Riveted Lap Joint", Structural Integrity in Aging Aircraft, C.I. Chang and C.T. Sun Eds., pp. 35-62, AD-Vol. 47 (ISBN 0-7918-1724-5), ASME, New York, 1995.

6.3 K. Iyer, M. Xue, R. Kasinadhuni, P. C. Bastias, C. A. Rubin, J. J. Wert and G. T. Hahn, "Contribution of Fretting to the Fatigue and Corrosive Deterioration of a Riveted Lap Joint"Proc. Air Force 3rd Aging Aircraft Conference, WPAFB, 1995.

6.4 K. Iyer, M. Xue, P.C. Bastias, C.A. Rubin and G.T. Hahn, "Analysis of Fretting and Fretting Corrosion in Airframe Riveted Connections", to be presented at the May 6-7, 1996 AGARD Specialists' Meeting on "Tribology for Aerospace Systems", Sesimbra. Portugal.

6.5 K. Iyer, "Three-Dimensional Finite Element Analyses of the Local Mechanical Behavior of Riveted Lap Joints", PH.D. Dissertation, Vanderbilt University, May 1997.

6.6 M. Xue, "Fretting Wear and Fretting Corrosion of Aeronautical Aluminum Alloys", M.S. Thesis, Vanderbilt University, December 1997.

6.7 K. Iyer, P. C. Bastias, C. A. Rubin and G. T. Hahn, "Influence of Interference and Clamping on Fretting Fatigue in Aluminum, Single Rivet-Row Lap Joints; Part I: Non-Countersunk Rivet" To be published (included as Appendix A).

6.8 K. Iyer, P. C. Bastias, C. A. Rubin and G. T. Hahn, "Influence of Interference and Clamping on Fretting Fatigue in Aluminum, Single Rivet-Row Lap Joints; Part 2: Countersunk Rivet" To be published (included as Appendix B).

6.9 M. Xue, J. Wert, P. Bastias and G. Hahn, "A Piezoelecric-Actuated Fretting Wear Machine," To be Published (included as Appendix C)

6.10 M. Xue, J. Wert, P. Bastias and G. Hahn, " Fretting Corrosion of 2024-T3 Aluminum Alloy", To be published (included as Appendix D)

6.11 M. Xue, J. Wert, P. Bastias and G. Hahn, "Fretting Corrosion of 7075-T3 Aluminum Alloy", To be published (included as Appendix E).

7. PATENT DISCLOSURE

The possibility of seeking a patent for the piezoelectric fretting machine is being explored by Vanderbilt University.

D68/a:fretfin2

APPENDIX A

Influence of interference and clamping on fretting fatigue in aluminum, single rivet-row lap joints - Part I: non-countersunk rivet

K. Iyer†, P. C. Bastias, C. A. Rubin, G. T. Hahn

Department of Mechanical Engineering
Box 1592, Station B
Vanderbilt University
Nashville, TN 37235

Abstract

Numerical evaluation of primary fretting fatigue variables such as contact pressure, slip amplitude and bulk tensile stress, at and near the contact interface between the rivet shank and panel hole in a single rivet-row, 7075-T6 aluminum alloy lap joint is presented. Three-dimensional finite element analysis is applied to evaluate the effects of interference and clamping stresses on the values of the primary variables and other mixed (multi-variable) measures of fretting damage. This article, the first of a two-part paper, considers a non-countersunk rivet geometry. Both interference and clamping lower the cyclic slip amplitude, stress range and other composite indicators for crack initiation. However, interference elevates the mean stress, whose effect on fretting fatigue remains unclear. Variations of the cyclic stress range and other proponents of crack initiation peak at distinct locations along the critical interface, making it possible to predict crack initiation locations.

List of Symbols

A	cross-sectional area of panel
L	overall length of riveted lap joint
E	Young's Modulus
σ_y	monotonic yield strength
σ_κ	kinematic yield strength
M	overall plastic modulus (including elastic slope contribution)
$\Delta\sigma$	cyclic stress range
σ_m	mean stress
P	applied load
Δ	total displacement
p	contact pressure
μ	coefficient of friction
τ	frictional shear stress. $\tau = \mu \cdot p$
λ	slip: amount of relative movement between contacting surfaces
δ	slip amplitude: amount of relative movement between contacting surfaces per load cycle
θ	angular location. The $\theta = 90^0$ direction corresponds with the positive direction of the 1-axis (tensile loading axis). 3 o'clock corresponds to $\theta = 0^0$, 6 o'clock to $\theta = -90^0$ etc.
$\sigma_{\theta\theta}$	local circumferential tensile stress, parallel and adjacent to contacting surfaces
F_1	fretting wear parameter. $F_1 = \tau \cdot \delta$
F_2	fretting fatigue parameter. $F_2 = \sigma_{\theta\theta} \cdot \tau \cdot \delta = \sigma_{\theta\theta} \cdot F_1$

† now with the Dept. of Mechanical Engineering and Applied Mechanics, 2250 G. G. Brown Bldg., University Of Michigan, Ann Arbor, MI, 48109.

Introduction

The appearance of identical pairs of cracks at rivet holes in cyclically loaded airframe riveted lap joints has been well recognized for some time. The signature cracking pattern, commonly referred to as Multiple Site Damage (MSD), is a consequence of identical conditions of stress and wear existing at each rivet-hole interface in a particular row of rivets combined with load shedding [1]. Although efforts to study the issue of MSD and crack growth in these layered structures are rather extensive [2,3], descriptions of the local stresses and damage mechanisms in the interfacial regions surrounding the rivet leading to crack initiation are more limited. Experimental evidence confirming the presence of fretting between the panel holes and rivet that constitute riveted assemblies is quite adequate [4,5,6]. Fatigue loading of the assembly initiates cracks that emerge from a fretted region. In order to shed light on the initiation life, it follows that one must study the mechanics of fretting fatigue at the critical contact areas.

The fretting fatigue behavior of any system of contacting components depends primarily on the contact geometry, contact pressure (normal load), slip amplitude at the interface, frequency, material factors and environmental factors. The material pair and the surface environment determine the friction coefficient, its variation with slip amplitude, and tangential stresses generated at the interface. Oxide layers, corrosive media, etc., can play a critical role in the wear process and crack initiation [7,8,9].

Numerical estimation of the primary factors which lower the fatigue strength of fuselage riveted assemblies because of fretting have not been sought until recently. The present authors [10] have analyzed the propensity for fretting in a simple two-dimensional pinned joint with and without interference stresses. This has shown that interference residual stresses generated during rivet installation can affect the fretting fatigue performance of the joint by modifying its

compliance (stiffness) and the material response evolution with load cycling. However, this analysis assumes an Isotropic hardening behavior, which is at best valid only during rivet installation and the first load step. Other efforts [11,12,13,14] have addressed the issues of installation interference and clamping, but none account for the three-dimensional effects of countersinking, non-linear effects such as friction, and the correct cyclic material response. Most recently, the present authors have developed realistic three-dimensional finite element models to quantify the distortion of riveted lap joints under a monotonic load [15,16]. The present work involves the adaptation of these models to evaluate the fretting fatigue conditions in airframe alloy 7075-T6, single rivet-row lap joints. In order to account for the evolution of cyclic plasticity more appropriately, a "parallel-analyses" approach has been adopted. In one analysis, interference and clamping stresses generated due to rivet installation are modeled using monotonic properties and the Isotropic hardening approximation. Since it is not possible to alter the material response in the middle of an analysis, a second, independent analysis of the installation process and subsequent load cycling is performed with an elastic-linear-kinematic-plastic (ELKP) approximation, representative of the steady-state cyclic behavior. Results from the two analyses are combined to evaluate the steady-state cyclic contact pressures, slip amplitudes, tangential shear stresses and bulk (circumferential) tensile stresses at the rivet-hole interface in the riveted assemblies.

The present study of fretting fatigue in a single rivet-row lap joint is compiled into two parts. This part presents results of the analysis of a joint with a non-countersunk rivet. The circumstances (contact pressure, slip amplitude, etc.) under which fretting fatigue damage accumulates are evaluated and interpreted in terms of existing approaches for predicting crack initiation locations. Part II [17] contains results of the analysis of a joint with a countersunk

rivets. Detailed analyses of the effects of interference and clamping stresses on the distortions of a single rivet-row lap joint are presented elsewhere, independently [18]. They are applied here and in Part II directly to account for the effects of interference and rivet clamping on fretting fatigue parameters. Rivet and panel shapes and dimensions, and the rivet spacing are patterned after those employed in airframes.

Fretting Wear and Fretting Fatigue Crack Initiation

Traditionally, fretting wear has been expressed in terms of either the wear volume or the average depth of the fretting damage (wear scar), both of which are directly proportional to the contact pressure, slip amplitude, specific wear rate and number of fretting cycles. The specific wear rate is a property of all the materials in the system, and in the case of fretting, may also depend on the slip amplitude and contact pressure. The tribological conditions favoring fretting wear are large values of specific wear rate, contact pressure and slip amplitude [8]. Unfortunately, the magnitude of fretting wear is not a sufficient or completely reliable measure of the risk of fretting fatigue crack formation. In fact, at large slip amplitudes, incipient cracks may be constantly abraded away resulting mainly in material loss. Further, cracks have been observed under conditions showing very little wear [19]. Efforts to understand the relative weights of the primary factors responsible for the initiation of fatigue cracks under fretting conditions may be categorized according to two approaches currently in use. One, the fretting map approach [20,21,22,23], identifies and documents the dominant mode of material degradation near the interface under diverse combinations of slip amplitude, normal load, shear traction, frequency and number of cycles (fretting condition), on the basis of controlled laboratory tests. This approach has led to the identification of the mixed stick-slip fretting regime

as being most vulnerable to crack initiation. One may assume then that this regime also has the most optimal combination of fretting fatigue variables to promote cracking and cyclic plasticity. A second approach, based usually on computations and laboratory tests, may be described as mechanistic since it attempts to link the interfacial shear stress, slip amplitude and underlying bulk stress (cause) directly to crack initiation (effect). This approach involves the evaluation of the variations of the contact pressure, slip amplitude and other such primary fretting fatigue variables at and near the contact interface. Then, some overall parameter seeking to capture the synergistic effect of the individual factors is evaluated to predict crack initiation location and life.

Based on their study of fretting fatigue in dovetail joints, two mechanistic parameters were proposed by Ruiz et al. [24] to predict fretting damage and crack initiation. These are: (i) $F_1 = \tau \cdot \delta$, which is defined as the product of the interfacial tangential shear stress and the slip amplitude and is a measure of the frictional work expended per unit contact area, and, (ii) $F_2 = \sigma_{\theta\theta}(\tau \cdot \delta) = \sigma_{\theta\theta} \cdot F_1$, defined as the product of F_1 and the (bulk) tensile stress just beneath the contacting interface and parallel to it. In their study, the location of the peak value of F_2 coincided with the observed crack initiation site. Subsequently, Kuno et al. [25] went on to confirm a similar coincidence between the F_2 peak and crack initiation location under an axisymmetric Hertzian contact. Although a physical interpretation for F_2 remains elusive, Endo et al. [26] clearly showed that fretting damage does little to diminish fatigue strength in the absence of a bulk cyclic stress. More recently, Farris et al. [27] have proposed a multiaxial fretting fatigue crack initiation criterion which involves identifying the critical plane for initiation based on the product of the peak principal stress and principal strain amplitude. Conceptually, the criterion is similar to F_2 in the sense that it considers the product of parameters

that can independently drive crack initiation. It is more sophisticated than F_2 owing to its ability to account for non-normal angles of initiation.

In the present work, variations of the contact pressure, slip amplitude, bulk stress (adjacent and parallel to the contact interface), F_1 and F_2 are evaluated at and adjacent to the rivet-panel interface in single rivet-row lap joints. The merits and significance of parameters such as F_2 are also discussed.

Analytical Procedures

Material Constitutive Relation Model

In spite of the fact that most materials exhibit a definite hardening induced anisotropy, the Isotropic hardening representation is often used. It is an attractive choice owing to its simplicity and validity in the case of proportional loading, i.e., when the principal stresses do not rotate at any structural location. However, for the more general case of anisotropic hardening, a simplistic and useful representation is that of linear kinematic hardening or plasticity, in which the elastic domain retains a constant size but translates in stress space. The center of the elastic domain represents the internal, or back stress of the neutral state. This approach represents a first approximation to the Bauschinger effect. Crack initiation life in riveted assemblies has been shown to be a strong function of the interference and clamping stresses generated by rivet installation [28]. However, fretting fatigue cracks initiate after thousands of load cycles by which time the material is in a steady state. Employing Isotropic constitutive relations for the installation step (interference and/or clamping) is justifiable if the rivet and panels are assumed to be isotropic initially. But after the first loading, the kinematic yield strength may be exceeded in regions where significant compressive residual stresses are generated during the unloading

cycle. There is then the possibility that these regions experience continuing cyclic plasticity and are, therefore, prone to conventional fatigue and fretting fatigue. The purpose of the ELKP analysis is to evaluate this possibility quantitatively.

Material properties for the Isotropic hardening behavior are defined by E = 69 GPa, $\nu = 0.3$, σ_y = 530.75 MPa and M = 0.7 GPa. The material properties for the ELKP hardening behavior are defined by E = 69 GPa, $\nu = 0.3$, σ_k = 369.9 MPa and M = 57.5 GPa, where M is the overall plastic modulus [29]. The ELKP representation has a lower yield point and a greater hardening slope.

Under relatively ideal circumstances, a single analysis would be capable of simulating the installation effects with Isotropic constitutive relations and then switching to the ELKP properties for the load cycle. However, a dynamic analysis in which the stress-strain curve changes with load cycling without having to re-equilibrate to an artificial initial condition in between, is beyond the scope of present-day FEA. Instead, current analyses are constrained to utilizing a single material response curve. The residual stress state because of rivet installation is determined by the Isotropic hardening analysis. These residual stresses are then superimposed on the stress state determined with the ELKP analysis and are interpreted as first-order representations of the steady state *prior to crack initiation*. Local cyclic stress range variations are not subject to any modifications since they are determined exclusively by the ELKP constitutive relations.

Finite Element Model

The model geometry consists of two partially overlapping sheets (panels) coupled by a two-headed, non-countersunk rivet, shown in Fig. 1. This represents one half unit of a multi-

riveted, single row, wide panel extending in the positive and negative 2-directions. The repeat distance between successive units is 30.6 mm. Three-dimensional FEA was performed using the ABAQUS code; twenty-seven-noded brick elements were used to mesh the three bodies and single-noded slide surface elements were defined internally to solve the contact inequality constraints. A nominal, remote cyclic load defined by $\Delta\sigma = 90$ MPa and $R = 0.1$ is applied at the non-lapping end face of the upper sheet while the corresponding face belonging to the lower sheet is fixed along the x-axis; the Cartesian systems (1,2,3) and (x,y,z) are equivalent. Figure 1 shows the main features of the models. The 1-3 planes CD and EF are symmetry planes and are constrained against motion in the 2-direction. In addition, the edges parallel to the 2-axis, at a depth of 1.53 mm and on the 2-3 planes DF and CE are fixed in the 3-direction to prevent unrestrained rotation of the body in space. All the boundary conditions are symmetric.

Rivet installation interference stresses are modeled by forcing radial conformity between an initially oversized rivet shank and the panel holes. In this case the interference is produced only in the radial direction. Clamping stresses are generated by forcing the elongation of a rivet whose shank height (depth) is initially shorter than the combined depth of the two panels ($z = 2t$). Thus the clamping forces are also introduced by an interference (misfit) method. Table 1 indicates the amounts of interference and clamping misfits analyzed, where the misfit is expressed as a percentage of the panel hole diameter (6.12 mm) or combined panel thickness (3.06 mm). For model A0, only an ELKP analysis was performed since rivet installation effects are absent. For the remaining models in Table 1, two parallel analyses are performed; one with an Isotropic hardening approximation and the other with an ELKP approximation. Actual rivets are installed by an upsetting process, which simultaneously induces radial interference and vertical clamping. It is not the aim of this work to simulate the installation process itself but

rather to shed light on the effects of interference and clamping as separate fatigue life parameters.

Ball-on-flat fretting tests conducted for aluminum rubbing against itself have shown the friction coefficient, μ, to vary from 0.2 to 0.5 [30]. The slip amplitude ranges between 10 μm and 80 μm, the normal load between 28.2 N and 34 N and the frequency is 1 Hz. This variation in friction coefficient, μ, has been simplified in the models, and a constant value of 0.4 has been assumed for all interfaces.

The finite element meshes typically consist of 3171 user defined nodes, 252 user defined elements and 609 internally generated contact elements, with a total number of variables of approximately 11,340. Calculations typically consumed between 18,000s and 20,000s of CPU time on a SGI Power Challenge Array.

Results

Loading typically results in rivet tilt accompanied by panel bending and contact between the rivet and panels and panels themselves. Detailed analyses of the distortions of single rivet-row lap joints under a uniaxial load are described elsewhere [15,16]. Of primary concern in fretting fatigue is the identification of macroscopic rivet-panel and panel-panel contact areas, and these are at three locations: (A) between the rivet shank and hole surfaces, (B) between the two panels, and (C) between the standard rivet head and panel surfaces. Each location represents a two-dimensional surface (field) along which fretting can occur. Figure 2 shows the intersections of the three fretting fields with the symmetry plane and the definition of angular locations according to the global coordinate axes. Fretting field A arises from the predominantly in-plane slips, λ_{12}, between the countersunk hole surface and rivet shank and is coincident with the

countersunk hole surface. Fretting field B is present because of the predominantly in-plane slips between a panel surface and the opposite panel hole edge and is present at symmetric 90° and -90° locations; its plane is coincident with the relevant portion of the panel surface.

Prior laboratory tests [6] by the present authors have confirmed the presence of fretting fields A and B. It has also been observed that contact between the standard rivet heads and panels (field C) does not lead to any significant fretting damage even though it affects the mechanics of distortions in the shank-hole interface by affecting the load transfer path [15,16]. Figure 3 shows the important fretting fields that arise from fatigue loading of riveted assemblies in the laboratory. The cracks that lead to MSD typically arise due to fretting between the rivet shank and hole surfaces (A). The panel material in fretting field B is responsible for in-plane load transfer to the rivet and yields in compression along the loading axis [16]. Fretting damage in this highly deformed regions is extremely severe in terms of abrasive wear, but the compressive bulk stress safeguards this highly plasticized volume from crack initiation.

Results which follow concentrate on shank-hole fretting and the repercussions on crack initiation there. Although slip amplitude vectors at any location possess in-plane, δ_{12}, and out-of-plane, δ_{13}, components, only the in-plane component is considered and presented given its predominance. The results presented for model A0 (no rivet installation effects) are for the ELKP material constitutive relation. Calculated variations of the local mean stress and bulk circumferential stress under maximum load are determined first for the ELKP constitutive relation, and then modified by the installation residual stress state using the Isotropic constitutive relation.

Figures 4-7 show the variations with the angular location, θ, of the contact pressure, the in-plane slip and the local in-plane tensile stress parallel to the shank-hole interface in the upper

panel. Table 2 shows values of some parameters at different locations through the hole depth; 2% interference generates compressive residual stresses between $0 \leq z \leq 0.5t$ and tensile residual stresses at $z = t$. Conditions in the lower panel mirror those in the upper panel and are not shown. Results for the case without any interference and clamping (model A0) include the variations of the above fretting fatigue variables with the hole depth. For the sake of brevity and clarity, results for models A1-A4 show angular variations only at the depth where the above variables are most critical, which is $z = t$; variations through the depth are not the same as in model A0 but do follow a similar trend.

Peak shank-hole contact pressures of about 580 MPa are produced at $z = t$ upon loading, in the absence of interference and clamping (see Fig. 5(a)). Loading causes the panel hole to pull away from the rivet and contact between the rivet shank and hole is lost almost uniformly through the hole depth, between 90° and approximately -4.3° in model A0 ($p = 0$ when contact is lost). Interference shifts the angular location at which rivet-hole contact is lost towards 90° (loading direction) thus increasing the area over which the shank and hole remain in contact. Additionally, interference generates shank-hole contact pressures which vary through the depth but remain approximately uniform at a given depth. Interference increases the loaded shank-hole contact pressure, the peak value rising to about 800 MPa with 2% interference (see Fig. 5(b)). The unloaded value is determined by the uniform interference pressure and any additional material yielding. Pure clamping reduces the peak, loaded shank-hole contact pressures from 580 MPa to about 500 MPa and increases the unloaded pressures by about 350%.

Fig. 5(a) indicates that clamping can inhibit unloading. The effect of clamping on the angular range over which contact is lost is negligible in the absence of interference. Interference and clamping lower slip amplitudes as expected. A detailed analysis of the effects of interference

and clamping are presented elsewhere [18]. Figures 5(b) and 6 show that, in the absence of interference and clamping, through-the-depth variations of total in-plane slip and slip amplitude show little scatter in the range of $-90° \leq \theta \leq 0°$. Figure 4(a) shows that this is also the range of angular location over which the rivet shank and panel hole maintain contact under load. With interference and clamping, the scatter becomes even less. This implies that slip amplitude is a variable that does not determine the depth of MSD crack initiation in the lap joint. Beyond $\theta = 0°$, the slips and slip amplitudes peak distinctly at $z = t$ (see Figs. 5(b) and 6(a)). Panel bending and rivet tilt predispose the depth $z = t$ to the greatest loaded pressures and bulk tensile stresses.

Figure 7(a) shows the variation of circumferential tensile stresses in the panel hole immediately adjacent to the shank-hole interface at depth $z = t$. In the 2-dimensional analysis of a pinned joint where the pin remained elastic and was not allowed to tilt [10], circumferential stresses remained compressive under load with 2% radial interference. Recent work [18] has shown that non-uniform material yield across the hole depth during installation, which cannot be accounted for in a 2-dimensional analysis, leads to a corresponding plastic strain gradient, which results in compressive circumferential stresses at $z= 0$ and tensile values at $z = t$ (see Table 2). Figure 7(b) shows that 0.5% clamping is as effective as 2% interference in lowering the peak, bulk circumferential tensile stress at $z = t$, adjacent to the upper panel hole. It also indicates the shift in the angular location of the subdued $\sigma_{\theta\theta}$ peaks, towards the loading end.

Fatigue and Fretting Fatigue

Figure 8 shows the angular variation of the local cyclic stress range, $\Delta\sigma$ and local mean stress, σ_m, at $z = t$. Conventional fatigue parameters are of particular consequence if critical crack initiation is driven by conventional fatigue and fretting merely results in material loss. In the

absence of interference and clamping, the applied, nominal stress range, $\Delta\sigma = 90$ MPa, results in a peak $\Delta\sigma$ of about 530 MPa at -8.7°. Interference elevates the mean stress at the shank-hole interface, about which load/unload values fluctuate. Increasing interference diminishes the fluctuations and under these circumstances the mean stress increases and may gain in relative importance. Interference also shifts the location of the peak cyclic stress range towards 90°. Clamping diminishes the cyclic stress range and mean stress without altering the angular location at which $\Delta\sigma$ peaks.

Composite effects are expressed by the mechanistic parameters, F_1 and F_2, whose variations with angular location at z = t are shown in Fig. 10. In the absence of interference and clamping the peak value of F_1 is almost 2.4 kPa.m and it persists near -15.6°. Interference lowers the magnitudes of F_1 and, typically, a blunted peak persists over a range of angular locations which have been shifted towards the loading end (90°). Clamping also lowers F_1 magnitudes leaving the peak location unchanged. The reduction in fretting wear is particularly apparent when interference and clamping are applied together. The effects of interference and clamping on F_2 are similar.

Table 3 shows peak values of the mechanistic parameters through the depth of the shank-hole interface and their angular location. 2% interference renders the shank-hole circumferential stresses compressive even under load at z = 0 and z = 0.5t, and hence F_2 does not have any significance. The same is true for at z = 0 in model A3.

Discussion

For a nominal applied cyclic stress range, $\Delta\sigma = 90$ MPa, the peak value of the fretting wear parameter is $F_1 = 2.3$ kPa.m for in-plane, shank-hole wear. This is in the absence of

interference and clamping, and is less than the value of F_1 = 3 kPa.m, obtained with a two-dimensional analysis [10]. Peak values of the fretting fatigue parameter, F_2, are well above the value, $F_2 = 4 \cdot 10^9 \cdot Pa^2.m$, which can lead to fatigue crack initiation within 10^7 cycles in aluminum alloys according to Nowell and Hills [31]. For example, with 1% interference, the peak value of F_2 is $290 \cdot 10^9$ $Pa^2.m$; a two-dimensional calculation with 1% interference produced a peak value of $60 \cdot 10^9$ $Pa^2.m$ [10]. This implies that out-of-plane deformations, which cannot be accounted for in 2D analyses, are extremely important in determining the fretting fatigue resistance of the joint. Also, crack initiation well before 10^7 cycles may be expected. This is consistent with observations in practice [6], where cracks are known to initiate after a few thousand cycles. Laboratory fatigue tests of riveted assemblies by the present authors have shown that several microcracks, all close to each other, may be initiated in the panel hole. However, only one grows to dominance while the others stop growing, or more commonly, the microcracks join together in a river-delta pattern to form the dominant crack.

This work shows the feasibility of evaluating the individual variables that are responsible for fretting fatigue crack initiation in airframe riveted lap joints. Although the parameters $\Delta\sigma$ and F_2 may be considered to be crack initiation drivers and barometers, they cannot be assumed to be complete. There are other factors such as the repeat plasticity near the shank-hole interface which are yet to be accounted for. The establishment of a criterion for fretting fatigue crack initiation remains an independent area of study. It has been shown here that the values of all the mechanistic parameters that might find a place in the final criterion are already calculable.

Conclusions

1. Primary fretting fatigue variables in a single rivet-row lap joint have been evaluated for different amounts of interference, clamping and a non-countersunk rivet geometry.

2. Interference elevates the contact pressure and decreases the slip amplitude at the rivet shank-panel hole interface. Interference also increases the cyclic mean stress and decreases the cyclic stress range in the panel, immediately adjacent and parallel to the hole surface.

3. The single value of clamping stress examined results in a lowering of the peak contact pressure and slip amplitude at the rivet shank-panel hole interface. Clamping also inhibits the unloading of the joint and decreases the cyclic mean stress and stress range in the panel.

4. Both interference and clamping improve the resistance of the joint to fretting wear and crack initiation, as indicated by the mixed parameters F_1 and F_2. The combination of interference and clamping is better than either considered singly, in postponing crack initiation.

5. Interference shifts the peaks of fatigue and fretting fatigue parameters at and around the shank-hole interface towards the loading end. Clamping has a very marginal effect in this regard, if any.

6. Peaks in the angular variations of conventional fatigue parameters and the fretting fatigue parameter, F_2, are usually distinct. This offers a basis to identify the controlling mechanism for crack initiation.

7. The critical value of F_2 for fretting fatigue cracking in aluminum alloys proposed by Nowell and Hills, is exceeded by at least an order of magnitude. Accordingly, crack initiation well before 10^7 cycles is to be expected in single rivet-row assemblies.

Acknowledgments

The authors are grateful to Hibbitt, Karlsson and Sorensen, Inc. for permission to use their finite element code ABAQUS. This research was supported with a grant from the Air Force Office of Scientific Research (F49620-93-1-0488).

References

[1] Park, J. H. and Atluri, S. N., "Fatigue growth of multiple-cracks near a row of fastener-holes in a fuselage lap-joint," Computational Mechanics, v 13, n 3, Dec. 1993, pp. 189-203.

[2] Swenson, D. V., Chih-Chien, C. and Derber, T., "Analytical and experimental investigation of fatigue in lap joints," in Advances in Fatigue Lifetime Predictive Techniques, ASTM STP 1122, M. R. Mitchell and R. W. Landgraf, Eds., 1992, pp. 449-459.

[3] Swenson, D. V., Gondhalekar, S. R. and Dawicke, D. S., "Analytical developments in support of the NASA aging aircraft program with an application to crack growth from rivets," ISSN 0148-7191, SAE General, Corporate and Regional Aviation Meeting and Exposition, Wichita, Kansas, 1993.

[4] Adibnazari, S. and Hoeppner, D. W., "Study of fretting crack nucleation in 7075-T6 aluminum alloy," Wear, 159 (1992), pp. 257-264.

[5] Piascik, R. S., "The characterization of widespread fatigue damage in fuselage structure," NASA technical memorandum, 109142, Langley Research Center, 1994.

[6] Iyer, K., Xue, M., Kasinadhuni, R., Bastias, P. C., Rubin, C. A., Wert, J. J. and Hahn, G. T., "Contribution of fretting to the fatigue and corrosive deterioration of a riveted lap joint," Proc. Symp. Structural Integrity in Aging Aircraft, San Francisco, Nov. 15, 1995.

[7] Waterhouse, R. B., "Fretting corrosion," Pergamon Press, New York, 1972.

[8] Waterhouse, R. B., "Avoidance of fretting fatigue failures," in Fretting Fatigue, pp. 221-240, Ed. R. B. Waterhouse, Applied Science Publishers Ltd. (ISBN 0-85334-932-0), London, 1981.

[9] Waterhouse, R. B., "Fretting wear," ASM Metals Handbook, No. 18, pp. 242-256, 1992.

[10] Iyer, K., Hahn, G. T., Bastias, P. C. and Rubin, C. A., "Analysis of fretting conditions in pinned connections," Wear, 120 (1995), pp. 524-530.

[11] Schwarmann, L., "Influence of cold-working and interferencefit on fatigue life," Proc. Fatigue Prevention and Design, 21-24 April, 1986, J. T. Barnby, Ed., Amsterdam, The Netherlands.

[12] Ramamurthy, T. S., "Analysis of interference fit pin joints subjected to bearing bypass loads," AIAA Journal, v 28, n 10, 1990, pp. 1800-1805.

[13] Hermann, R., "Three-dimensional stress distribution around cold expanded holes in aluminum alloys," Experimental Mechanics, v 48, n 6, 1994, pp. 819-835.

[14] Sundarraj, N., Dattaguru, B. and Ramamurthy, T. S., "Analysis of a double shear lap joint with interference fit pin," Computers and Structures, v 55, n 2, 1995, pp. 357-363.

[15] Iyer, K., Bastias, P. C., Rubin, C. A. and Hahn, G. T., "Three-dimensional analyses of single rivet-row lap joints - Part I: Elastic Response," to be submitted to ASME J of App. Mech.

[16] Iyer, K., Bastias, P. C., Rubin, C. A. and Hahn, G. T., "Three-dimensional analyses of single rivet-row lap joints - Part I: Elastic-Plastic Response," to be submitted to ASME J of App. Mech.

[17] Iyer, K., Bastias, P. C., Rubin, C. A. and Hahn, G. T., "Influence of interference and clamping on fretting fatigue in aluminum, single rivet-row lap joints - Part II: countersunk rivet," submitted to Wear.

[18] Iyer, K., Bastias, P. C., Rubin, C. A. and Hahn, G. T., "Influence of interference and clamping on distortions and fatigue in aluminum, single rivet-row lap joints," to be published.

[19] Mutoh, Y., "Mechanisms of freting fatigue," JSME Int. J. Series A, Mechanics and Material Engineering, v 38, n 4 (1995), pp. 2331-2346.

[20] Vingsbo, O. and Soderberg, S., "On fretting maps," Wear, 126 (1988), pp. 131-147.

[21] Vingsbo, O., Oldfalk, M. and Shen, N. E., "Fretting maps and fretting behavior of some fcc metals and alloys," Wear of Materials, K. C. Ludema Ed., ASME, New York, pp. 275-282, 1989.

[22] Zhou, Z. R., Fayeulle, S. and Vincent, L., "Cracking behavior of various aluminum alloys during fretting wear," Wear, 155 (1992), pp. 329-343.

[23] Zhou, Z. R. and Vincent, L., "Cracking induced by fretting of aluminum alloys," personal communication of draft for publication (1996).

[24] Ruiz, C., Boddington, P. and Chen, K., "An investigation of fatigue and fretting in dovetail joints," Exp. Mech., v 24, 1984, pp. 208-217.

[25] Kuno, M., Waterhouse, R. B., Nowell, D. and Hills, D. A., "Initiation and growth of fretting fatigue cracks in the partial slip regime," Fatigue Fracture Engineering of Materials and Structures, v 12 (1989), pp. 387-398.

[26] Endo, K., Goto, H. and Nakamura, T., "Effect of cycle frequency on fretting fatigue life of carbon steel," Bulletin of JSME, v 12, n 54, 1969, pp. 1300.

[27] Farris, T. N., Harish, G., McVeigh, P. A. and Szolwinski, M. P., "An investigation of fretting fatigue in aging aircraft," Air Force 3rd Aging Aircraft Conference, Wright-Patterson AFB, Ohio, 26-28 September, 1995.

[28] Muller, R. P. G., "An experimental and analytical investigation on the fatigue behavior of fuselage riveted lap joints – the significance of the rivet squeeze force, and a comparison of 2024-T3 and Glare 3," Ph.D. dissertation (1995), Delft University of Technology, The Netherlands.

[29] Hahn, G. T., Bhargava, V. and Chen, Q., "The cyclic stress-strain properties, hysteresis loop shape and kinematic hardening of two high strength bearing steels," Met. Trans. A, v 21A (1990), pp. 653-664.

[30] Xue, M., "Study of fretting corrosion in aluminum alloys," Ph.D. dissertation proposal (1996), Vanderbilt University, USA.

[31] Nowell, D. and Hills, D. A., "Crack initiation criteria in fretting fatigue," Wear, 136 (1990), pp. 329-343.

List of Tables

1. The finite element models.

2. Variation of fretting fatigue variables through the depth of the upper panel hole.

3. Summary of mechanistic parameters indicating locations of fretting wear and crack initiation in lap joint assemblies with non-countersunk rivets.

List of Figures

1. (a) Multi-riveted, single rivet-row lap joint, of which one half-unit is considered for the 3D half-symmetry finite element model, (b) the thickness of each panel is t=1.53 mm. The rivet is non-countersunk with a shank diameter of 6.12 mm; the rivet head diameter and height are 9.792 mm and 3.83 mm respectively, (c) plan view of the mesh. The overall length of the model is 306 mm, the length of the overlap region is 30.6 mm and the width of the model (half the repeat distance) is 15.3 mm.

2. (a) Profile of a deformed mesh showing the three main rivet-panel and panel-panel fretting fatigue contact locations, (b) Schematic showing the definition of the angular locations and depth in the models.

3. Important fretting fields observed in laboratory tested riveted lap joints.

4. (a) Variation of contact pressure at the shank-hole interface with angular location and depth for Model A0, (b) Variation of contact pressure with angular location at depth z=t, where contact pressures peak, for Models A1 and A2.

5. (a) Angular variation of contact pressure at the shank-hole interface in Models A3 and A4 at z=t, depth at which the pressures peak, (b) Variation of in-plane slip between the panel hole and rivet in Model A0.

6. (a) Variation of in-plane slip amplitude at the shank-hole interface with angular location and depth for Model A0, (b) Angular variation in Models A1-A4 at depth z=t, where slip amplitudes peak.

7. (a) Variation of circumferential tensile stress, $\sigma_{\theta\theta}$, in the panel and immediately adjacent to the hole surface under maximum load, with angular location and depth for Model A0, (b) Variation with angular location at z=t, depth at which tensile stresses are greatest, for Models A1-A4.

8. Variation of conventional fatigue parameters at the rivet shank-panel hole interface at z=t. (a) cyclic stress range, $\Delta\sigma$, (b) mean stress, σ_m.

9. (a) Variation of the fretting wear parameter, F_1, with angular location at z=t, (b) Variation of the fretting fatigue parameter, F_2, depth at which both parameters peak.

Table 1. The finite element models.

Model	% Interference (radial misfit)	% Clamping (shank height misfit)
A0	0	0
A1	1	0
A2	2	0
A3	0	0.5
A4	1	0.5

Table 2. Variation of fretting fatigue variables through the depth of the hole.

Model		Installation $\sigma_{\theta\theta}$ (MPa)	Peak $\sigma_{\theta\theta}$ (MPa)	Peak δ_{12} (μm)
A0	z=0	0	429.9	25.7
	z=0.5t	0	533.2	30.4
	z=t	**0**	**594.8**	**34.7**
A1	z=0	35	95.0	2.7
	z=0.5t	114	196.4	4.4
	z=t	**325**	**518.3**	**7.2**
A2	z=0	-423	-351.6	1.4
	z=0.5t	-155	-76.1	2.2
	z=t	**252**	**388.7**	**5.2**
A3	z=0	-53	337.8	9.3
	z=0.5t	4	372.1	12.2
	z=t	**-14**	**410.2**	**13.7**
A4	z=0	-305	-216.6	1.5
	z=0.5t	142	218.5	3.1
	z=t	**280**	**411.1**	**4.8**

*Installation $\sigma_{\theta\theta}$ values are from the analyses with the Isotropic hardening approximation [18].

Table 3. Summary of mechanistic parameters indicating locations of fretting wear and crack initiation in lap joint assemblies with non-countersunk rivets.

		Peak Tangential Stress (MPa)		**Peak F_1 (kPa.m)**		**Peak F_2 (10^{10} Pa^2.m)**	
Model		**magnitude (MPa)**	**θ, °**	**magnitude (kPa.m)**	**θ, °**	**magnitude (10^{10} Pa^2.m)**	**θ, °**
A0	z=0	102	-45.0	0.81	-33.7	22.6	-22.5
	z=0.5t	116	-33.7, -45.0	1.38	-15.6, -22.5	60.3	-8.7
	z=t	**137**	**-33.7, -45.0**	**2.28**	**-15.6, -22.5**	**88.5**	**-8.7**
A1	z=0	83.1	15.6	0.20	15.6	1.4	0.0, 4.3
	z=0.5t	77	15.6,-4.3	0.27	33.7, 8.7	5.4	22.5, 15.6
	z=t	**124**	**-4.3, -8.7**	**0.56**	**8.7, -8.7**	**29.0**	**8.7**
A2	z=0	154	56.2, 45.0	0.16	33.7, 15.6	-	-
	z=0.5t	90	45, 15.6	0.20	33.7	-	-
	z=t	**146**	**-4.3**	**0.50**	**15.6**	**17.4**	**15.6**
A3	z=0	82.6	-45.0	0.32	-4.3, -15.6	9.5	-8.7
	z=0.5t	57.8	-33.7	0.26	-15.6	8.3	-15.6
	z=t	**132**	**-33.7**	**0.55**	**-15.6**	**17.8**	**-15.6**
A4	z=0	89	33.7, 22.5	0.11	33.7, 15.6	-	-
	z=0.5t	50	22.5, -4.3	0.13	33.7, 8.7	2.9	22.5, 15.6
	z=t	**102**	**-4.3, -8.7**	**0.29**	**15.6, 0.0**	**11.2**	**15.6, 8.7**

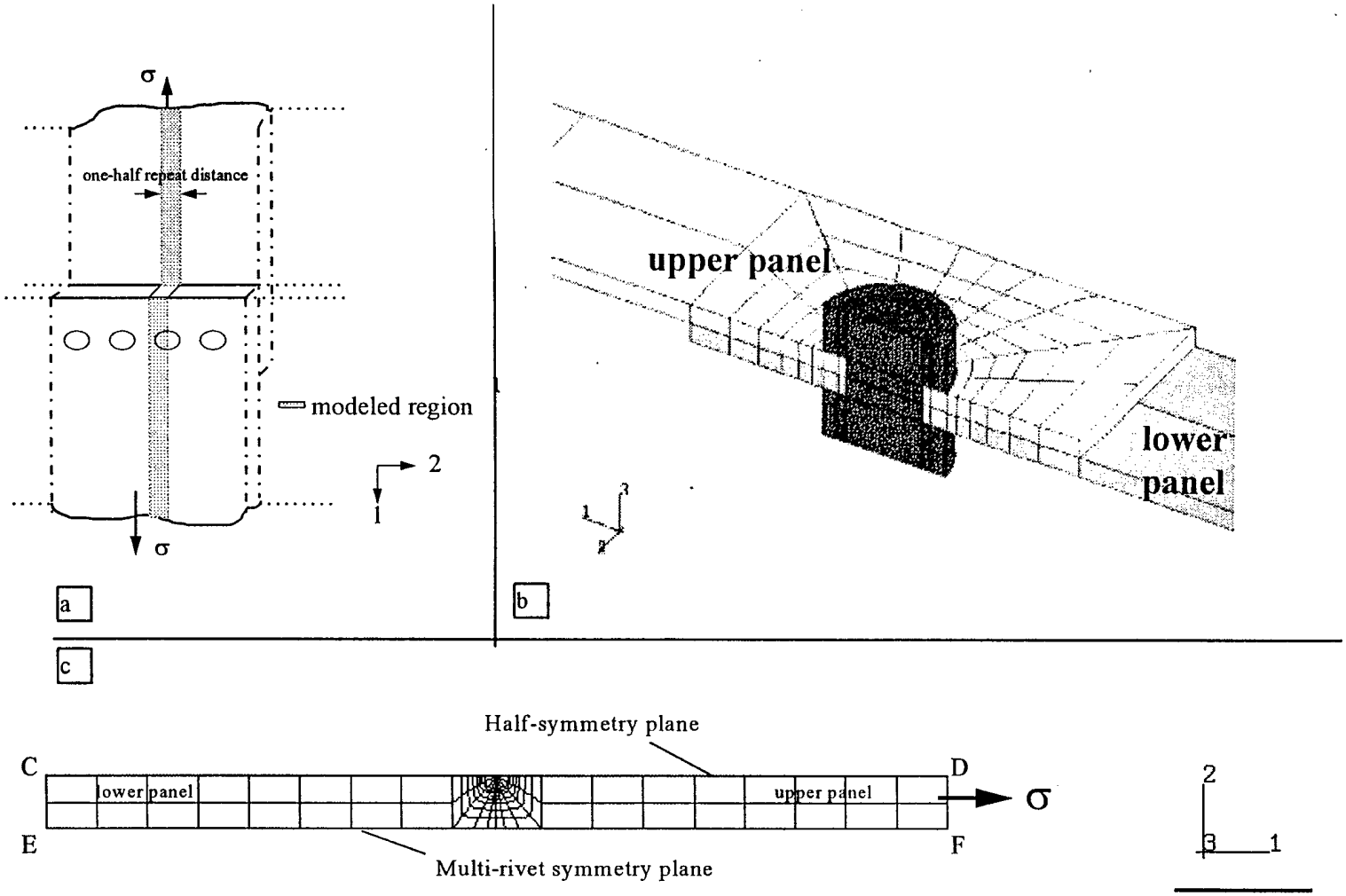

Figure 1. (a) Multi-riveted, single rivet-row lap joint, of which one half-unit is considered for the 3D half-symmetry finite element model, (b) the thickness of each panel is t=1.53 mm. The rivet is non-countersunk with a shank diameter of 6.12 mm; the rivet head diameter and height are 9.792 mm and 3.83 mm respectively, (c) plan view of the mesh. The overall length of the model is 306 mm, the length of the overlap region is 30.6 mm and the width of the model (half the repeat distance) is 15.3 mm.

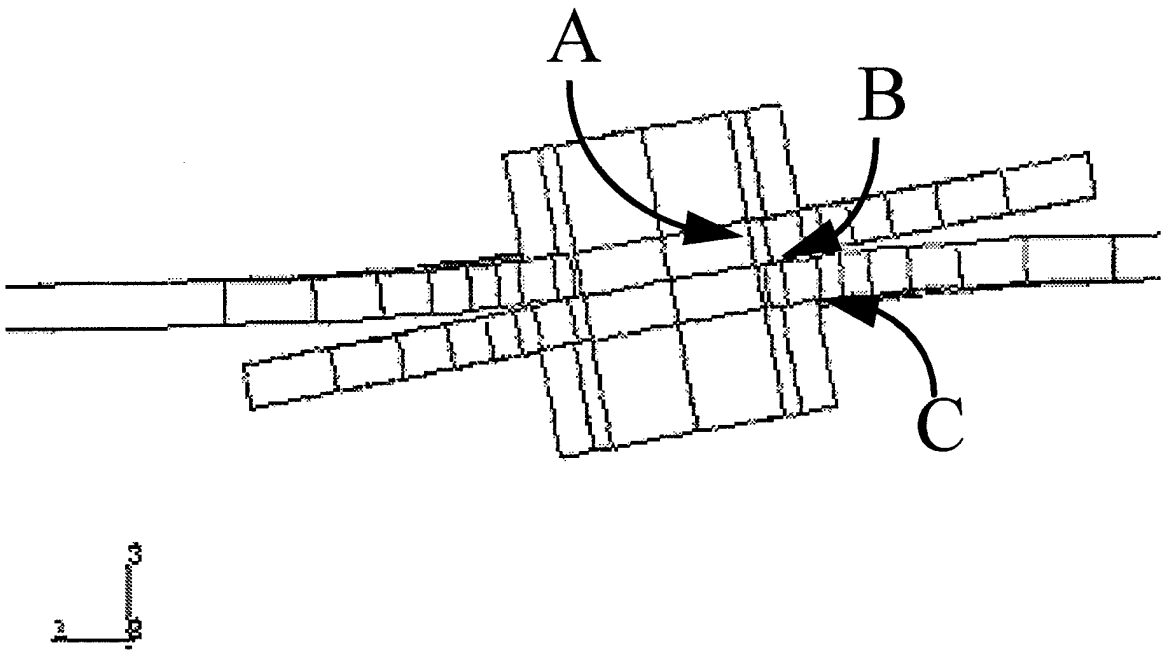

(a)

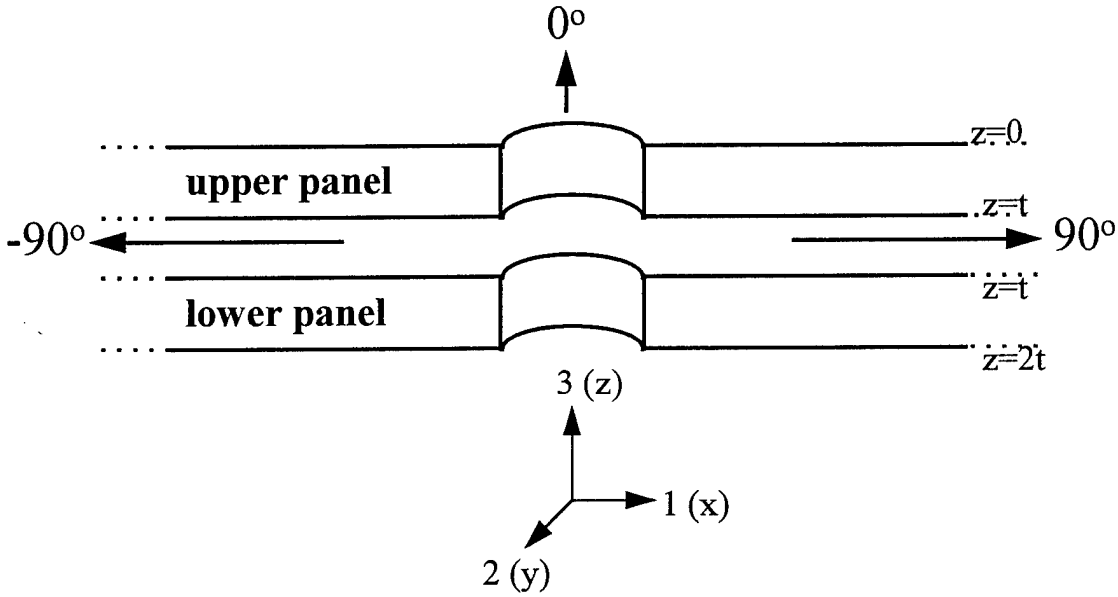

(b)

Figure 2. (a) Profile of a deformed mesh showing the three main rivet-panel and panel-panel fretting fatigue contact locations, (b) Schematic showing the definition of the angular locations and depth in the models.

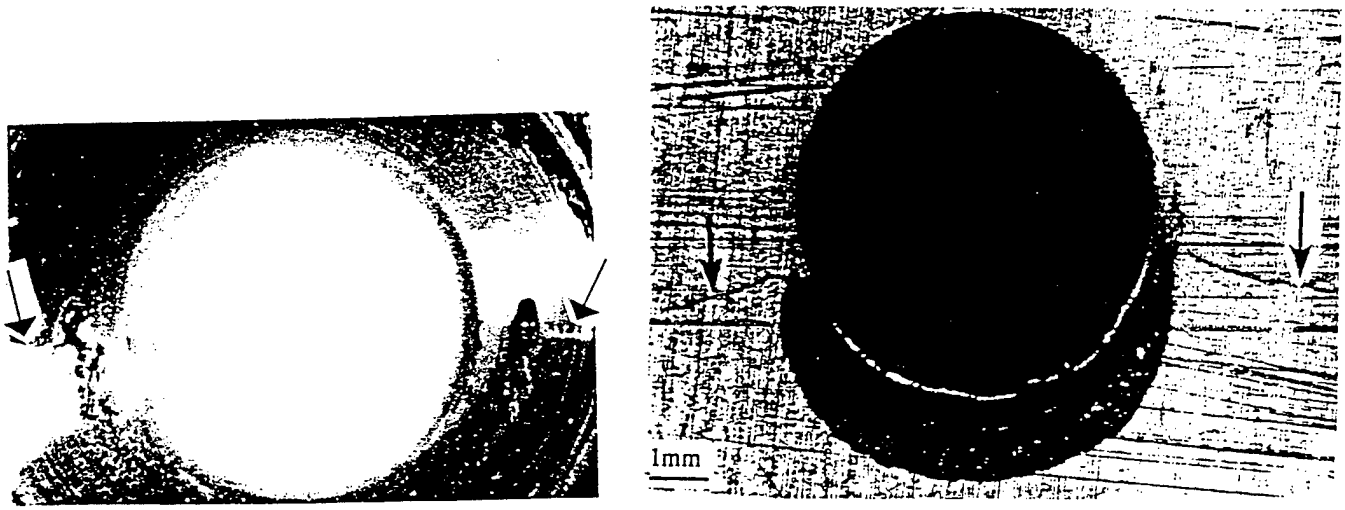

Figure 3. Important fretting fields observed in laboratory tested riveted lap joints.

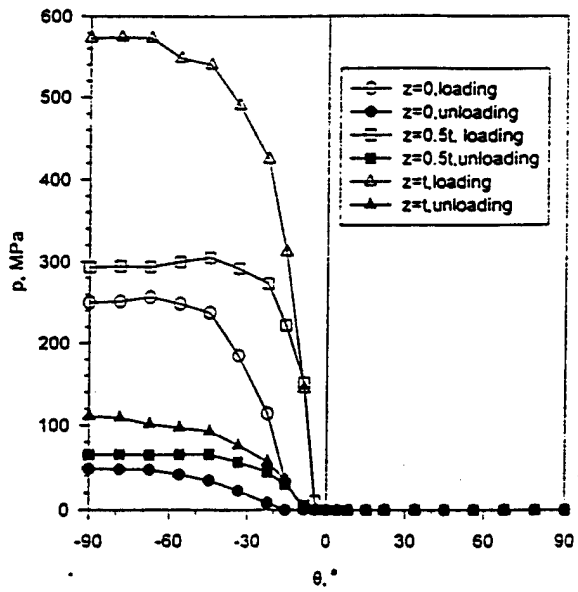

(a)

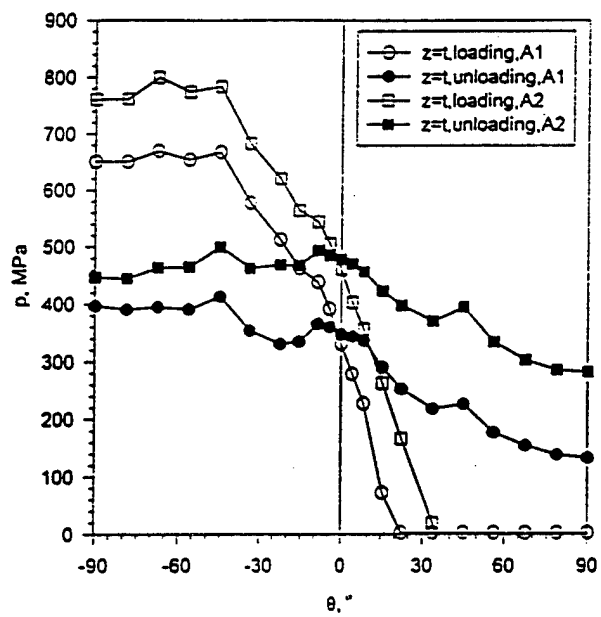

(b)

Figure 4. (a) Variation of contact pressure at the shank-hole interface with angular location and depth for Model A0, (b) Variation of contact pressure with angular location at depth z=t, where contact pressures peak, for Models A1 and A2.

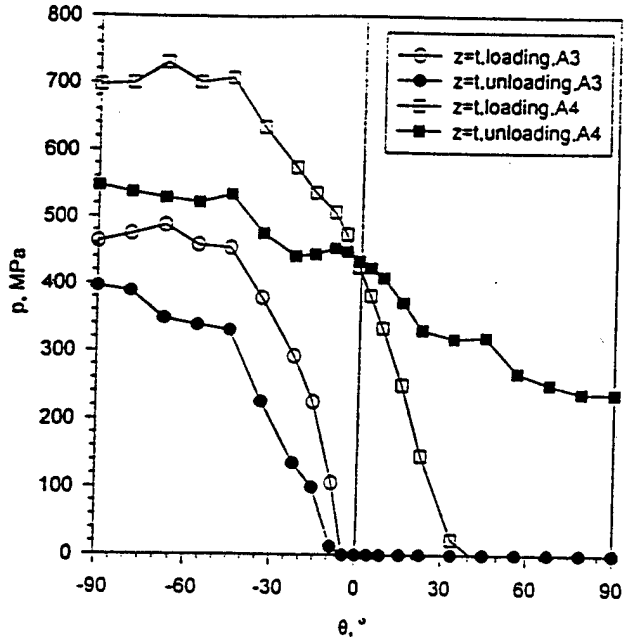

(a)

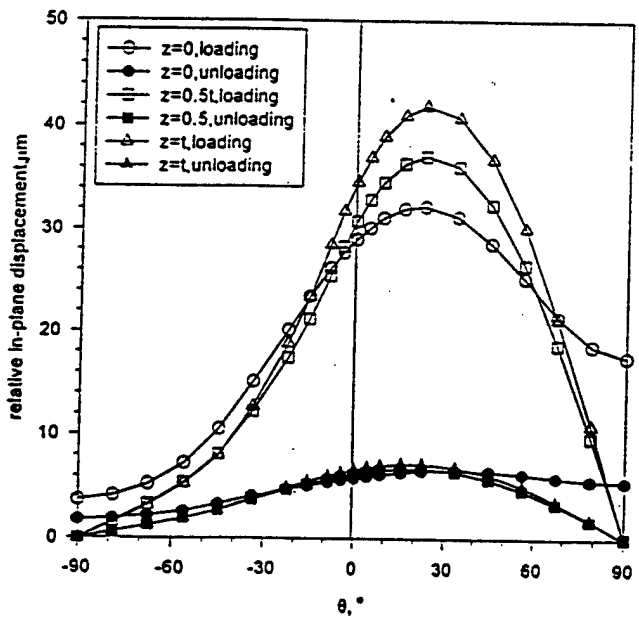

(b)

Figure 5. (a) Angular variation of contact pressure at the shank-hole interface in Models A3 and A4 at z=t, depth at which the pressures peak, (b) Variation of in-plane slip between the panel hole and rivet in Model A0.

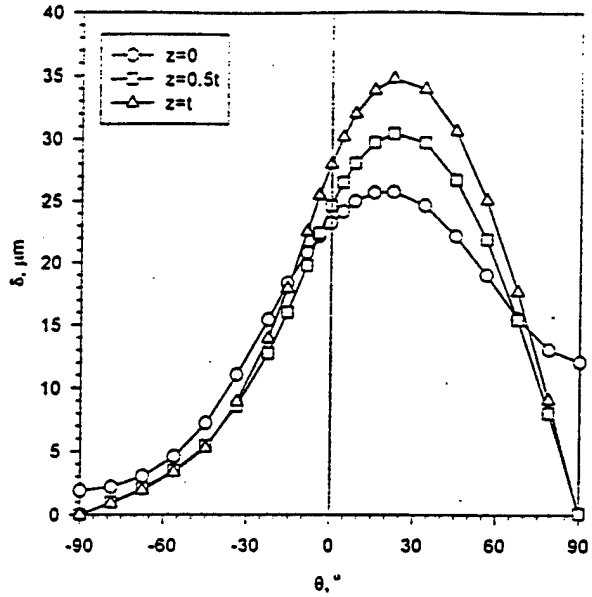

(a)

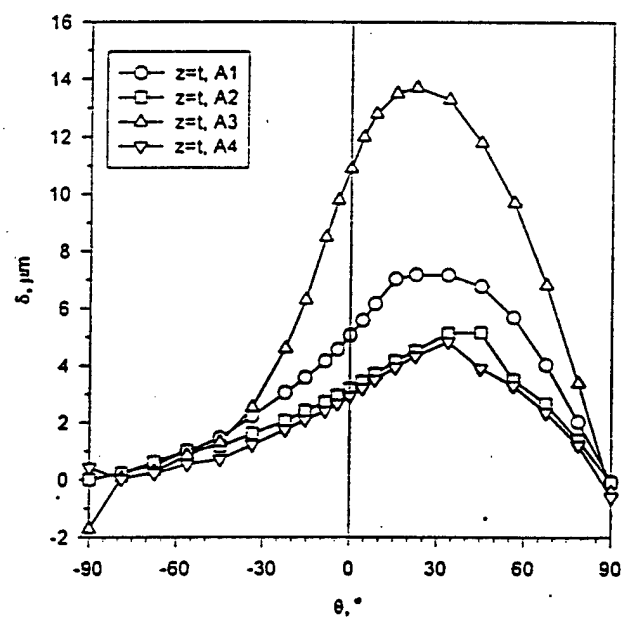

(b)

Figure 6. (a) Variation of in-plane slip amplitude at the shank-hole interface with angular location and depth for Model A0, (b) Angular variation in Models A1-A4 at depth z=t, where slip amplitudes peak.

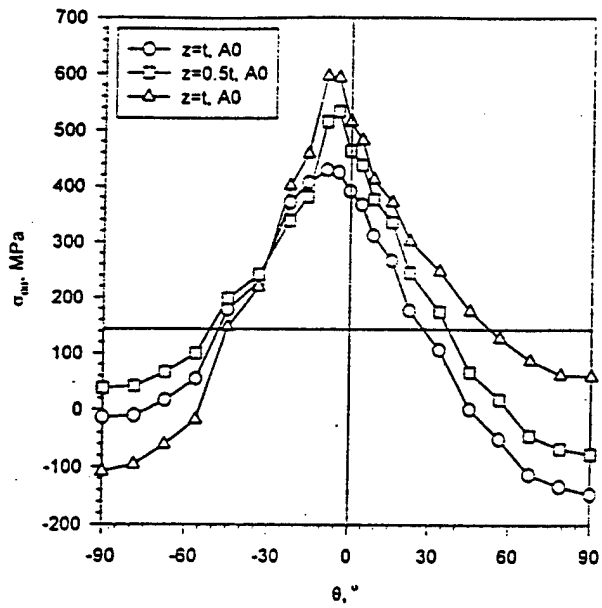

(a)

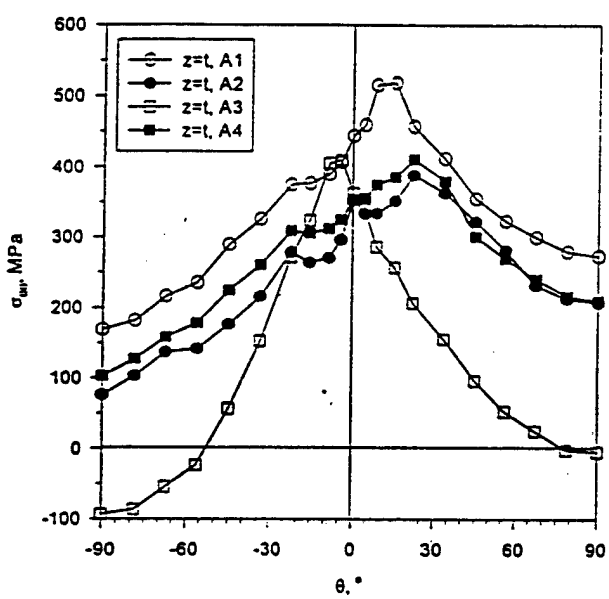

(b)

Figure 7. (a) Variation of circumferential tensile stress, $\sigma_{\theta\theta}$, in the panel and immediately adjacent to the hole surface under maximum load, with angular location and depth for Model A0, (b) Variation with angular location at z=t, depth at which tensile stresses are greatest, for Models A1-A4.

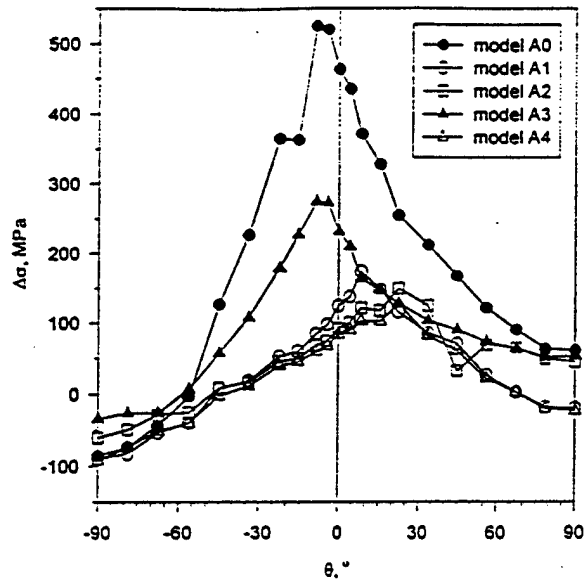

(a)

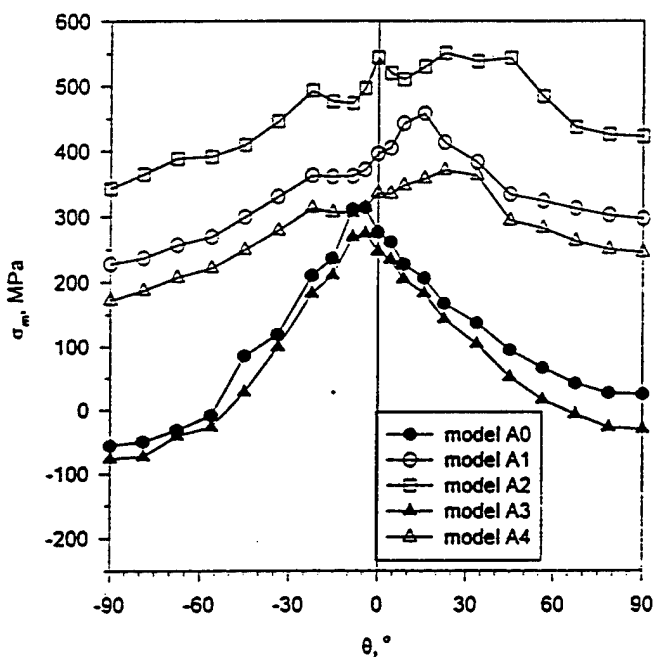

(b)

Figure 8. (a) Variation of conventional fatigue parameters at the rivet shank-panel hole interface at z=t. (a) cyclic stress range, $\Delta\sigma$, (b) mean stress, σ_m.

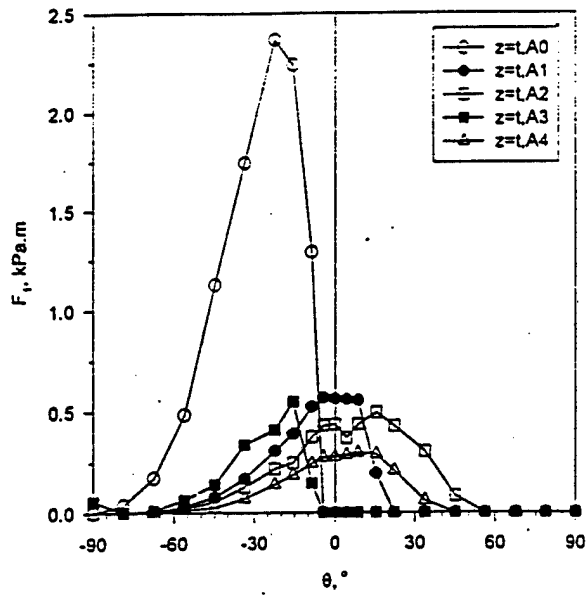

(a)

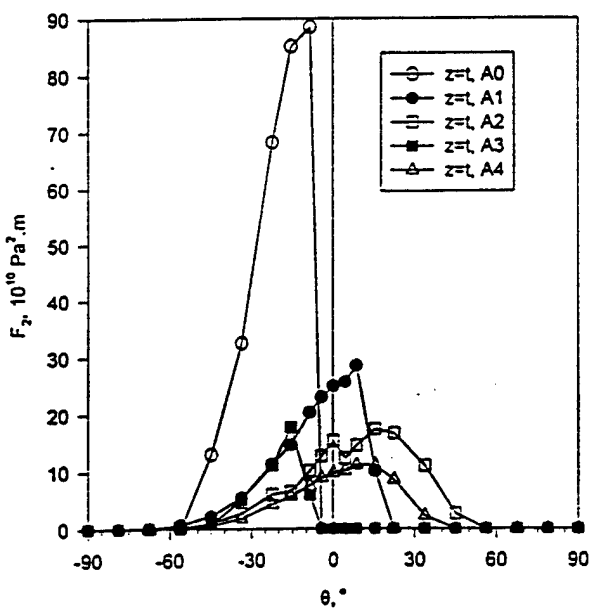

(b)

Figure 9. (a) Variation of the fretting wear parameter, F_1, with angular location at z=t, (b) Variation of the fretting fatigue parameter, F_2, depth at which both parameters peak.

APPENDIX B

Influence of interference and clamping on fretting fatigue in aluminum, single rivet-row lap joints - Part II: countersunk rivet

K. Iyer†, P. C. Bastias, C. A. Rubin, G. T. Hahn

Department of Mechanical Engineering
Box 1592, Station B
Vanderbilt University
Nashville, TN 37235

Abstract

Numerical evaluation of primary fretting fatigue variables at and near the contact interface between the rivet shank and panel hole in a single rivet-row, 7075-T6 aluminum alloy lap joint is presented. This article, the second part of a two-part paper, considers a countersunk rivet geometry with an included angle of 100°. Three-dimensional finite element analysis is applied to evaluate the effects of interference and clamping stresses on the variations of contact pressure, slip amplitude, bulk tensile stress, cyclic stress range, cyclic mean stress and two other mixed fretting fatigue variables. The beneficial effects of interference and clamping calculated for a non-countersunk rivet geometry in Part I are observed with countersinking also. Shifts in the peaks of the cyclic stress range and the mixed fretting fatigue parameters with varying interference and clamping may be exploited to extend the residual life of aging airframes.

List of Symbols

A	cross-sectional area of panel
L	overall length of riveted lap joint
E	Young's Modulus
σ_y	monotonic yield strength
σ_κ	kinematic yield strength
M	overall plastic modulus (including elastic slope contribution)
$\Delta\sigma$	cyclic stress range
σ_m	mean stress
P	applied load
Δ	total displacement
p	contact pressure
μ	coefficient of friction
τ	frictional shear stress. $\tau = \mu \cdot p$
λ	slip: amount of relative movement between contacting surfaces
δ	slip amplitude: amount of relative movement between contacting surfaces per load cycle
θ	angular location. The $\theta = 90^0$ direction corresponds with the positive direction of the 1-axis (tensile loading axis). 3 o'clock corresponds to $\theta = 0^0$, 6 o'clock to $\theta = -90^0$ etc.
$\sigma_{\theta\theta}$	local circumferential tensile stress, parallel and adjacent to contacting surfaces
F_1	fretting wear parameter. $F_1 = \tau \cdot \delta$
F_2	fretting fatigue parameter. $F_2 = \sigma_{\theta\theta} \cdot \tau \cdot \delta = \sigma_{\theta\theta} \cdot F_1$

† now with the Dept. of Mechanical Engineering and Applied Mechanics, University Of Michigan, 2250 G. G. Brown Bldg., Ann Arbor, MI, USA, 48109.

Introduction

Cracks at rivet holes in cyclically loaded airframe riveted lap joints initiate in regions showing fretting damage [1,2,3]. The location and life of fretting fatigue crack initiation in these structures depends primarily on the contact pressure (normal load), slip amplitude at the interface, frequency, material factors and environmental factors. The friction coefficient, its variation with slip amplitude, and tangential stresses generated at the interface, are determined by the material pair and the surface environment [4,5,6]. Apart from these factors, which determine fretting fatigue damage in any system involving contacting components, rivet installation during the assembly of a lap joint, prior to any loading, alters the initial elastic-plastic contact conditions, thus affecting the subsequent evolution of material response and fatigue damage.

The work presented here is a study of fretting fatigue in airframe aluminum alloy 7075-T6, single rivet-row lap joints and is compiled into two parts. This part presents results of the analysis of a joint with a countersunk rivet. The circumstances (contact pressure, slip amplitude, etc.) under which fretting fatigue damage accumulates are presented and interpreted in terms of existing approaches [7,8] to predict crack initiation locations. The reader is referred to Part I [9] for a more verbose introduction and results from the analysis of a single rivet-row lap joint with a non-countersunk rivet. Detailed analyses of the residual stresses that may be generated during rivet installation (interference and clamping) are presented elsewhere, independently [10]. They are applied here directly to account for the effects of interference and rivet clamping on fretting fatigue parameters. Rivet and panel shapes and dimensions, and the rivet spacing are patterned after those employed in airframes.

Analytical Procedures

Material Constitutive Relation Model

Crack initiation life in riveted assemblies has been shown to be a strong function of the interference and clamping stresses generated by rivet installation [11]. However, fretting fatigue cracks initiate after thousands of load cycles, by which time the material has attained a steady-state response whose characteristics are considerably different from those present at the time of rivet installation. Employing the monotonic material properties with the Isotropic hardening approximation for the installation step (interference and/or clamping) is justifiable if one assumes an initially isotropic medium. But after the initial loading, the kinematic yield strength may be exceeded in regions where significant compressive residual stresses are generated during the unloading cycle. There is then the possibility that these regions experience continuing cyclic plasticity and are, therefore, prone to conventional fatigue. Consequently, the analysis of the effects of interference and clamping on fretting fatigue requires calculations to be performed with tboth sets of material properties/hardening approximation pairs.

Material properties for the Isotropic hardening behavior are defined by E = 69 GPa, $\nu = 0.3$, σ_y = 530.75 MPa and M = 0.7 GPa. The material properties for the elastic-linear-kinematic-plastic (ELKP) hardening behavior are defined by E = 69 GPa, $\nu = 0.3$, σ_k = 369.9 MPa and M = 57.5 GPa, where M is the overall plastic modulus [12]. The ELKP representation has a lower yield point and a greater hardening slope.

Ideally, a single analysis would be capable of simulating the installation effects with Isotropic constitutive relations and then switching to the ELKP properties for the load cycle. However, such dynamic analyses are beyond the scope of present-day FEA. Instead, current analyses are constrained to utilizing a single material response curve. The residual stress state

because of rivet installation is determined by the Isotropic hardening analysis. These residual stresses are then superimposed on the stress state determined with the ELKP analysis and are interpreted as first-order representations of the steady state *prior to crack initiation.* Local cyclic stress range variations are not subject to any modifications since they are determined exclusively by the ELKP constitutive relations.

Finite Element Model

The model geometry consists of two partially overlapping sheets (panels) coupled by a countersunk rivet, shown in Fig. 1. This represents one half unit of a multi-riveted, single row, long panel extending in the positive and negative 2-directions. The repeat distance between successive units is 30.6 mm. The upper panel has a countersunk hole. The rivet has one standard head at its lower end and one head countersunk to a depth of half the thickness of a single sheet, the included angle being 100°. A nominal, remote cyclic load defined by $\Delta\sigma = 90$ MPa and R = 0.1 is applied at the non-lapping end face of the upper sheet while the corresponding face belonging to the lower sheet is fixed along the x-axis; the Cartesian systems (1,2,3) and (x,y,z) are equivalent. The symmetry and other boundary conditions are identical to those described in Part I [9]. Variations in friction coefficient, μ, with contact pressure and slip amplitude are neglected and a constant value of 0.4 has been assumed for all interfaces.

Table 1 indicates the amounts of interference and clamping misfits analyzed. A description of the procedure applied to model the rivet installation stresses may be found in Part I [9]. Actual rivets are installed by an upsetting process which simultaneously induces radial interference and vertical clamping. The present study does not attempt to simulate the installation

process itself but rather isolate the effects of interference and clamping as separate fatigue life parameters.

Results

Detailed analyses of the distortions of single rivet-row lap joints under a uniaxial load are described elsewhere [13,14]. Of primary concern in fretting fatigue is the identification of macroscopic rivet-panel and panel-panel contact areas, and these occur at four locations: (A) between the rivet shank and hole surfaces, (B) between the two panels, and (C) between the standard rivet head and panel surfaces, and (D) between the countersunk rivet head and countersunk hole surface. Each location represents a two-dimensional surface (field) along which fretting can occur. Figure 2 shows the intersection of the four fretting fields with the symmetry plane and a schematic which defines angular locations according to the global coordinate axes. Fretting field A arises from the predominantly in-plane slips, λ_{12}, between the countersunk hole surface and rivet shank and is coincident with the countersunk hole surface. Fretting field B is present because of the predominantly in-plane slips between a panel surface and the opposite panel hole edge; its plane is coincident with the relevant portion of the panel surface. Although field D may be considered to be a part of field A, a distinction is made on the basis of the predominant component of slip that causes fretting damage. Rivet tilt causes the sharp chisel edge of the countersunk head to rub against the countersunk hole surface and the slips possess a significant out-of-plane component, λ_{13}, responsible for fretting damage in field D. Contact between the standard rivet heads and panels (C) does not lead to any significant fretting damage [3]. Figure 3 shows the important fretting fields which arise from fatigue loading of lap joints with countersunk rivets. The cracks that lead to MSD typically form due to fretting between the

rivet shank and hole surfaces (A). Fretting damage in field B is restricted to severe plasticity and material loss without cracking owing to the beneficial bulk compressive stress field [14].

Results which follow focus on shank-hole fretting conditions and their repercussions on crack initiation there. Although slip amplitude vectors at any location possess in-plane, δ_{12}, and out-of-plane, δ_{13}, components, only the in-plane component is considered and presented given its predominance. The results presented for models B0 (without rivet installation effects) are for the ELKP material constitutive relation. Calculated variations of the local mean stress and bulk circumferential stress under maximum load are determined first for the ELKP constitutive relation, and then modified by the installation residual stress state using the Isotropic constitutive relation.

For the upper panel, Figs. 4-7 show the variations with angular location, θ, of the contact pressure the in-plane slip and the local, in-plane tensile stress parallel to the shank-hole interface. Table 2 shows values of some fretting fatigue variables at different locations through the hole depth. The countersunk case is not symmetric about the 1-2 plane at $z = t$ and the response of the upper (countersunk) portion of the assembly is not equivalent to the response of the lower (cylindrical) portion. Prior analysis [10,13,14] has shown that the asymmetric geometry introduces an imbalance in the response of the two portions with the countersunk half being subject to greater pressures, slips etc., in the absence of interference. However, when interference is present, the conventional fatigue variables such as $\Delta\sigma$, in the *lower*, straight-hole half have been shown to be slightly more damaging than in the upper, countersunk panel [10]. Further, it has been shown that the response of the lower, straight-hole panel of the countersunk assembly is very similar to that calculated for the panel holes in the non-countersunk assembly. Thus, since the fretting fatigue conditions around the lower panel (straight) hole are very similar to those

calculated in Part I, the results in this section focus on the upper, countersunk hole interface only. Variations through the depth of the countersunk hole and with angular location are presented in the same manner as in Part I.

Inherent to the countersunk rivet geometry is the presence of the contact field D (Fig. 2 (a)) which arises due to slippage of the sharp chisel edge of the countersunk rivet head (rivet tilt) along the countersunk hole surface when the assembly is loaded. In the absence of interference and clamping, the peak contact pressure associated with this field is about 250 MPa at 90° (see Fig. 4(a)). Contact pressures are registered at those interface elements initially at z = 0 and decrease gently towards 0°. Peak shank-hole contact pressures of about 800 MPa are produced at z = t upon loading in the absence of interference and clamping. Contact between the rivet shank and hole is lost at -8.7° at z = t under load. The shift in this location because of interference is towards 90° (loading direction). Pure interference increases the loaded shank-hole contact pressure, the peak value rising to about 1020 MPa at z = t, with 2% interference. Pure clamping does little to change the loaded contact pressure at z = t but restricts unloading, and the peak unloaded pressures increase by more than 200%. Interference and clamping lower slip amplitudes as expected. Table 2 and Fig. 7 show that the slips in contact field D (z = 0) are high and comparable to those in field A (z = t). In general, the effect of 0.5% clamping becomes insignificant when combined with 2% interference.

Figure 7 shows the variation of circumferential tensile stresses in the panel hole and immediately adjacent to the shank-hole interface. The bulk loaded stress associated with field D (z = 0) is compressive over the region associated with significant contact pressures and slip amplitudes.

Fatigue and Fretting Fatigue

Figure 8 shows the angular variation of the local cyclic stress range, $\Delta\sigma$ and local mean stress, σ_m, at z = t. In the absence of interference and clamping, the applied, nominal cyclic stress range, $\Delta\sigma$ = 90 MPa, results in a peak $\Delta\sigma$ of about 900 MPa at -8.7°. The effects of interference are the same as those observed with the non-countersunk rivet [9]. Variations of the mechanistic parameters, F_1 and F_2, with angular location at z = t are shown in Fig. 9. In the absence of interference and clamping the peak value of F_1 is about 3.9 kPa.m and is present at -22.5°. Interference and clamping lower the magnitudes of F_1 and F_2 and blunted peaks persist over a range of angular locations, which have been shifted towards the loading end (90°). Clamping does not alter the location of the peaks. Table 3 shows the peaks of the mechanistic parameters through the depth of the shank-hole interface.

Discussion

Angular variations of F_1 and F_2 at z =t at and adjacent to the lower, straight-hole interface, which are not shown, indicate the peak F_1 values of 0.53 kPa.m and 0.38 kPa.m with 1% and 2% interference respectively; the peak F_2 values are $22.9 \cdot 10^{10}$ Pa^2.m and 14.8 $\cdot 10^{10}$ Pa^2.m respectively. These are comparable or higher than the peak values of these parameters for the upper, countersunk hole, listed in Table 3. The implication is that there are values of interference which equalize the likelihood of crack initiation in both the countersunk (upper) and cylindrical (lower) panel holes after a certain number of load cycles. Peak F_1 and F_2 values for the lower panel in the present models are very similar to those calculated in the non-countersunk models [9] for the same amount of interference and have not been shown for this reason.

Relative shifts in the angular locations of the peaks of $\Delta\sigma$ and F_2 suggest a functional modification that may be applied to optimize the residual life of aging airframes. Installing adjacent rivets in a given rivet-row with different amounts of interference and clamping can offset the growth trajectories and limit interaction of neighboring cracks growing towards each other. For example, in the absence of interference and clamping and with a countersunk rivet, $\Delta\sigma$ peaks at -8.7° and F_2 peaks at -22.5°; 1% interference shifts the peaks to 15.6° and -4.3° respectively.

The value of F_2 is a more sensitive function of applied load than the peak value of $\Delta\sigma$. The fretting fatigue parameter depends on the interfacial shear stress, slip amplitude and bulk circumferential stress, $\Delta\sigma$. Consequently, a two-fold reduction in applied load can, for example, lead to a two-fold reduction in $\Delta\sigma$ but an eight-fold reduction in F_2. Thus fretting fatigue may be viable when conventional fatigue is not.

It is well known that the primary variables that promote fretting fatigue crack initiation are the contact pressure, p, slip amplitude, δ, friction coefficient, μ, and the tensile stress component adjacent and parallel to the rivet hole, $\sigma_{\theta\theta}$. The slip amplitude *at* the contact interface is directly related to the cyclic plasticity there. However, additional variables that drive conventional fatigue crack initiation must not be overlooked. These include the local values of repeat plasticity, $\Delta\varepsilon_{\theta\theta}$, cyclic stress range, $\Delta\sigma_{\theta\theta}$, and mean stress, $(\sigma_m)_{\theta\theta}$. The present work presents the evaluation of the variations of most of these parameters and F_2 as a more complete indicator for crack initiation location prediction. However, it may be asserted that a more universally applicable and fundamentally sound indicator is necessary and must include all the parameters mentioned above. If this universal parameter is denoted by Ψ, then it may be of the form,

$$\Psi = (p)^a \bullet (\delta)^b \bullet (\mu)^c \bullet (\sigma_{\theta\theta})^d \bullet (\Delta\sigma_{\theta\theta})^e \bullet ((\sigma_m)_{\theta\theta})^f \bullet (\Delta\varepsilon_{\theta\theta})^g$$

where a, b, c, d, e, f and g are real. Dependent variables in the above equation may disappear which would reflect on the value of the exponent of the parent variable.

Conclusions

1. Primary fretting fatigue variables in a single rivet-row lap joint have been evaluated for different amounts of interference, clamping and a countersunk rivet geometry.

2. In the absence of interference, fretting fatigue crack initiation in the countersunk panel will occur first. However, some values of interference can cause the fretting fatigue crack to initiate in lower (cylindrical) panel hole.

3. For some values of interference, a lap joint with a non-countersunk rivet may be inferior to one with a countersunk rivet.

4. The combination of interference and clamping is better than either considered singly, in lessening the threat of crack initiation.

5. Peaks in the angular variations of conventional fatigue parameters and the fretting fatigue parameter, F_2, are usually distinct. This offers a basis to identify the relative weights of the primary variables that drive crack initiation.

6. The fretting wear parameter, F_1, is a reliable indicator of fretting wear zones.

7. It is proposed that the shift (interference) or lack thereof (clamping), of the angular locations of the peaks of the fretting fatigue parameters can be exploited to optimize the residual life of aging airframes. Installing adjacent rivets in a given row with different amounts of interference and clamping can offset the growth trajectories and limit or postpone interaction of adjacent cracks growing towards each other.

Acknowledgments

The authors are grateful to Hibbitt, Karlsson and Sorensen, Inc. for permission to use their finite element code ABAQUS. This research was supported with a grant from the Air Force Office of Scientific Research (F49620-93-1-0488).

References

[1] Adibnazari, S. and Hoeppner, D. W., "Study of fretting crack nucleation in 7075-T6 aluminum alloy," Wear, 159 (1992), pp. 257-264.

[2] Piascik, R. S., "The characterization of widespread fatigue damage in fuselage structure," NASA technical memorandum, 109142, Langley Research Center, 1994.

[3] Iyer, K., Xue, M., Kasinadhuni, R., Bastias, P. C., Rubin, C. A., Wert, J. J. and Hahn, G. T., "Contribution of fretting to the fatigue and corrosive deterioration of a riveted lap joint," Proc. Symp. Structural Integrity in Aging Aircraft, San Francisco, Nov. 15, 1995.

[4] Waterhouse, R. B., "Fretting corrosion," Pergamon Press, New York, 1972.

[5] Waterhouse, R. B., "Avoidance of fretting fatigue failures," in Fretting Fatigue, pp. 221-240, Ed. R. B. Waterhouse, Applied Science Publishers Ltd. (ISBN 0-85334-932-0), London, 1981.

[6] Waterhouse, R. B., "Fretting wear," ASM Metals Handbook, No. 18, pp. 242-256, 1992.

[7] Ruiz, C., Boddington, P. and Chen, K., "An investigation of fatigue and fretting in dovetail joints," Exp. Mech., v 24, 1984, pp. 208-217.

[8] Nowell, D. and Hills, D. A., "Crack initiation criteria in fretting fatigue," Wear, 136 (1990), pp. 329-343.

[9] Iyer, K., Bastias, P. C., Rubin, C. A. and Hahn, G. T., "Influence of interference and clamping on fretting fatigue in aluminum, single rivet-row lap joints – Part I: non-countersunk rivet," submitted to Wear.

[10] Iyer, K., Bastias, P. C., Rubin, C. A. and Hahn, G. T., "Influence of interference and clamping on distortions and fatigue in aluminum, single rivet-row lap joints," to be published.

[11] Muller, R. P. G., "An experimental and analytical investigation on the fatigue behavior of fuselage riveted lap joints – the significance of the rivet squeeze force, and a comparison of 2024-T3 and Glare 3," Ph.D. dissertation (1995), Delft University of Technology, The Netherlands.

[12] Hahn, G. T., Bhargava, V. and Chen, Q., "The cyclic stress-strain properties, hysteresis loop shape and kinematic hardening of two high strength bearing steels," Met. Trans. A, v 21A (1990), pp. 653-664.

[13] Iyer, K., Bastias, P. C., Rubin, C. A. and Hahn, G. T., "Three-dimensional analyses of single rivet-row lap joints - Part I: Elastic Response," to be submitted to ASME J of App. Mech.

[14] Iyer, K., Bastias, P. C., Rubin, C. A. and Hahn, G. T., "Three-dimensional analyses of single rivet-row lap joints - Part I: Elastic-Plastic Response," to be submitted to ASME J of App. Mech.

List of Tables

1. The finite element models.

2. Variation of fretting fatigue variables through the depth of the countersunk (upper panel) hole.

3. Summary of mechanistic parameters indicating locations of fretting wear and crack initiation in lap joint assemblies with countersunk rivets.

List of Figures

1. (a) Multi-riveted, single rivet-row lap joint, of which one half-unit is considered for the 3D half-symmetry finite element model, (b) the thickness of each panel is t=1.53 mm. The rivet is countersunk with an included angle of 100° and a shank diameter of 6.12 mm; the rivet head diameter and height are 9.792 mm and 3.83 mm respectively, (c) plan view of the mesh. The overall length of the model is 306 mm, the length of the overlap region is 30.6 mm and the width of the model (half the repeat distance) is 15.3 mm.

2. (a) Profile of a deformed mesh showing the four main rivet-panel and panel-panel fretting fatigue contact locations, (b) Schematic showing the definition of the angular locations and depth in the models.

3. Important fretting fields observed in laboratory tested riveted lap joints.

4. (a) Variation of contact pressure at the shank-hole interface with angular location and depth for Model B0, (b) Variation of contact pressure with angular location at depth z=t, where contact pressures peak, for Models B1 and B2.

5. (a) Angular variation of contact pressure at the shank-hole interface in Models B3 and B4 at z=t, depth at which the pressures peak, (b) Variation of in-plane slip between the panel hole and rivet in Model B0.

6. (a) Variation of in-plane slip amplitude at the shank-hole interface with angular location and depth for Model B0, (b) Angular variation in Models B1-B4 at depth z=t, where slip amplitudes peak.

7. (a) Variation of circumferential tensile stress, $\sigma_{\theta\theta}$, in the panel and immediately adjacent to the hole surface under maximum load, with angular location and depth for Model B0, (b) Variation with angular location at z=t, depth at which tensile stresses are greatest, for Models B1-B4.

8. Variation of conventional fatigue parameters at the rivet shank-panel hole interface at z=t. (a) cyclic stress range, $\Delta\sigma$, (b) mean stress, σ_m.

9. (a) Variation of the fretting wear parameter, F_1, with angular location at z=t, (b) Variation of the fretting fatigue parameter, F_2, depth at which both parameters peak.

Table 1. The finite element models.

Model	Rivet Heads	% Shank Radial Interference	% Shank Height Interference (Clamping)
B0	1 standard 1 countersunk (100^0) to half panel thickness	0	0
B1	1 standard 1 countersunk (100^0) to half panel thickness	1	0
B2	1 standard 1 countersunk (100^0) to half panel thickness	2	0
B3	1 standard 1 countersunk (100^0) to half panel thickness	0	0.5
B4	1 standard 1 countersunk (100^0) to half panel thickness	2	0.5

Table 2. Variation of fretting fatigue variables through the depth of the countersunk (upper panel) hole.

Model		Installation $\sigma_{\theta\theta}$ (MPa)	Peak $\sigma_{\theta\theta}$ (MPa)	Peak δ_{12} (μm)
B0	z=0	0	199.3	51.5
	z=0.5t	0	726.1	47.0
	z=t	0	**933.0**	**55.6**
B1	z=0	159	198.7	4.3
	z=0.5t	**102**	336.9	7.6
	z=t	269	**544.2**	**10.6**
B2	z=0	281	303.4	2.1
	z=0.5t	**-198**	-65.7	2.3
	z=t	132	**297.2**	**4.2**
B3	z=0	1	202.8	39.1
	z=0.5t	-1	651.2	37.6
	z=t	29	**848.8**	**45.2**
B4	z=0	265	282.0	2.1
	z=0.5t	**-200**	-72.6	2.1
	z=t	179	**346.8**	**4.2**

* Installation $\sigma_{\theta\theta}$ values are from the analyses with the Isotropic hardening approximation [10].

Table 3. Summary of mechanistic parameters indicating locations of fretting wear and crack initiation in lap joint assemblies with countersunk rivets.

		Peak Tangential Stress (MPa)		**Peak F_1 (kPa.m)**		**Peak F_2 (10^{10} Pa^2.m)**	
Model		**magnitude (MPa)**	**θ, °**	**magnitude (kPa.m)**	**θ, °**	**magnitude (10^{10} Pa^2.m)**	**θ, °**
B0	z=0	99	45.0, 78.8	**4.90**	**67.5, 90.0**	30.4	-4.3
	z=0.5t	172	-56.3, -45.0	2.52	-22.5, -15.6	140.0	-15.6
	z=t	**309**	**-45.0**	**3.90**	**-22.5**	**297.4**	**-22.5**
B1	z=0	204	56.3, 78.8	**0.85**	**78.8, 90.0**	4.1	0.0, 8.7
	z=0.5t	112	4.3, 15.6	0.60	15.6, 22.4	18.8	22.4
	z=t	**134**	**-22.5, -8.7**	**0.70**	**-8.7, -4.3**	**30.0**	**-4.3**
B2	z=0	238	67.5, 78.8	**0.38**	**78.8, 90.0**	4.5	15.6, 22.4
	z=0.5t	**113**	**15.6, 33.7**	0.24	15.6, 33.7	-	-
	z=t	**111**	**-8.7, -4.33**	**0.33**	**-8.7, 4.3**	**7.7**	**-4.3, 4.3**
B3	z=0	108	45.0, 78.7	**3.9**	**67.5, 90.0**	18.5	15.6
	z=0.5t	199	-45.0	2.1	-22.5, -8.7	102.8	-8.7
	z=t	**291**	**-45.0**	**3.0**	**-22.5**	**162.8**	**-22.5, -15.6**
B4	z=0	**236**	**67.5, 90.0**	**0.22**	**78.8, 90.0**	3.77	15.6, 22.4
	z=0.5t	121	33.7, 45.0	**0.24**	**15.6, 45.0**	-	-
	z=t	85	-8.7, -4.3	**0.25**	**-4.3, 8.7**	**7.1**	**-4.3, 0**

* two angular locations indicates the range over which a peak persists.
- indicates compressive, bulk stresses, and F_2 does not have any significance.

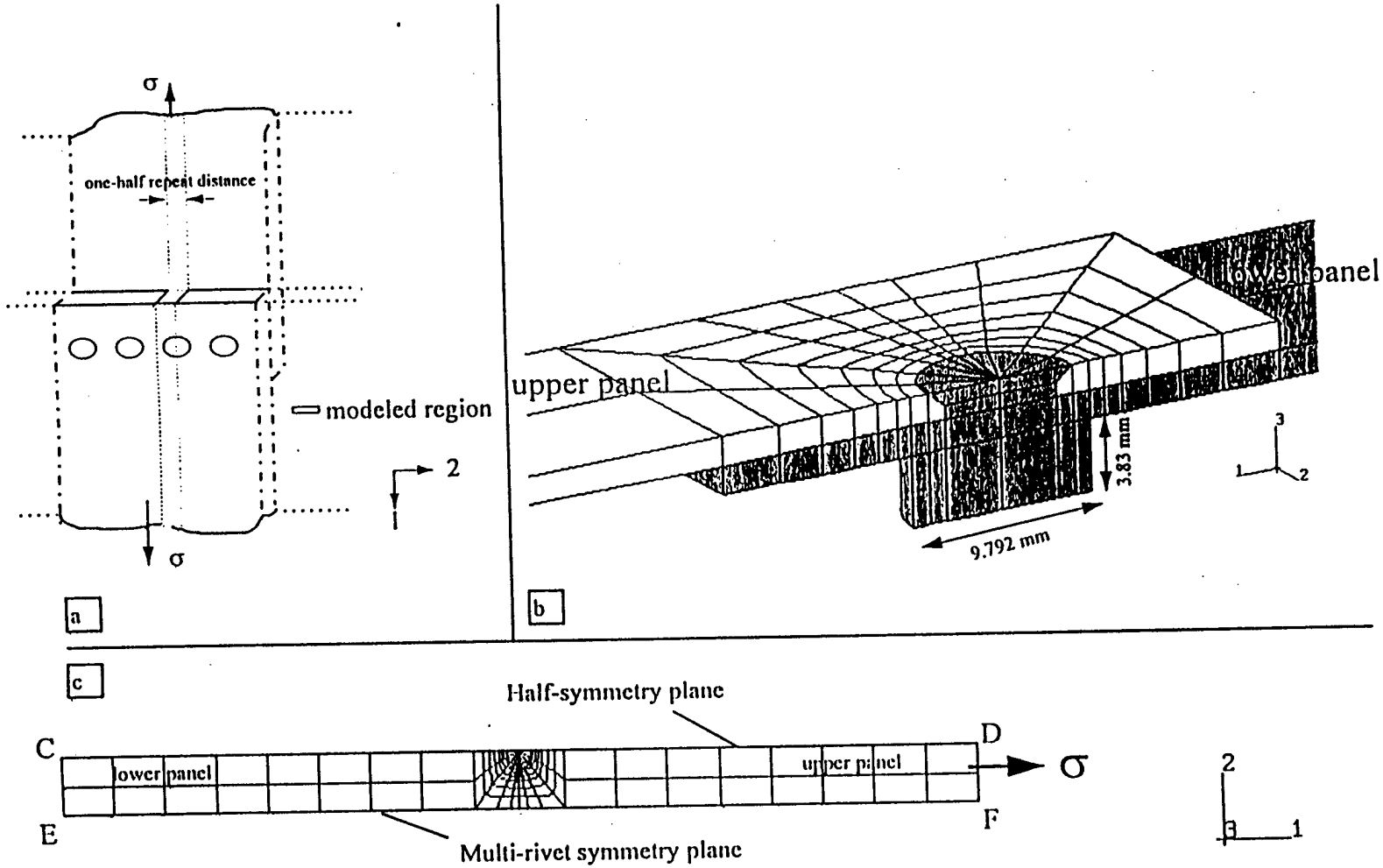

Figure 1. (a) Multi-riveted, single rivet-row lap joint, of which one half-unit is considered for the 3D half-symmetry finite element model, (b) the thickness of each panel is t=1.53 mm. The rivet is countersunk with an included angle of 100° and a shank diameter of 6.12 mm; the rivet head diameter and height are 9.792 mm and 3.83 mm respectively, (c) plan view of the mesh. The overall length of the model is 306 mm, the length of the overlap region is 30.6 mm and the width of the model (half the repeat distance) is 15.3 mm.

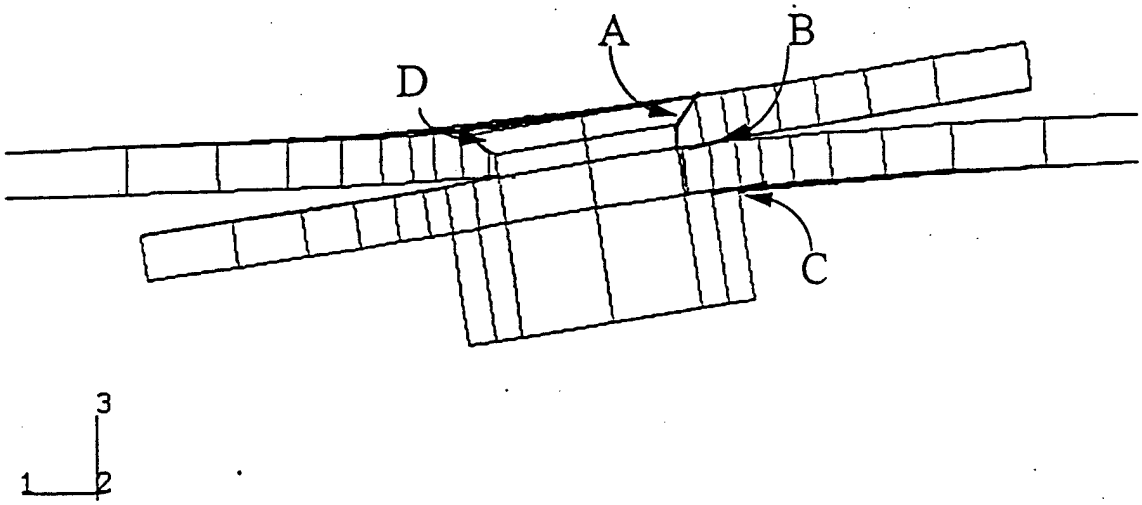

(a)

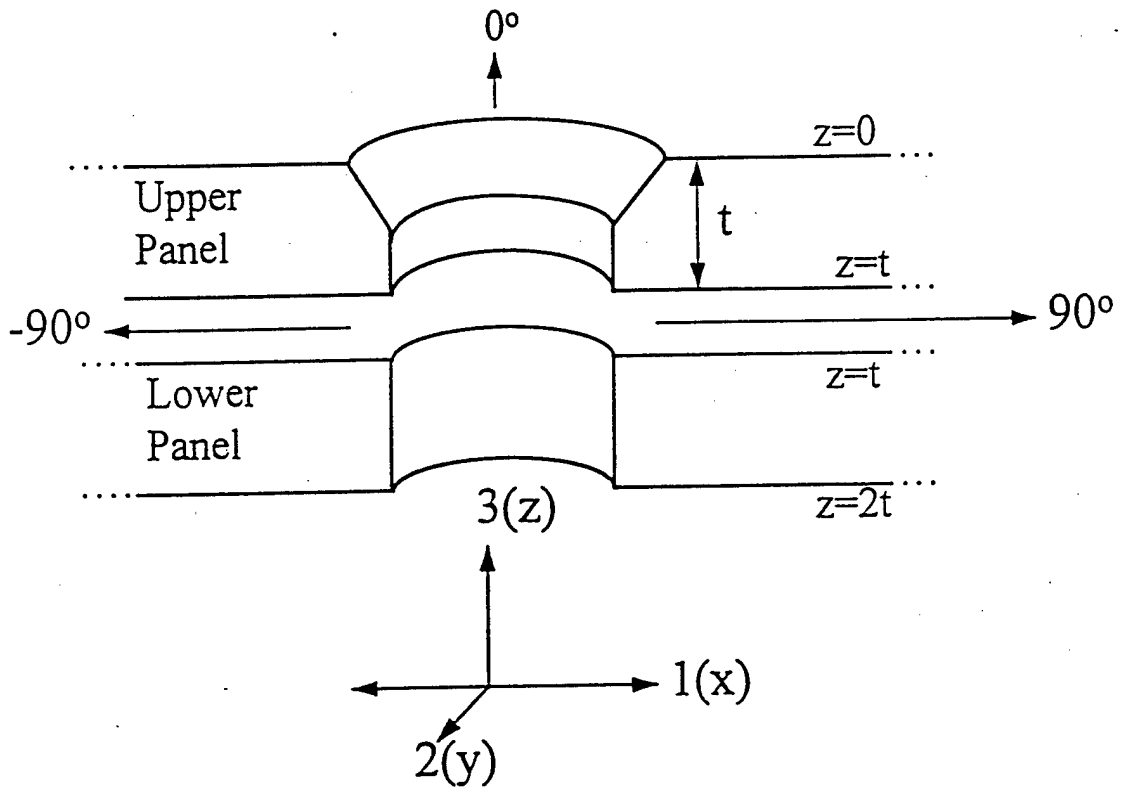

(b)

Figure 2. (a) Profile of a deformed mesh showing the four main rivet-panel and panel-panel fretting fatigue contact locations, (b) Schematic showing the definition of the angular locations and depth in the models.

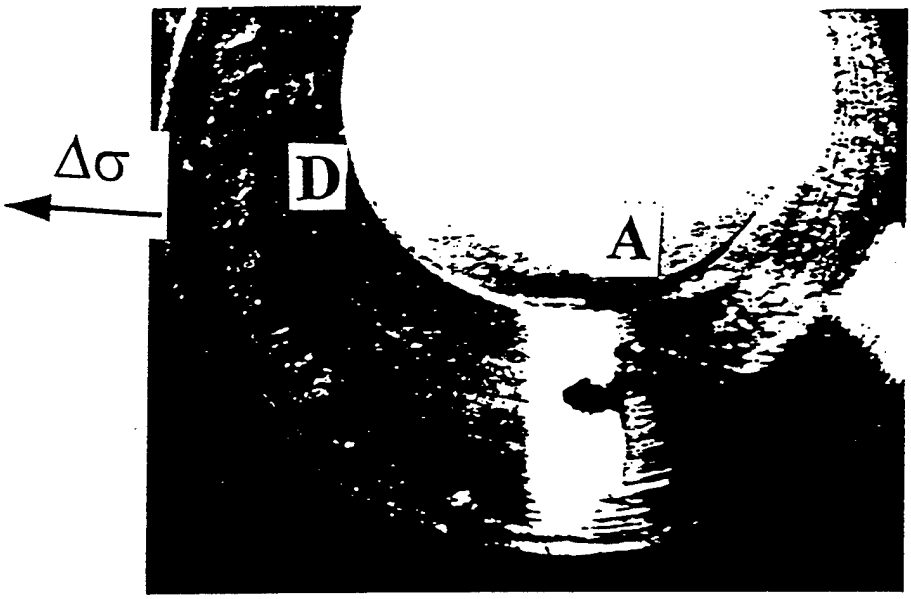

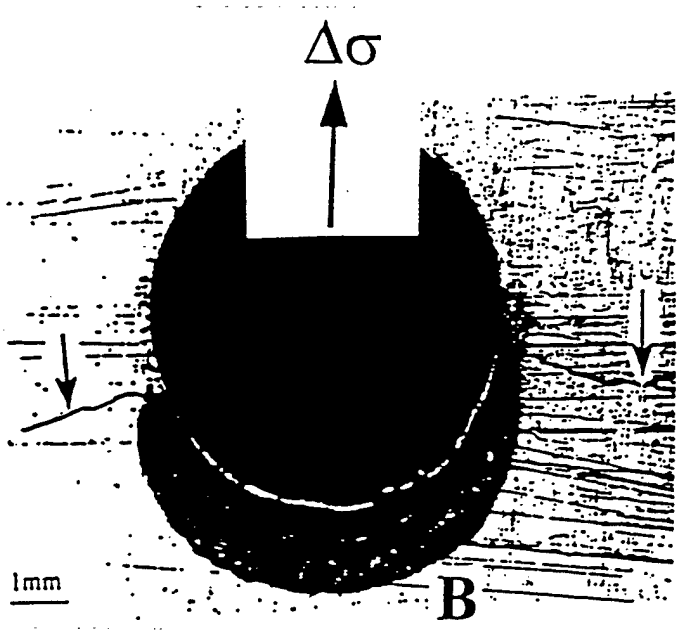

Figure 3. Important fretting fields observed in laboratory tested riveted lap joints.

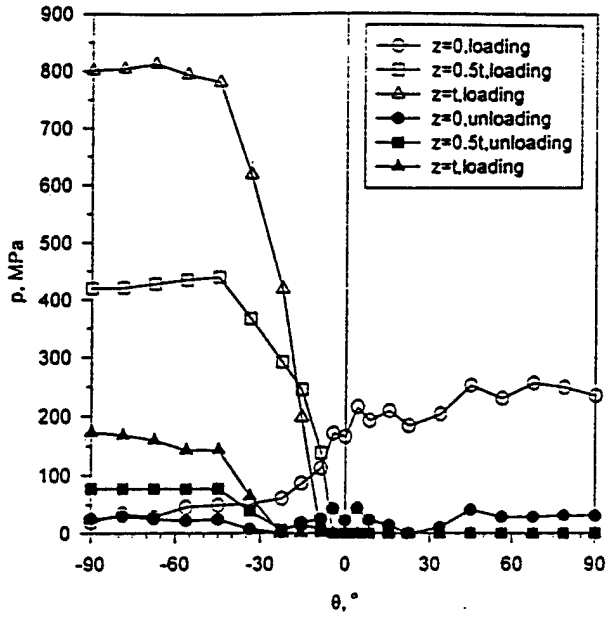

(a)

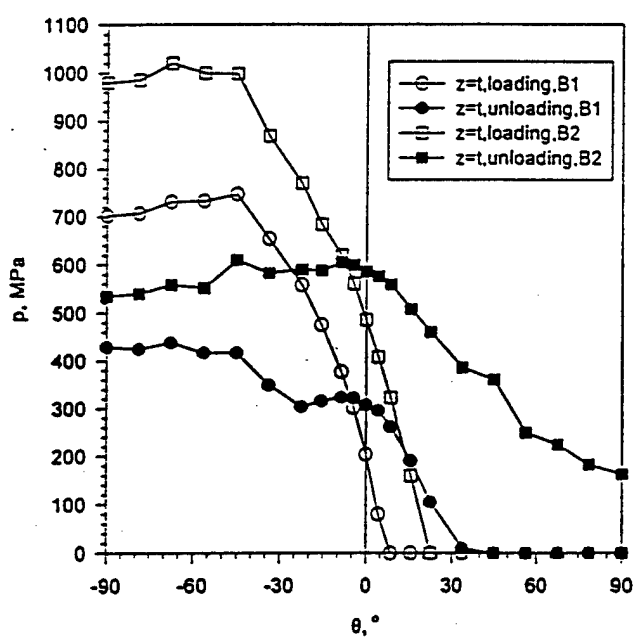

(b)

Figure 4. (a) Variation of contact pressure at the shank-hole interface with angular location and depth for Model B0, (b) Variation of contact pressure with angular location at depth z=t, where contact pressures peak, for Models B1 and B2.

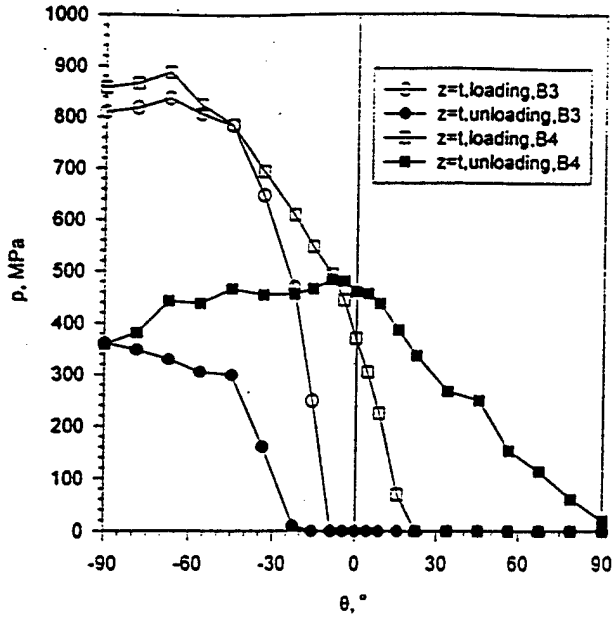

(a)

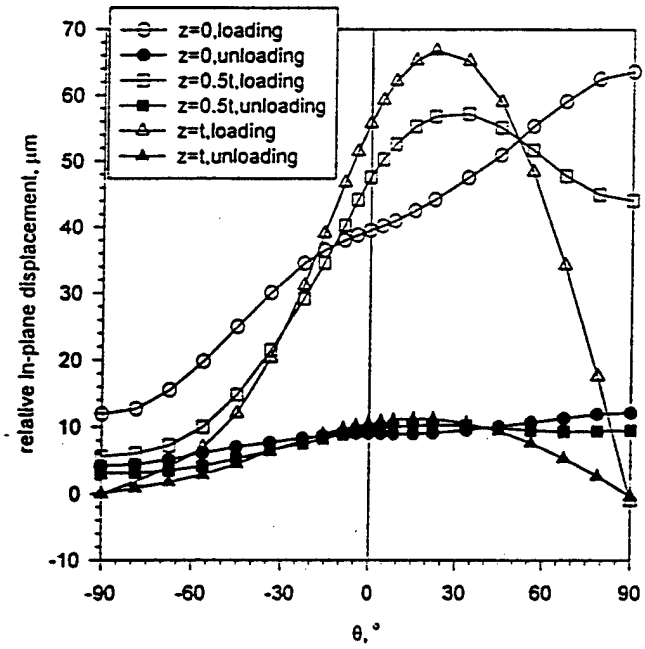

(b)

Figure 5. (a) Angular variation of contact pressure at the shank-hole interface in Models B3 and B4 at z=t, depth at which the pressures peak, (b) Variation of in-plane slip between the panel hole and rivet in Model B0.

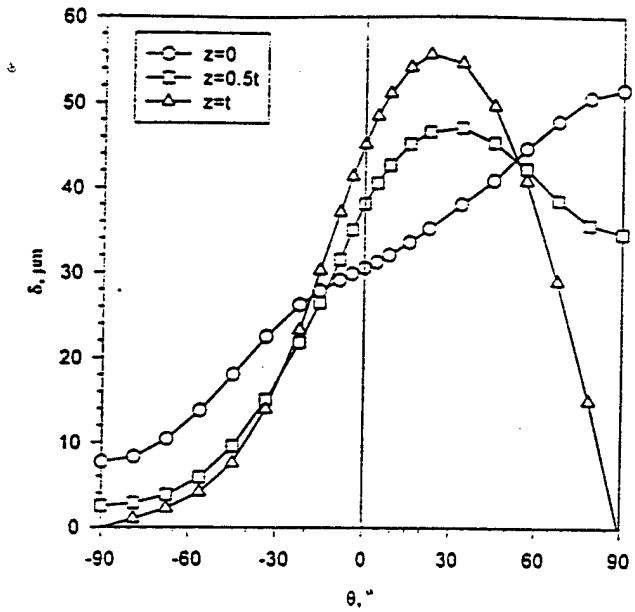

(a)

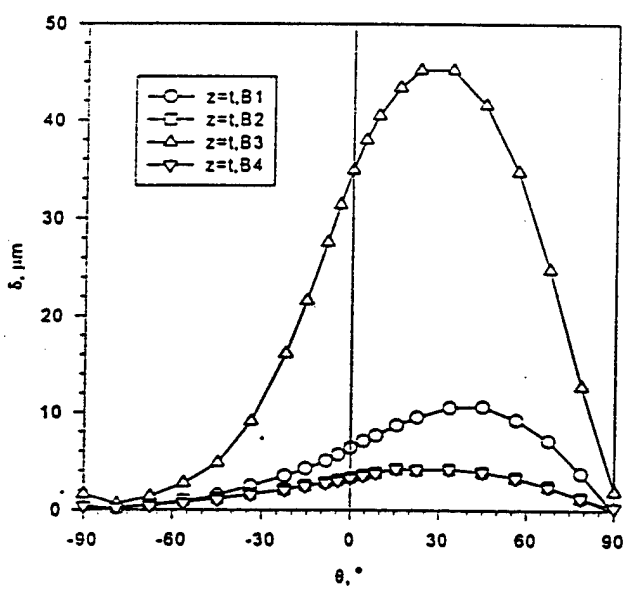

(b)

Figure 6. (a) Variation of in-plane slip amplitude at the shank-hole interface with angular location and depth for Model B0, (b) Angular variation in Models B1-B4 at depth z=t, where slip amplitudes peak.

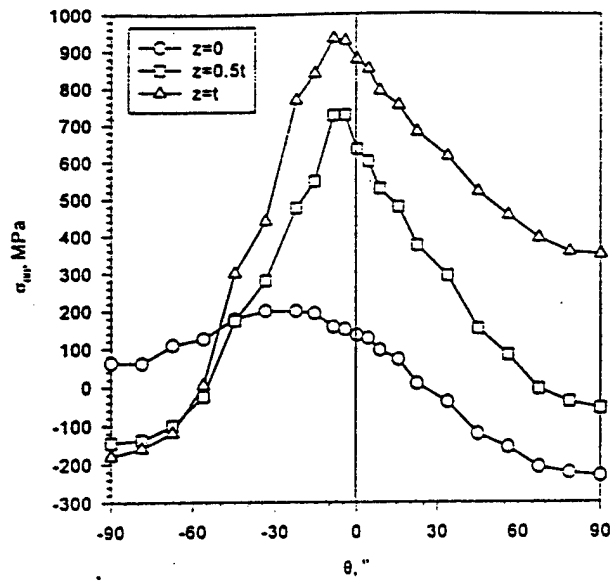

(a)

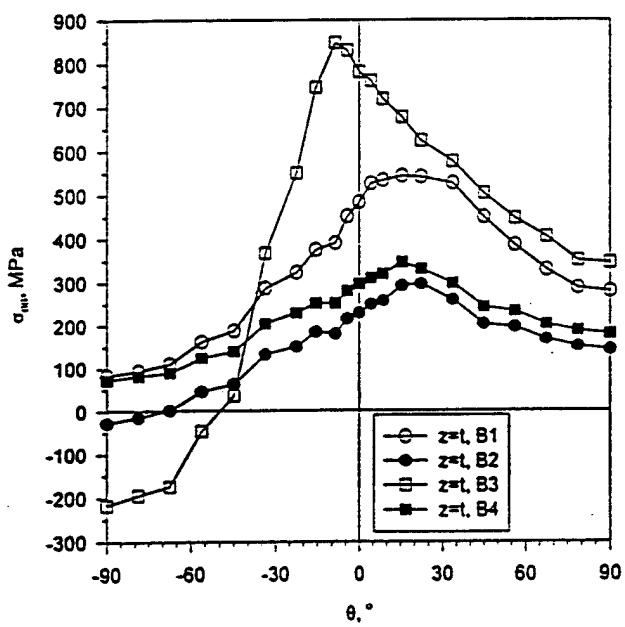

(b)

Figure 7. (a) Variation of circumferential tensile stress, $\sigma_{\theta\theta}$, in the panel and immediately adjacent to the hole surface under maximum load, with angular location and depth for Model B0, (b) Variation with angular location at z=t, depth at which tensile stresses are greatest, for Models B1-B4.

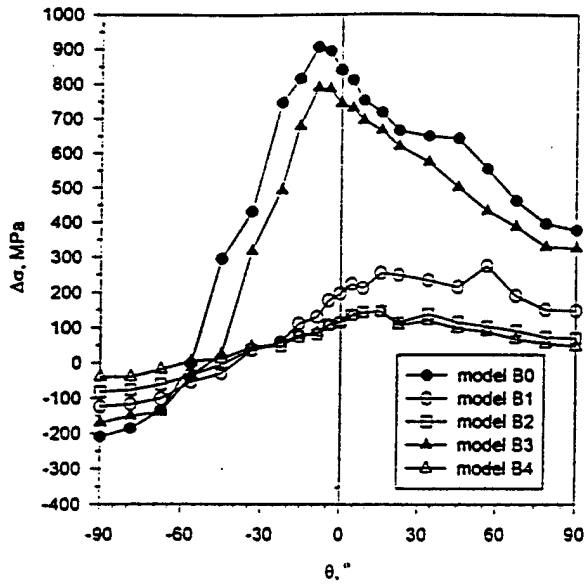

(a)

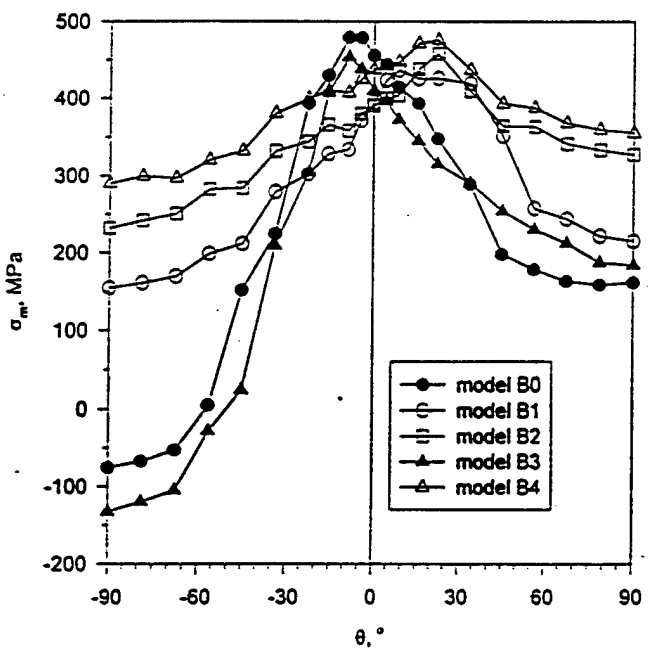

(b)

Figure 8. (a) Variation of conventional fatigue parameters at the rivet shank-panel hole interface at z=t. (a) cyclic stress range, $\Delta\sigma$, (b) mean stress, σ_m.

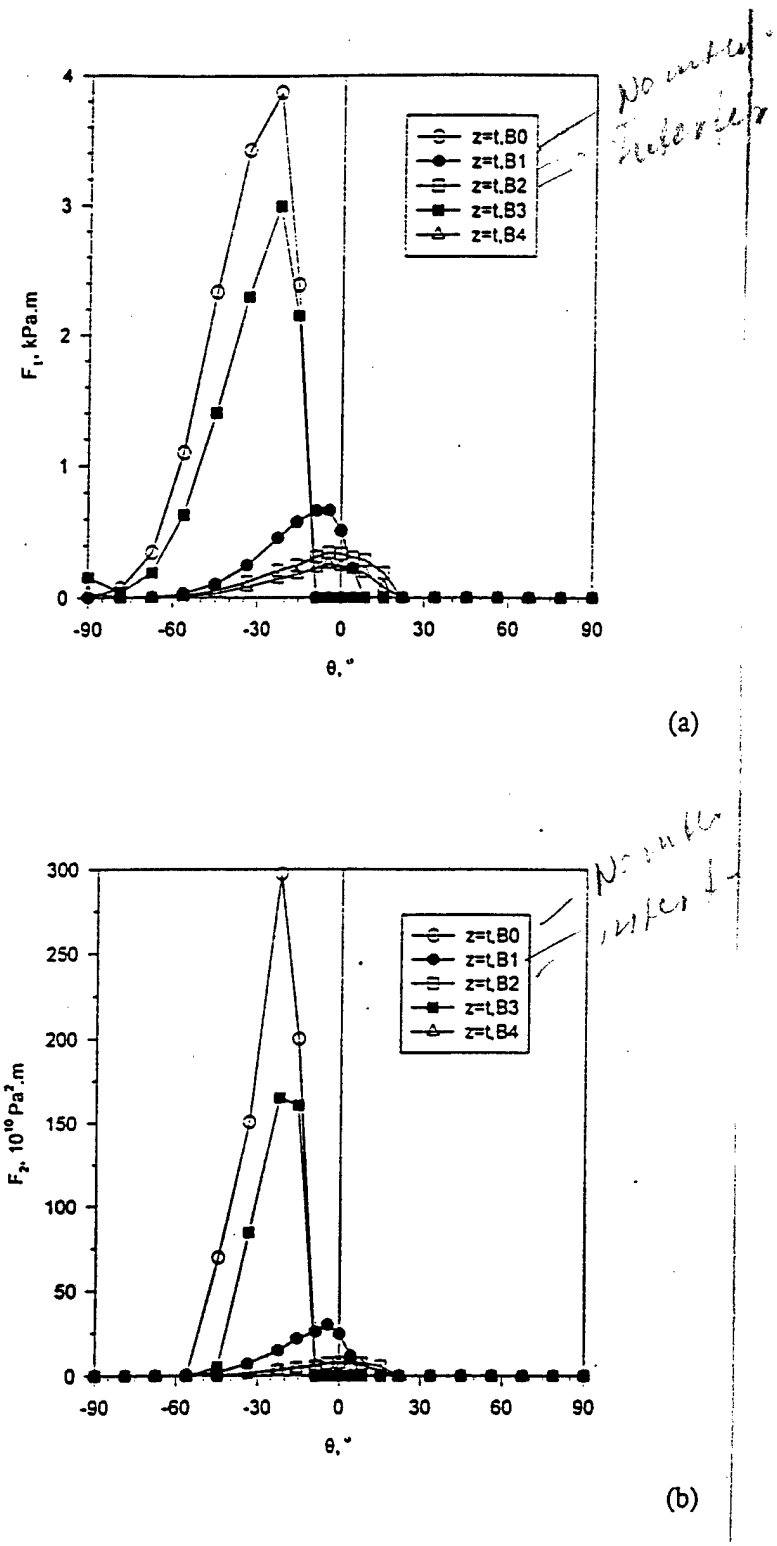

Figure 9. (a) Variation of the fretting wear parameter, F_1, with angular location at z=t, (b) Variation of the fretting fatigue parameter, F_2, depth at which both parameters peak.

APPENDIX C

A PIEZOELECTRIC-ACTUATED FRETTING WEAR MACHINE

by

M. Xue, J. Wert, P. Bastias, G. Hahn

Center for Materials Tribology

P. O. Box 1593, Station B

Vanderbilt University

Nashville, TN 37235

ABSTRACT This paper describes a novel, piezoelectric-driven fretting wear machine that can generate slip amplitudes from 1μm to 100 μm and frequencies from 0.05 Hz to 30 Hz with contact pressures up to 1 GPa. The closed-loop controlled piezoelectric actuator regulates the sum of the elastic distortion of the load train and the slip displacement of the interface. The machine facilitates the measurement of the coefficients of friction and the specific wear rates in both air and saline solution environments under constant total displacement and contact normal force. Some typical test results for aluminum alloys in contact with hardened steel are presented.

KEY WORDS: fretting wear, fretting corrosion, machine design, piezoelectric actuator, closed-loop control, aluminum, steel.

Introduction

Fretting wear and fretting corrosion are complex phenomena involving 2 contacting bodies experiencing small, cyclic, relative movement or slip under contact

pressure in a particular environment (Waterhouse, 1972, 1981, 1992). Three of the most important variables are the small slip amplitude, typically in the range of 1 μm to 100 μm, the contact pressure and the number of fretting cycles. The measurement of fretting wear damage and the study of the wear mechanisms call for a machine capable of applying a large number of contact cycles with different, well defined slip amplitudes and contact pressures to small laboratory samples and the appropriate counterface in a controlled environment. Early fretting machines derived the oscillatory movements from a motor-driven eccentric cam (Iwabuchi and Hori, 1988; Smallwood et al., 1988; Sato and Shima, 1988; Hamdy et al., 1981). These machines produced large slip amplitudes usually with low frequencies. One of the inherent problems with the mechanical-driven mechanism is the variability of the slip amplitude arising from the hub clearance typically of the order of 10 μm (Hamdy et al., 1981). More recently, Price and Taylor (1988) has used an electromagnetic device to vibrate the specimens at a frequency between 60 to 120 Hz with slip amplitudes more than 25 μm. Blanchard et al. (1991) employed a hydraulic-driven vibrator from a conventional fatigue machine to produce frequencies as low as 0.1 Hz, and slip amplitude of 30 μm or greater. These three driving mechanisms do not lead themselves to providing the combination of low frequency and low peak-to-peak slip amplitude encountered in many mechanical assemblies.

This paper describes a novel, piezoelectric-driven fretting wear machine that can generate slip amplitudes from 1μm to 100 μm and frequencies from 0.05 Hz to 30 Hz with contact pressures up to 1 GPa. The machine has been used successfully to reproduce the fretting conditions in airframe-type, riveted aluminum lap joints.

Machine Design

The fretting wear machine was designed to test samples of sheet materials in contact with either a spherical or cylindrical counterface. A photograph and schematic drawing of the machine are shown in Figures 1 and 2. The machine consists of a specimen holder for small, e.g., 20 mm by 40 mm blanks, cut from 2 mm- to 3 mm-thick sheet material. The holder is supported laterally by a leaf spring. Vertical oscillations are generated by a P-843.60, Physik Instrumente (PI) piezoelectric translator with internal strain gage sensor (SGS). The counterface, a small, e.g., 5 mm- to 40 mm-diameter sphere or a 5 to 10 mm-diameter cylinder, is clamped in a holder mounted on a 40 kg support riding on a Thompson Industries linear bearing. The contact force is generated by 2, dead weight, pulley-lever arrangements, one in front and the other in the rear, with a mechanical advantage of 9. The lever arrangement can be seen in Figure 1 but is omitted in Figure 2. A container (also not shown) was built to collect corrosive media used in fretting corrosion tests. The aqueous solution is supplied by a flask with an adjustable valve, which is able to supply from 1 to 10 drops/minute of the liquid. The overall dimensions of the machine, about 375 mm high with a 375 mm by 375 mm base, were selected to facilitate tests in vacuum under a bell jar.

Instrumentation and Calibration

Oscillating Movement System

The system uses piezoelectric actuating and controlling devices, which together provide constant cyclic displacement in the range of 0.2 μm to 120 μm with a precision of 0.2 % of the total nominal travel (Physik Instrumente, 1992). The piezoelectric system consists of two electronic devices: one piezoelectric (PZT) translator with a built-in strain gage sensor (SGS) and one piezoelectric controller. These two devices work in a closed-loop mode Expansion Control (EC) Mode, as shown in Figure 3. In the EC mode, the free end of the PZT displaces an amount, which is preset by the operator at the beginning of an experiment. The piezoelectric controller then regulates the expansion amplitude of the PZT consistent with the preset value using the feedback from the strain gauge sensor. While it is expected that the displacement would be affected by hysteresis, possible drift movement of the PZT and also by the changing frictional forces, these phenomenon are automatically compensated by the piezoelectric controller. The peak-to-peak displacement is simply the maximum expansion minus the minimum expansion. The actual slip amplitude of fretting at the interface, i.e., the relative movement of the contacting surfaces, is obtained by subtracting the elastic displacement from the total peak-to-peak displacement of the tangential force-displacement (F_t-D) loop. Figure 4 is a schematic drawing of the tangential force-displacement loop, where a, b and c are positive elastic displacement, frictional force and the slip amplitude, respectively. The ratio, a/b, defines the compliance of the system.

Friction Force Measurement

The fretting machine offers measurements of the coefficient of friction, $\mu = F_t/P$, where F_t, the tangential force, is generated by the PZT translator, and P, the normal force, is applied by the counterface through the dead weight, pulley-lever arrangement. While the tangential force can not be measured directly, it is closely related to the input voltage to the PZT when the unit operates under slip amplitude control (EC mode). Therefore, the larger the tangential force, the higher the voltage supplied to the PZT must be to maintain constant amplitude. The tangential force is obtained from the conversion of the input voltage signal into a force signal. Two steps are involved:

(1). The relation between force and input voltage has been calibrated.

(2). The input voltage, which reflects the changes in the force with variations in the friction coefficient, is recorded continuously through a DT data acquisition system.

A set of the state-of-art programs with DT-VEE® software was developed to collect and process tangential force and displacement data simultaneously and automatically. These data are then used to construct the fretting loops to distinguish three fretting wear patterns, as suggested by Vingsbo and Soderberg (1988), and Zhou and Vincent (1992). The value of F_t used here is the average of the two values at which the gross slip starts on the forward and reverse half of the cycle as defined by the tangential force-displacement (F_t-D) hysteresis loops.

Normal Force and Calibration

The dead weight-pulley-lever loading system was calibrated by applying known

weights and measuring the normal force generated on a Chatillon force gage normal to the mass. The calibration curve, shown in Figure 5, was linearly regressed as: $P = -9.53 + 93.86 \times W$, where P is the resulted normal force in N, W is the total weight in kg.

Machine Stiffness

A calibration procedure was carried out to determine the total compliance of the system without installing samples, the compliance is linearly regressed to be 0.276 μm/N ($r^2 = 0.999$), which contributes $40 \times 0.276 = 11.04$ μm to the total elastic displacement. The other sources of elastic displacement are the specimen, sample holder and the interface. Under the given calibration conditions the contributions from the above three are 0.2 μm, 3.4 μm and 4.1 μm, respectively. Therefore, the total accountable elastic deformation is 18.7 μm, which is about 93.0% of the elastic displacement (≈ 20.0 μm) obtained from the fretting loops.

Control of Slip Amplitude

Operation at constant total displacement does not produce constant slip amplitude fretting at the interfaces when the frictional force changes during the test. An increase in frictional force is accompanied by an increase in the elastic component of the displacement and a reduction of the slip component. To maintain constant slip amplitude at the interface, it is necessary to adjust the output voltage from the external signal generator either manually or automatically. Experience has shown that the slip amplitude is relatively constant for large total displacement conditions (e.g., ≥ 60 μm). In that case the elastic displacement is relatively small and the slip amplitude is insensitive to changes

in the friction coefficient.

Experimental Procedure

The nominal displacement, normal force and frequency are preset to the desired values before each test while the closed loop control ensures that the total displacement is constant during the test. The tangential force and displacement are intermittently recorded. The data acquisition takes place about every 30 minutes and each time it collects four cycles of data. The acquisition frequency is at least 100 times of the fretting frequency, and is sensitive enough to detect any variation in the recording signals.

Fretting studies have been conducted in this way on AA 7075-T6 and AA 2024-T6 aluminum alloys in received conditions, using 38.1 mm × 15.3 mm × 2.0 mm (or 3.0 mm for 2024-T3) parallelepiped samples. The detailed drawings of the specimen are shown in Figure 6. Three different counterfaces have been employed: 38.1 mm-diameter 52100 bearing steel ball, 6.36 mm and 19.05 mm-diameter aluminum cylinders. Tests are carried out in both dry air and a 3.5% sodium chloride solution. The normal force is usually fixed at 37.3 N, which yields a Hertzian pressure of 407.0 MPa. Before testing, the specimens are polished with a series of sandpaper and the final polishing direction is parallel to the fretting movement direction. Specimens are also cleaned with acetone after immersion for 2.5 hours ultrasonically agitated action before and after test. After each fretting test, a Taylor-Hobson Talysurf-10 profilometer is used to measure the wear scar parallel and normal to the fretting direction, the profile measurements are made through the center of the wear scar. These profiles are used to calculate the specific wear rates, W_s, which is defined as material loss per unit of applied normal force and per unit

of sliding distance, and the unit used is usually m^3/Nm.

$$W_s = V/(2 \cdot \delta \cdot N \cdot P) \quad (1)$$

where V is the wear volume, δ is the slip amplitude, N is the number of fretting cycles, and P is the applied normal force.

Scanning Electron Microscopy (SEM) and Optical Microscopy are also used to observe the fretting wear patterns and identify the wear mechanisms before and after ultrasonically removing the wear debris.

Experimental Results

Figure 7 shows typical tangential force, displacement and force-displacement hysteresis loop records for three successive fretting cycles with total displacement maintained at 80 μm. As the tangential force increases, the corresponding displacement, up to 10 μm, is accommodated by elastic distortions of the PZT-actuator, the specimen holder and the connections. The contacting surfaces begin to slip when the tangential force reaches about 15 N. Slip proceeds for 60 μm with little increase in frictional resistance, until the direction of displacement is reversed. The tangential force, 15 N, taken together with the applied normal force, 37.3 N, defines the coefficient of friction, in the case, $\mu = 0.402$.

Figure 8 describes the variation of coefficient of friction with number of fretting cycles for 7075-T6 sample at 40 μm slip amplitude in the saline solution. In this case, the coefficient of friction fluctuates and tends to decrease with increasing number of cycles.

The profile of the fretting wear scar of the sample described in Figure 8 after N = 40,000 cycles, is shown in Figure 9, and the corresponding SEM image is presented in

Figure 10. The maximum depth of the wear scar is 25 μm, which may result from combined wear modes, such as adhesion, corrosion and abrasion. The average specific wear rate after N = 40,000 cycles, defined by Equation 1, W_s, is 7.50×10^{-14} m^3/Nm. The diameter of the fretting scar increases gradually with wear and is 80% larger after N = 40,000 fretting cycles with a corresponding 69% reduction of the contact pressures since the normal force is held constant.

Conclusion

The design of a fretting wear and fretting corrosion machine equipped with a piezoelectric actuator has been described. The machine has following capabilities:

(1) The built-in closed-loop feedback control system offers constant nominal displacement during test, and the range is between 1 μm to 100 μm, which is independent of testing frequency, normal loading, temperature and environment. The minimum applicable frequency is about 0.05, and the maximum is estimated to be 30 Hz.

(2) The normal force is constant during the test and able to produce the required Hertzian peak pressures between 200 MPa to 1000 MPa.

(3) The slip amplitude and tangential force can be monitored and recorded simultaneously during the test by using a DT-VEE® data acquisition system.

(4) The contact area, usually having a diameter of about 500 μm, can be immersed into a salted solution to conduct environmental experiments.

(5) Coefficients of friction and the specific wear rates can be measured with the tribosystem and other complementary equipment.

Acknowledgments

This work was supported with a grant from the Air Force Office of Scientific Research (F49620-93-1-0488). The authors wish to thank Bill Gentry and James Hightower for their assistance in machining the machine parts.

References

Blanchard, P., Colombie, C., et al., "Material Effects in Fretting Wear: Application to Iron, Titanium, and Aluminum Alloys", Met. Trans. A, 22A (1991).

Hamdy, M. M., Overs, M. P. and Waterhouse, R. B., " A New High-Temperature Fretting Wear Test Rig", J. Phys. E: Sci. Instrum., Vol. 14, 1981.

Iwabuchi, A. and Hori, K., "Effects of Temperature and Ambient Pressure on Fretting Properties of Polyimide", Wear, 125 (1988).

PI (Physik Instrumente), Products for Micropositioning, Catalog US-Edition, 1992.

Price, S. and Taylor, D., E., "Fretting Corrosion of A High Strength Low Alloy Steel in Synthetic Seawater Environments", Wear, 125 (1988).

Sato, J. and Shima, M., "Effect of Lubricants on Fretting Wear of Steel", Wear, 125 (1988).

Smallwood, R., Pearson, D. R. and Brook, P. A., "The Influence of Dissolved Oxygen in Seawater on the Fretting Corrosion of Roping Steel", Wear, 125 (1988).

Vingsbo, O., Soderberg, S., "On Fretting Maps", Wear, 126 (1988).

Waterhouse, R. B., Fretting Corrosion, Pergamon Press, New York, 1972.

Waterhouse, R. B., Fretting Fatigue, Applied Science Publisher, UK, 1981.

Waterhouse, R. B., "Fretting Wear", Metals Handbook, ASM, Vol. 18, 1992.

Zhou, Z. R., and Vincent, L., "Cracking Behavior of Various Aluminum Alloys during Fretting Wear", Wear, 155 (1992).

LIST OF FIGURES

Figure 1 Overview of the fretting wear test machine.

Figure 2 Schematic diagram of the fretting wear machine.

Figure 3 Closed-loop control (EC mode) of the piezoelectric translator with strain gage sensors.

Figure 4 Schematic drawing of a tangential force-displacement (F_t-D) loop.

Figure 5 Calibration curve of the normal force.

Figure 6 Dimensions of flat aluminum specimen.

Figure 7 Records of tangential force (a), displacement (b), and tangential force-displacement (F_t-D) curves (c) for three successive fretting cycles. Testing conditions: 7075-T6 at 60 μm displacement, 37.3 N normal force, 1 Hz frequency and in dry air.

Figure 8 Plots of coefficient of friction against number of fretting cycles for 7075-T6 in 3.5% NaCl solution at 40 μm displacement, 37.3 N normal force and 1 Hz frequency.

Figure 9 Profiles of fretting wear scars of 7075-T6 specimen after N = 40,000 cycles in 3.5% NaCl solution. Total displacement is 40 μm and normal force is fixed at 37.3 N.

Figure 10 SEM image of the wear scar described in Figure 3.9, showing wear debris and corrosion products, as well as pits in the middle of the picture.

LIST OF FIGURES

Figure 1 Overview of the fretting wear test machine.

Figure 2 Schematic diagram of the fretting wear machine.

Figure 3 Closed-loop control (EC mode) of the piezoelectric translator with strain gage sensors.

Figure 4 Schematic drawing of a tangential force-displacement (F_t-D) loop.

Figure 5 Calibration curve of the normal force.

Figure 6 Dimensions of flat aluminum specimen.

Figure 7 Records of tangential force (a), displacement (b), and tangential force-displacement (F_t-D) curves (c) for three successive fretting cycles. Testing conditions: 7075-T6 at 60 μm displacement, 37.3 N normal force, 1 Hz frequency and in dry air.

Figure 8 Plots of coefficient of friction against number of fretting cycles for 7075-T6 in 3.5% NaCl solution at 40 μm displacement, 37.3 N normal force and 1 Hz frequency.

Figure 9 Profiles of fretting wear scars of 7075-T6 specimen after N = 40,000 cycles in 3.5% NaCl solution. Total displacement is 40 μm and normal force is fixed at 37.3 N.

Figure 10 SEM image of the wear scar described in Figure 3.9, showing wear debris and corrosion products, as well as pits in the middle of the picture.

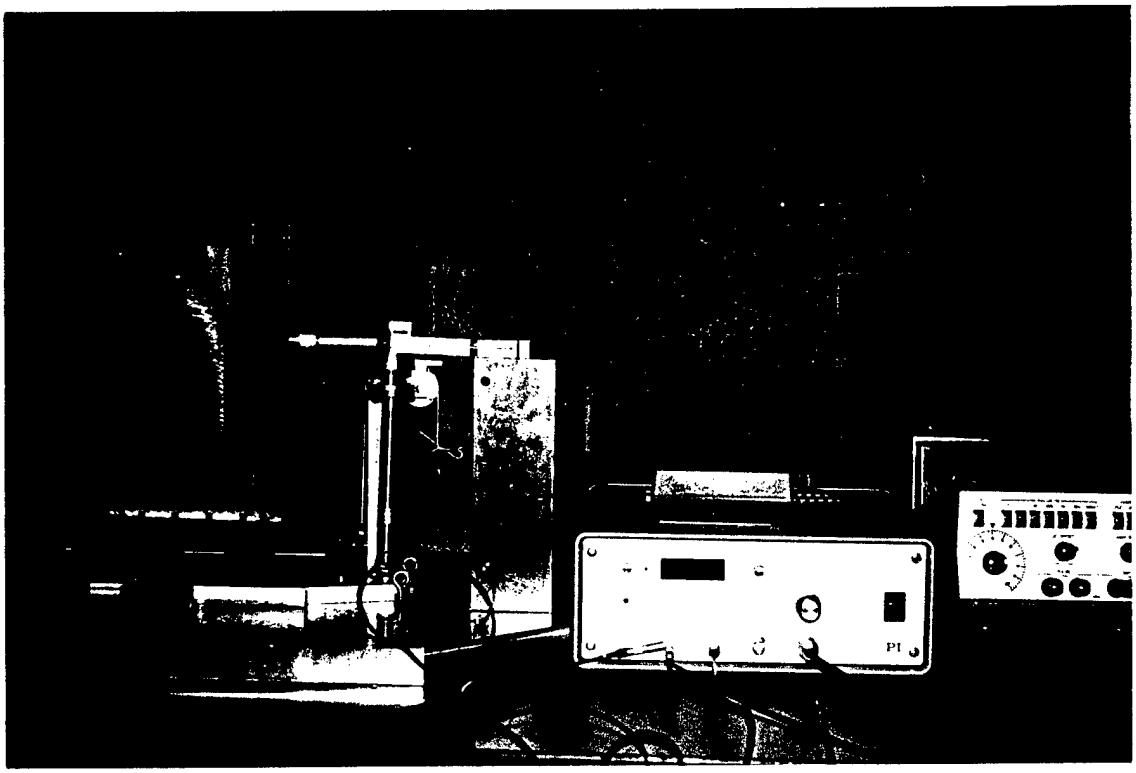

Figure 1 Overview of the fretting wear machine

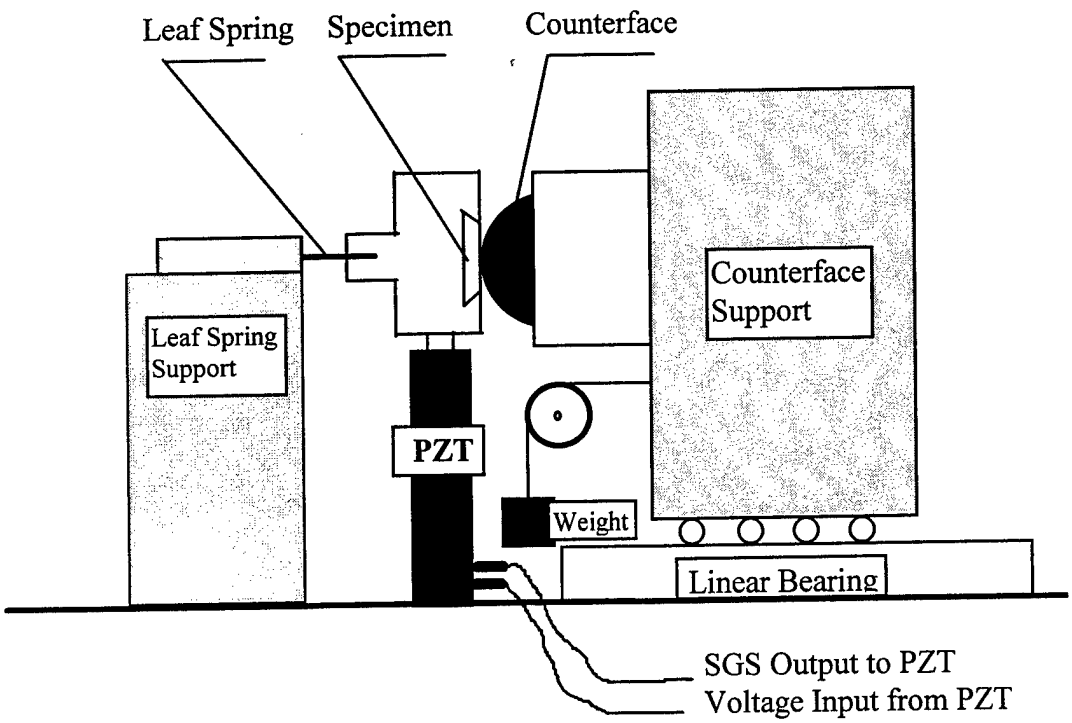

Figure 2 Schematic diagram of the fretting wear machine (mechanical part)

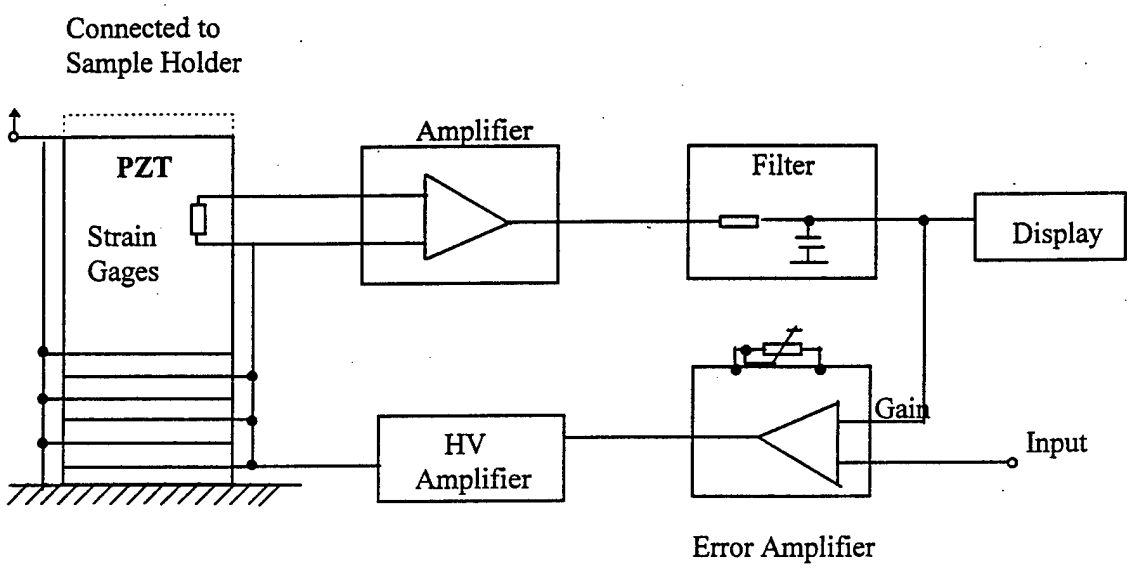

Figure 3 Closed-loop control (EC mode) of the piezoelectric tyranslator with strain gage sensors.

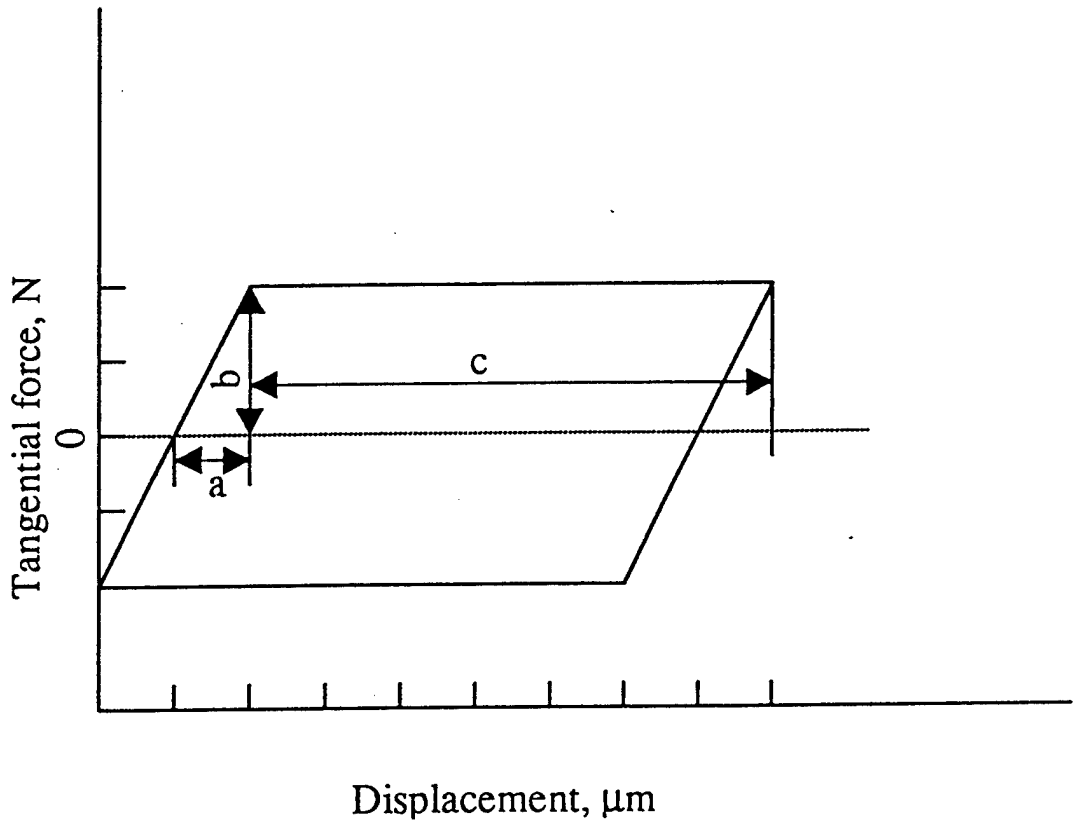

Figure 4 Schematic drawing of a typical tangential force-displacement (Ft-D) hysteresis loop. a/b defines the system compliance and c is the local slip amplitude.

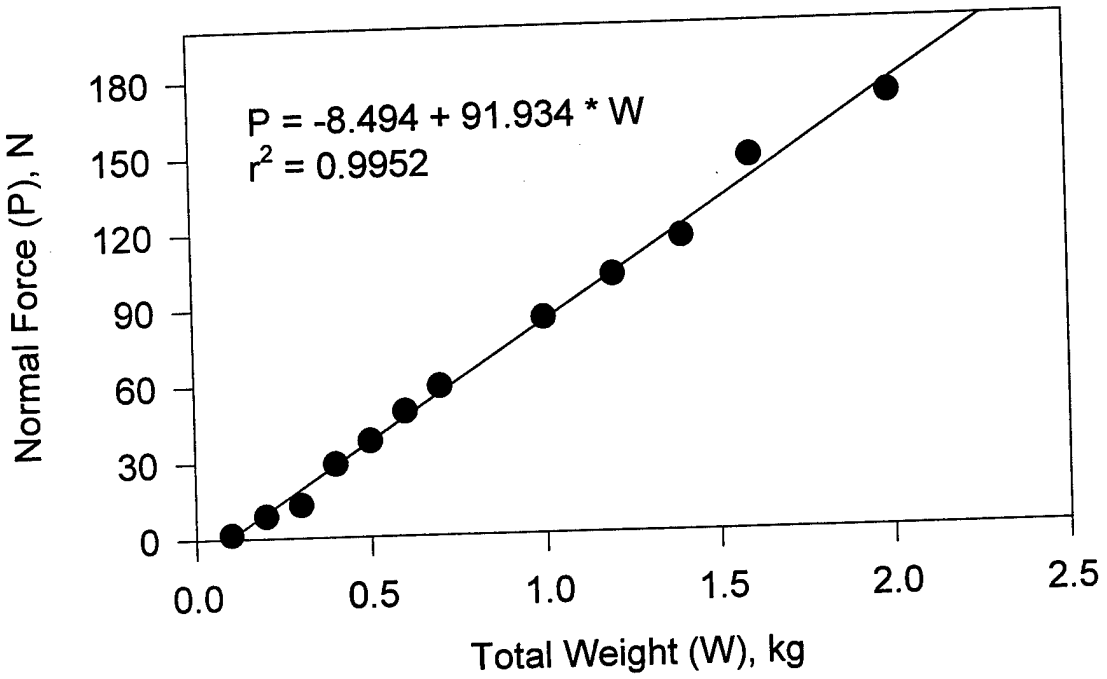

Figure 5 Calibration curve of the normal force.

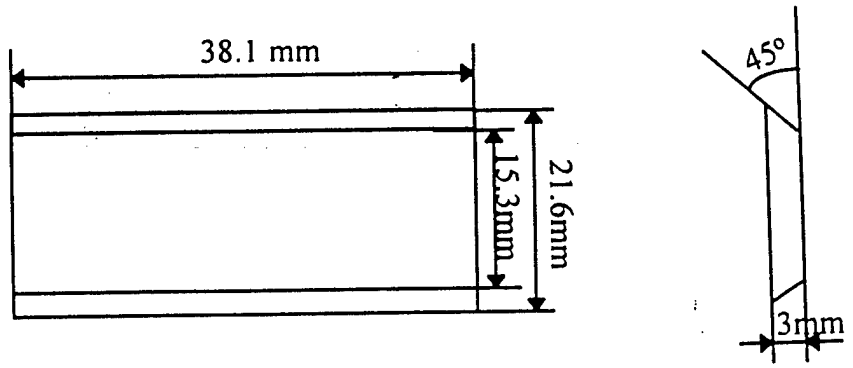

Figure 6 Aluminum specimen (flat) dimension

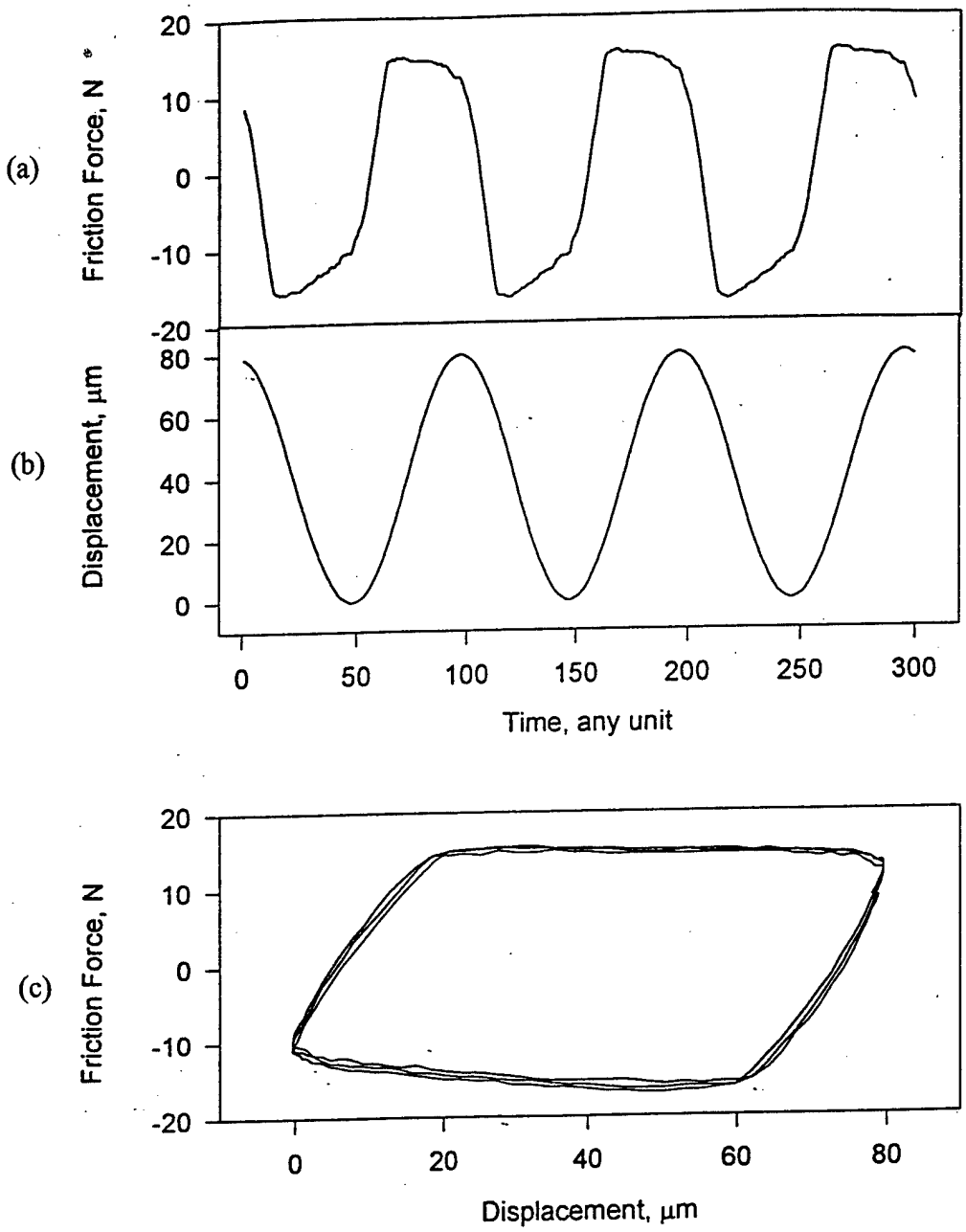

Figure 7 Records of tangential force (a), displacement (b) and tangential force-displacement (Ft-D) curves (c) for three successive fretting cycles. Testing conditions: 7075-T6 at 60 µm displacement, 37.3 N normal force and 1 Hz frequency in dry air.

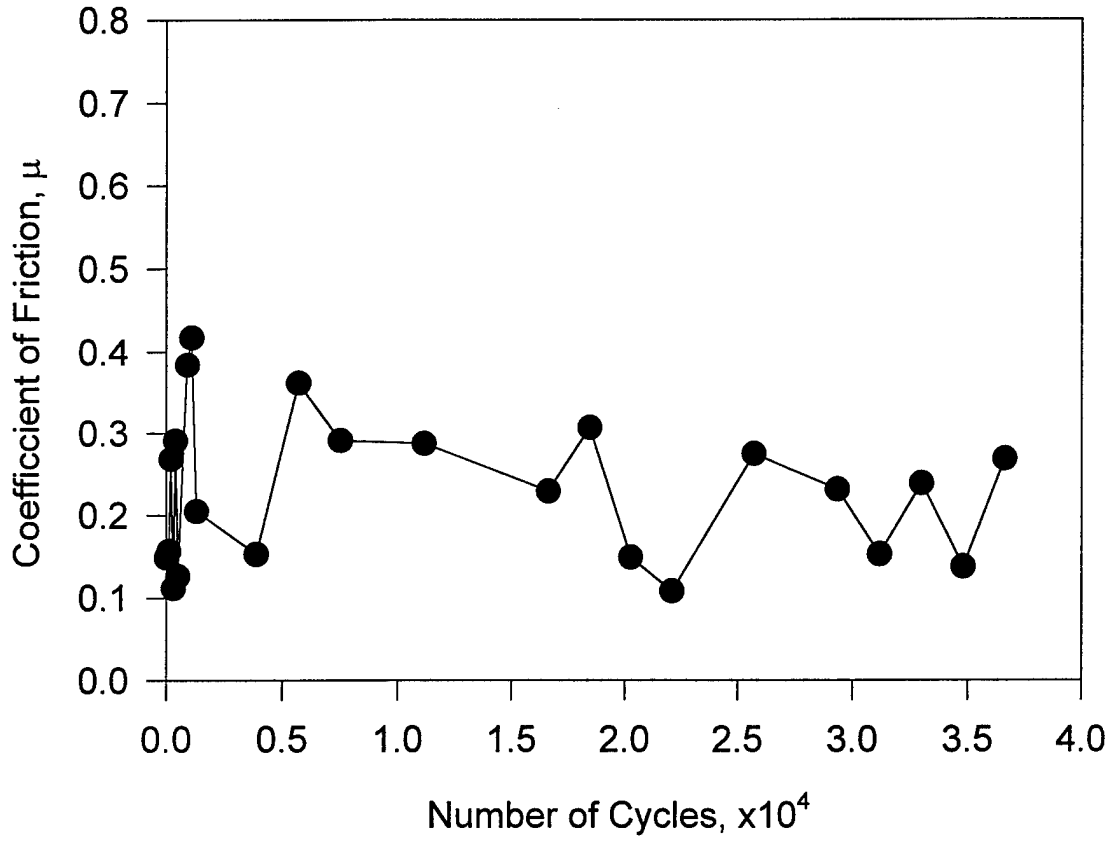

Figure 8 Plot of coefficient of friction against number of fretting cycles for 7075-T6 in 3.5% NaCl solution at 40 μm displacement, 37.3 N normal force and 1 Hz frequency.

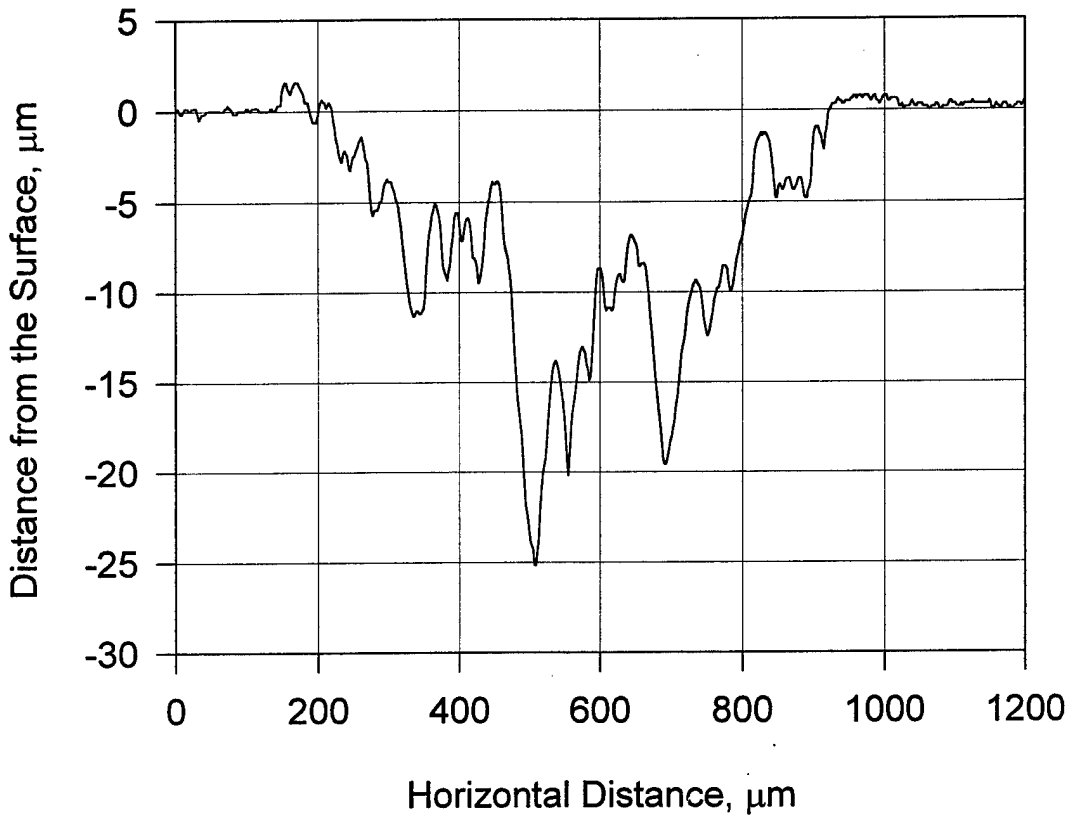

Figure 9 Profile of fretting wear scar of 7075-T6 specimen after N = 40,000 cycles in 3.5% NaCl solution. Total displacement is 40 µm and normal force is fixed at 37.3 N.

Figure 10 SEM image of the fretting wear scar described in Figure 3.9, showing wear debris and corrosion product, as well as pits in the middle of the picture. The fretting direction is vertical (↕).

APPENDIX D

FRETTING CORROSION OF 2024-T3 ALUMINUM ALLOY

by

M. Xue, J. Wert, P. Bastias, G. Hahn

Center for Materials Tribology

Vanderbilt University

Nashville, Tennessee 37235

ABSTRACT Fretting corrosion experiments of 2024-T3 were carried out with a unique fretting wear machine in both air and a saline solution. Fretting damage was significantly dependent on both slip amplitudes and environments. Severe fretting damage resulted from plastic deformation and adhesion for 25 μm and little damage was observed for 10 μm in air. Three different fretting regions were identified by tangential force-displacement loops under the given conditions in both environments. Specific wear rates were more than 10 times higher in 3.5% NaCl solutions than those in air due to the synergistic interaction between electrochemical corrosion and fretting wear.

KEYWORDS: fretting corrosion, fretting wear, coefficient of friction, specific wear rate, fretting regions, aluminum alloys, wear mechanisms.

Introduction

Fretting is the small-amplitude oscillatory movement that may occur between contacting surfaces, which are usually nominally at rest (Waterhouse, 1992). When

fretting occurs in a corrosive environment, namely fretting corrosion, the synergistic interaction between fretting and corrosion can enhance both mechanical and chemical damage to the contacting materials. Riveted and pinned connections in airframes are susceptible to fretting corrosion problems. As reported by Hoeppner et al. (1995), corrosion and/or fretting have been a contributing factor in at least 687 incidents and accidents on aircraft in the US since 1975. Corrosion produces exfoliation swelling at the rivet and often requires costly repair work. Fretting initiates fatigue cracks, produces wear debris and results in premature failure of riveted and pinned connections. A better understanding of fretting and fretting corrosion will support efforts to reduce damage and unplanned maintenance for corrosion and fretting, and facilitate the early detection of the damage.

Aluminum alloys are prone to fretting corrosion since the fretting wear disrupts the protective oxide film, and exposes nascent metallic surfaces to further corrosion. Hard oxide particles produced by the fretting corrosion assist the abrasion of the surfaces and produce more debris (Waterhouse, 1992; Hoeppner and Chandrasekaran, 1994). One of the immediate consequences of fretting corrosion of aluminum alloys is the production of black aluminum oxide debris containing about 23% metallic aluminum (Andrews et al., 1968). Particle sizes range from 1 μm down to less than 0.05 μm, depending on the degree of comminution. The coefficient of friction of aluminum reported by different researchers ranges from $\mu = 0.05$ to $\mu = 0.7$ (Waterhouse, 1972; Takehira, 1994), and depends on tribosystems. It shows a common trend. Halliday and Hirst (1956) observed that the friction coefficient, μ, increases in the first few cycles and falls to a much lower value, after several hundred cycles, at which value it remains relatively constant.

Waterhouse (1992) has summarized the material loss with a variety of contact geometries and methods. The specific wear rate ranges from, $W_s = 10^{-17}$ m^3/Nm to 10^{-13} m^3/Nm, and with a strong dependence on slip amplitude. Goto, Ashida and Endo (1987) have reported that for the fretting wear of an Al-Zn-Mg alloy in contact with itself the fretting wear rate in wet air was about 3.5 times higher than in dry air. Takehira (1994) has observed the specific wear rate in distilled and sea water were approximately 100 times the rate in air for all three aluminum alloys tested with a cylinder-cross-cylinder configuration. The maximum wear rate is close to 5.0×10^{-13} m^3/Nm. No information has been found from literature on the material loss attending the fretting contact of steel with aluminum.

The features of the damaged surfaces are influenced by the variables of the fretting process (Bill, 1982). The interpretation of fretting data has been a controversial due to the complex nature of fretting phenomenon, which involves as many as 52 parameters (Beard, 1982). In recent years, friction logs and fretting maps have been increasingly used to describe the process. Fretting wear damage has been identified as three damaging modes (Zhou and Vincent, 1992, 1995, 1997; Blanchard et al., 1995): (1) non-degradation (ND), (2) cracking and (3) particle detachment (PD), which correspond to three distinguishable tangential force-displacement loop shapes (F_t-D curves) and active slip conditions: quasi-closed (stick), elliptic (mixed stick-slip) and parallelepiped (full slip), respectively. Two distinguishable fretting maps, i.e., running condition fretting map (RCFM) and material response fretting map (MRFM) (Zhou and Vincent, 1992, 1993, 1995), have been proposed and constructed for three aluminum alloys by displaying the specific influence of individual fretting variables on the fretting wear behavior.

In the present paper, the fretting corrosion of 2024-T3 in contact with 52100 steel

in both ambient air and salted water was investigated using a piezoelectric-actuated, fretting wear machine. The influences of slip amplitude, number of cycles and environments on fretting corrosion were investigated. Friction loops were recorded during each experiment to describe the running condition and also determine the coefficient of friction. Profilometry was used to measure the fretting wear scars and hence to calculate the wear volume and specific wear rate. Both scanning electron microscopy (SEM) and optical microscopy were used to examine the worn surfaces. Energy Dispersive Spectrometry (EDS) was conducted to analyze the elements in the wear debris. The effect of fretting variables and the wear mechanisms are discussed.

Experimental Procedure

Fretting corrosion measurements were performed with a unique fretting wear machine which is more fully described in somewhere else (Xue, et al., to be published). Small, sheet coupons of the test material are mounted in a holder attached to a stack of piezoelectric crystals which serves as the actuator. In this way, small, and controlled displacements in the range $\delta_t = 1.0$ μm to range $\delta_t = 100.0$ μm relative to a fixed conterface can be produced with frequencies from 0.05 Hz to 30 Hz. A schematic of the machine is shown in Figure 3.2. The machine can accommodate corrosive media at the contacting interface. The conterface, a hardened sphere, is supported by a heavy mass riding on a linear bearing. The normal force between the sample and counterface is generated by 2 dead weights, acting through 2 sets of pulley and levers on the mass supporting the steel counterface. The contact force was calibrated by applying known weights, and measuring the normal force generated on a Chatillon force gage normal to

the mass. The displacement is regulated by the piezoelectric controller which compensates for hysteresis and drift. The friction force is deduced from the input voltage to the piezoelectric translator. Both the local slip amplitude and the coefficient of friction are deduced from the friction force-displacement hysteresis loops. A schematic drawing of the typical tangential force-displacement hysteresis loop is demonstrated in Figure 3.4, where a is the elastic displacement of the loading system, c is the slip amplitude at the contact, and (2a+c) is the total displacement (δ_t), a constant value during each fretting test. The ratio, a/b, defines the compliance of the system

Fretting wear and friction measurements were performed on 3.0 mm-thick AA 2024-T3 sheet in the as-received condition. The specimens, 38.1 mm × 17.0 mm rectangular blanks, were hand polished through 600 grit silicon carbide paper. The final polishing direction was parallel to the fretting direction. Specimens were rinsed with acetone in an ultrasonic cleaner before tests. The counterface used was a 38.1 mm-diameter, hardened 52100 ball with a hardness of HRC 62. All tests were conducted at room temperature and a frequency of 1.0 Hz, either under dry condition or with the contact region immersed in the 3.5% NaCl solution. For most tests, the normal force was fixed at P = 37.30 N which yields a peak pressure of 407.0 MPa at the center of a Hertzian, 420 μm-diameter contact patch. Tests were also conducted on three applied normal loads: P = 18.6 N, 37.3 N and 65.6 N, corresponding with Hertzian pressures: p_0 = 323 MPa, 407 MPa and 491 MPa, respectively. After each fretting test, a Talysurf profilometer was used to measure the wear scar parallel and normal to the fretting direction, the profile measurements were made through the center of the wear scar prior to cleaning and after immersion for about 2.5 hours ultrasonically agitated action. The

specific wear rate, W_s, is deduced from V, the volume of the wear scar revealed by the profilometer trace:

$$W_s = V / (2 \cdot \delta \cdot N \cdot P)$$

where δ is the average local slip amplitude, N is the number of cycles and P is the applied normal force.

Experimental Results

Tangential Force-Displacement Loops and Coefficient of Friction

Figure 1 shows the tangential force-displacement hysteresis loops for the fretting of 2024-T3 against steel with a Hertzian contact pressure p_0 = 407 MPa, frequency of 1.0 Hz in either air or 3.5% NaCl solution. For the total displacement of 10 μm [Figure 1(a)] in dry air, the friction is initially low, $\mu = 0.12$, then increases to about $\mu = 0.22$ for larger number of fretting cycles (see Figure 2). At higher friction level, the total displacement is accommodated either completely by elastic deformation (in the form of quasi-closed Ft-D loops, stick) or by both elastic deformation and small amount of slip (elliptic Ft-D loops, mixed stick-slip). In the latter case, the tangential force-displacement curves are elliptic with a slip amplitude of $\delta = 2.4$ μm. After about N = 20,000 fretting cycles, the steady-state loops are obtained and are elliptic. For the total displacement of 40 μm [Figure 1(c)], the friction is relatively low for the first few cycles, $\mu \approx 0.2$, and then increases to $\mu \approx 0.5$ for the next 12,800 cycles, leading to quasi-closed (stick) or marginally open, elliptic loops. Finally friction decreases, $\mu \approx 0.34$, and the stead-state loops are reached with the shape of parallelepiped (full slip) after about N = 38,000 fretting cycles. For a relative

large total displacement of 80 μm, slip amplitude $\delta \approx 60$ μm [Figure 1(d)], the friction is approximately constant, $\mu \approx 0.29$, during the test after momentarily high value, $\mu \approx 0.43$, though it decreases at the end of the test. The tangential force-displacement curves are always parallelepiped-like shapes throughout the test and the frictional force increases rapidly at two ends of the displacement. Under wet conditions, for the displacement of 10 μm, only elliptic tangential force-displacement curves are observed after the initial parallelepiped, as seen in Figure 1(b). No quasi-closed curves are observed compared to Figure 1(a) in air.

Coefficient of friction values deduced from above tangential force-displacement loops for different total displacements and in both dry and wet conditions are presented as a function of the number of fretting cycles in Figure 2. The coefficient of friction in dry air is generally higher than in NaCl solution at both low and high total displacements, but after N = 40,000 cycles all the coefficient of friction curves tend to approach to a similar value, around $\mu = 0.18$. For small total displacements the coefficient of friction shows a peak value following an initial low value, then decreases to a steady state value. Alternatively for large total displacements the friction coefficient curves shows more peaks. The steady-state values of the coefficient of friction are listed in Table 4.1 for fretting tests under three different levels of Hertzian contact pressures: $p_0 = 323$ MPa, 407 MPa and 491 MPa (with applied normal forces: P = 18.6 N, 37.3 N and 65.6N, respectively). Under mediate and high contact pressures, the steady-state coefficient of friction is close to a similar value, i.e., $\mu = 0.30$ in dry, and $\mu = 0.188$ in wet conditions. With lower contact pressure, the steady-state coefficient of friction is relatively high, and is close to, $\mu = 0.60$.

Specific Wear Rates

Measurements of wear scar and the specific wear rate are complicated by the build-up of wear debris. In some cases, the profile of the wear scar on the aluminum sample, immediately after testing, reflects a build-up of material and a volume increase arising from wear debris deposited on top of the wear scar. With ultrasonic cleaning, usually a wear scar in the form of a depression was usually uncovered in the surface, as shown in Figure 3. Energy Dispersive Spectrometry (EDS) indicates that the debris consists of both aluminum oxide and iron oxide. Micrographs and profiles of the wear

Table 4.1 Coefficient of friction of 2024-T3 in contact with steel under $\delta_t = 60$ μm and different normal force.

Normal Force	Coefficient of Friction	
(N)	In Air	In Saline Solution
18.6	0.565	0.598
37.3	0.308	0.194
65.6	0.295	0.181

scars are reproduced in Figure 4. It illustrates that the material loss is almost 10× higher in wet condition than in dry condition. Two sets of measured specific wear values are summarized in Figure 5: (1) 2024-T3 flat in contact with the steel sphere, (2) 2024-T3 flat in contact with 2024-T3 hemisphere. These results show that the specific wear rates are in the range: 10^{-15} $m^3/Nm < W_s < 10^{-13}$ m^3/Nm for dry contact, and 10^{-13} $m^3/Nm < W_s < 10^{-12}$ m^3/Nm for wet contact. The specific wear rate of 2024-T3 alloy in contact with steel is the highest observed.

Wear Scar Profiles

The effect of number of cycles on fretting wear process was investigated by carrying out two sets of experiments: one set was for total displacement of 10 μm with N = 500 cycles, 5000 cycles, 25,000 cycles and 50,000 cycles; the second set utilized a total displacement of 25 μm with the same series of cycles. Figure 6 shows profiles of wear scars on cleaned 2024-T3 samples and their corresponding steel counterfaces before cleaning at a total displacement of 10 μm. Depending on the number of cycles, some of the steel counterfaces did not show any surface damage other than little wear debris transferred from aluminum samples. On the other hand, the aluminum samples all experienced progressive surface damage that depends on the number of fretting cycles. After both 500 cycles and 5,000 cycles the sample surfaces were worn sufficiently to accommodate the surface shape of the much harder counterface and the roughness was reduced compared to the unfretted surfaces. After N = 50,000 cycles, the surface was further deformed and the damaged area was larger than that after 500 and 5,000 cycles. In Figure 7 the cleaned counterfaces are quite smooth and do not exhibit any remaining

transferred aluminum debris. For total displacement of 10 μm, the profiles of the worn aluminum samples after ultrasonic cleaning are very similar to the profiles of uncleaned specimens. This indicates that the fretting damage is minimal.

Figure 8 shows the profiles of the wear scars of aluminum samples and the corresponding steel counterfaces prior to cleaning under a 25 μm total displacement. After 500 and 5,000 cycles the counterfaces did not exhibit much surface damage except wear debris transferred from the aluminum samples. After 50,000 cycles, a large amount of material was transferred from the aluminum sample to the counterface. Conversely the aluminum samples exhibited progressive surface damage with increasing fretting cycles. Similar to previous observations for the total displacement of 10 μm after 500 cycles and 5,000 cycles, the surfaces of aluminum samples were deformed to accommodate the surface shapes of the harder counterfaces. The roughness was also reduced compared to the unfretted surface and the waviness was greatly increased. After 50,000 cycles, the aluminum surface was not only deformed plastically, but a large particle of the aluminum alloy was formed and removed. After ultrasonic cleaning, the aluminum sample shows an even larger materials loss and the steel counterface did not suffer any surface damage after 50,000 cycles, as shown in Figure 9.

Discussion

Coefficient of Friction

From Figures 2 and 3, it is seen that the friction for 2024-T3 in contact with steel is generally lower in saline solution than in air. This may be due to the lubrication effect of

water and softening effect (Gahr, 1987) of the corrosive media surrounding the contact area. Among four sets of tangential force-displacement curves, all hysteresis loops shows a short period of full slip at the beginning of each test with low friction, which can be attributed to the lubrication effect of preexisting oxide layer on the surfaces (Halliday and Hirst, 1956). For total displacement of 80 μm, the rapid increase of friction at two ends of the total displacement, as shown in Figure 1(d), is due to the ridges (Blanchard et al., 1995) formed plastically at the top and bottom of the wear scar, as illustrated in Figure 8(c).

As also shown in Figure 1, the form of friction coefficient curves is that usually found in fretting tests: an initially very low friction due to the oxide film in the first few cycles, which can be referred to the first hysteresis loop of each set of the tangential force-displacement curves in Figure 1, immediately a high friction is observed in the first few hundred cycles because the oxide film breaks down due to fretting disruption, and thus metal-to-metal contact area increases, resulting in high friction. This has been also confirmed by measuring the electric resistance of the fretting pair (Waterhouse, 1972). After the friction reaches maximum value, it decreases and fluctuates for some cycles and finally reaches the steady-state value. The reason is that the newly formed oxide film and the loose oxidized wear debris, i.e., so-called third bodies (Blanchard et al., 1995), accumulate between the contacting surfaces and accommodate the relative slip, which causes a decrease of friction. More peaks at high slip amplitude are attributed to the repeating re-adhesion of wear particles to the parent surface (Goto et al., 1987). This re-adhesion leads to the formation of a pile-up debris layer which acts as an obstruction during fretting motion so that the friction increases up to the second peak value. As the

obstacle breaks down, the friction decreases again to a steady state value.

Specific Wear Rates

The result for 2024-T3 against 2024-T3 is similar to the findings of Goto, Ashida and Endo (1987) for higher slip amplitudes, e.g., 50 μm to 100 μm which represent the total displacement rather than the local values of slip amplitudes. The values for contact with steel in the saline environment are 5× the highest values reported by Goto et al., (1987). Their results may be lower because they used the profile traces of wear scars without removing wear debris and the total displacement rather than the local slip amplitudes when calculating the specific wear rate.

Total Displacement and Fretting Wear Mechanisms

The number of fretting cycles have great effect on the wear process, and the wear mechanisms can be identified through analyzing the profiles and the wear scars. Figure 6 suggests the aluminum samples experienced progressive surface damage, but the counterfaces did not suffer any surface damage other than wear debris transferred from the aluminum samples. The accommodation of sample surfaces to the surface shape of the harder counterface indicates that abrasion (plowing) and possibly plastic deformation are two of the wear mechanisms for fretting under small total displacement. Figure 10 contains micrographs of the aluminum sample and the counterface before cleaning. It is obvious that two different areas are present on the aluminum surfaces; one is the sticking area (white and shining area) and the other the slip area (dark area). The sticking area consists of asperities that adhered to the steel and resulted in material transfer.

Micrographs of these sticking areas at higher magnifications are shown in Figure 11. It is believed these sticking areas are responsible for most of the fretting damage to the material surface.

For fretting wear with 25 μm total displacement, materials transfer occurred after about 50,000 fretting cycles, which is a typical adhesion wear, suggesting under the given conditions severe adhesion is the main mechanism, though localized plastic deformation also contributes to the reduction of roughness and increase of waviness of the surfaces. Figure 12 includes the micrographs of the aluminum samples and counterfaces prior to cleaning. It is seen that the micrographs of the contacting pair matched each other exactly. The sticking area (white area) and slip area (dark area) existed after both 500 and 5,000 cycles. The sticking area is almost continuous and the slip area is larger than that obtained for $\delta_t = 10$ μm fretting tests. After 50,000 cycles the sticking area disappears and the slip area accounts for the total nominal contact area. This indicates that so-called full slip has occurred. At this point the amount of oxide generated is tremendous and a compacted oxide bed is formed on the sample surface. Figure 13 shows micrographs of fretted areas at higher magnifications. It is again found that adhesion is a major contributor to the either stick-slip mode or gross slip mode. For the gross slip mode fatigue may be another mechanism involved in the fretting damage since microcracks are found on both aluminum sample and steel counterface, besides finite element analysis (Kragelski, 1988) has shown that the tangential force is cyclic during each cycle of fretting sliding. The debris transferred to the counterface contains a large amount of metallic aluminum. The fretting regime is changed from partial slip to gross slip. However, the steady-state fretting wear seemed to be the fretting wear between the worn aluminum sample and the broken

juncture. The counterface merely played the role as a holder of the juncture. Therefore, the specific wear rate is initially high, then decreased and finally reached at a relatively constant value, steady-state specific wear rate.

The main fretting damage can be attributed to adhesion wear which results in material transfer and initiates microcracks. From the profiles of the wear scars parallel to the fretting direction, it is obvious that large amount of plowing has occurred and changed the contact conditions. Surface cracks observed on both aluminum sample and the counterface in full slip mode indicates that fatigue or delamination may be another damage mechanism involved in the fretting wear process. Flake-like debris was observed in the SEM studies. The extremely fine wear debris shown in Figure 13 is proof of the existence of fatigue cracks since only the fretting wear of the two surfaces of cracks can result in such fine debris (Waterhouse, 1992). The general fretting process of tribosystem examined can be stated as: when two materials are brought together asperities on the weaker material deform plastically and elastically first to accommodate the harder counterface. The fretting motion causes the deformed asperities to suffer further plastic deformation or fatigue. The debris, resulting from the breakdown of preexisting oxide layer and adhesive junctures and also delamination of surface layers, fills in the gaps between the strip-shaped asperities and the surface roughness decreases. The plastic deformation of the surface material leads to the increase of contact area. The increasing contact area increases the possibility of juncture formation and growth. However, cyclic displacement may rupture the junctures by either overloading or fatigue mechanism, and result in material transfer. This material transfer may introduce surface or subsurface microcracks. The formation of surface and subsurface microcracks enhances the possibility

of delamination and fatigue. It has also proven that abrasion plays a role in the fretting wear processes under the given conditions in this paper.

Conclusion

(1) Three fretting running conditions exist in the fretting wear and fretting corrosion of 2024-T3 aluminum alloy. In gross slip condition, severe adhesion and metal transfer occur in the given tribosystem.

(2) Curves of coefficient of friction have one peak for low slip amplitudes and more peaks for high slip amplitudes. Coefficient of friction is significantly dependent on slip amplitude and applied normal force.

(3) Specific wear rates are nearly 10 times higher in NaCl solution than in dry air due to the synergistic interaction of fretting and corrosion.

(4) Plastic deformation, adhesion and fatigue are the main damage mechanisms involved in the fretting corrosion of 2024-T3 in contact with 52100 steel.

Acknowledgment

The authors wish to thank Bill Gentry and James Hightower for their assistance in the construction of the fretting wear machine. Dr. Sandeep ??? is appreciated for his EDS work. This work was supported with a grant from the Air Force Office of Scientific Research (F49620-93-1-0488).

References

AGARD Corrosion Handbook, Vol 1, Aircraft Corrosion: Causes and Case Histories, ed.

by Wallace, W., Hoeppner, D. and Kandachar, P., Specialized Printing Services Ltd., 1985.

Bill, R. C., Review of Factors That Influence Fretting Wear. In Material Evaluation under Fretting Conditions, ASTM STP 780, Philadelphia, 1982, 165-182.

Blanchard, P., Colombie, C., Pellerin, V., Fayeulle, S., Vincent, L., "Material Effects in Fretting Wear: Application to Iron, Titanium and Aluminum Alloys", Metall. Trans. A, Vol. 22A, July 1995, p1535-1547.

Gahr, K-H. Z., Microstructure and Wear of Materials, Elsevier, 1987.

Halliday, T. S., and Hirst, W., "The Fretting Corrosion of Mild Steel", Proc. R. Soc. London, Ser. A, 236 (1956) 411.

Hoeppner, D. W., and Chandrasekaran, V., "Fretting in Orthopedic Implants: A Review", Wear 173 (1994) 189-197.

Hoeppner, D. W., Grimes, A., Hoeppner, A., Ledesma, J., Mills, T. and Shah, A., "Corrosion and Fretting as Critical Aviation Safety Issues", 18th ICAF Symposium, Melbourne, Australia, May 1-5, 1995.

Goto, H., Ashida, M., Endo, K., "The Influence of Oxygen and Water Vapor on the Friction and Wear of An Aluminum Alloy under Fretting Conditions", Wear, Vol. 116, 1987, pp. 141-155.

Takehira, A., "Fretting Wear of An Aluminum and Two Kinds of its Alloys in Marine Environment", Proc. JSME A, Vol. 65, No. 572, April 1994.

Waterhouse, R. B., Fretting Corrosion, Pergaman Press, 1972.

Waterhouse, R. B., "Fretting Wear", ASM Metals Handbook, Vol. 18 (1992) 242-256, ASM International.

Xue, M., Wert, J., Bastias, P., and Hahn, G., "A Piezoelectric-Actuated Fretting Wear Machine", to be published.

Zhou, Z. R., Fayeulle, S., Vincent, L., "Cracking Behavior of Various Aluminum Alloys during Fretting Wear", Wear 155 (1992) 317-330.

Zhou, Z. R., Vincent, L., "Mixed Fretting Regime", Wear 181-183(1995)531-536.

Zhou, Z. R., Vincent, L., "Cracking Induced by Fretting of Aluminum Alloys", Journal of Tribology, Vol. 119, 1997.

LIST OF FIGURES

Figure 1 Schematic diagram of the fretting wear machine.

Figure 2 Schematic drawing of a tangential force-displacement (F_t-D) loop.

Figure 3 Evolution of friction logs with number of fretting cycles for 2024-T3 vs. steel ball with f = 1.0 Hz under p_0 = 407 MPa for various displacement: (a) δ_t = 10 μm in lab air, (b) δ_t = 10 μm in the saline solution, (c) δ_t = 40 μm in lab air, and (d) δ_t = 80 μm in the saline solution.

Figure 4 Typical friction coefficient curves as the function of number of fretting cycles for 2024-T3 fretting against a steel ball in both dry and wet conditions.

Figure 5 Profilometer measurements of the wear scars produced by N = 10^4 fretting cycles for a 2024-T3 sample against a steel ball in ambient air with p_0 = 407 MPa.

Figure 6 Examples of wear scars and profilometer traces obtained after N = 5×10^4 fretting cycles for p_0 = 407 MPa, δ_t = 25 μm and f =1.0 Hz for 2024-T3 against a 52100 steel sphere: (a) dry air, $W_s = 8.5 \times 10^{-15}$ m^3/Nm, and (b) saline solution, $W_s = 90 \times 10^{-15}$ m^3/Nm .

Figure 7 Variation of the specific wear rate, W_s, with slip amplitude for 2024-T3 against a 52100 sphere in air and in a 3.5% salted water for N = 1×10^4 fretting cycles for p_0 = 407 MPa and f =1.0 Hz.

Figure 8 Profilometer traces of the aluminum sample and steel ball prior to cleaning, after (a) 500 fretting cycles, (b) 50,000 cycles for p_0 = 407 MPa and δ_t = 10 μm.

Figure 9 Profilometer traces of the aluminum sample and steel ball after cleaning, after (a) 500 fretting cycles, (b) 50,000 cycles, 20K×, for p_0 = 407 MPa and δ_t = 10 μm.

Figure 10 Profilometer traces of 2024-T3 sample and steel ball prior to cleaning, after (a) 500 fretting cycles, 10K×, (b) 50,000 cycles, 2K×, for p_0 = 407 MPa and δ_t = 25 μm.

Figure 11 Profilometer traces of 2024-T3 sample and steel ball after cleaning, after (a) 5,000 fretting cycles, 10K×, (b) 50,000 cycles, 2K×, for p_0 = 407 MPa and δ_t = 25 μm.

Figure 12 SEM and optical images of (a) 2024-T3 and (b) counterface for 5,000 cycles with a frequency of 1 Hz under p_0 = 407 MPa for δ_t = 10 μm.

Figure 13 SEM image of high magnification for broke joints, showing severe adhesion-related damage.

Figure 14 SEM and optical images of 2024-T3 and (b) the counterface after 5,000 cycles, (b) 50,000cycles with a frequency of 1 Hz under p_0 = 407 MPa for δ_t = 25 μm.

Figure 15 Highly magnified SEM and optical images of (a) 2024-T3 and (b) the counterface for 50,000 cycles with a frequency of 1 Hz under p_0 = 407 MPa for δ_t = 25 μm, showing fatigue cracks.

LIST OF FIGURES

Figure 1 Schematic diagram of the fretting wear machine.

Figure 2 Schematic drawing of a tangential force-displacement (F_t-D) loop.

Figure 3 Evolution of friction logs with number of fretting cycles for 2024-T3 vs. steel ball with f = 1.0 Hz under p_0 = 407 MPa for various displacement: (a) δ_t = 10 μm in lab air, (b) δ_t = 10 μm in the saline solution, (c) δ_t = 40 μm in lab air, and (d) δ_t = 80 μm in the saline solution.

Figure 4 Typical friction coefficient curves as the function of number of fretting cycles for 2024-T3 fretting against a steel ball in both dry and wet conditions.

Figure 5 Profilometer measurements of the wear scars produced by N = 10^4 fretting cycles for a 2024-T3 sample against a steel ball in ambient air with p_0 = 407 MPa.

Figure 6 Examples of wear scars and profilometer traces obtained after N = 5×10^4 fretting cycles for p_0 = 407 MPa, δ_t = 25 μm and f =1.0 Hz for 2024-T3 against a 52100 steel sphere: (a) dry air, $W_s = 8.5 \times 10^{-15}$ m^3/Nm, and (b) saline solution, $W_s = 90 \times 10^{-15}$ m^3/Nm .

Figure 7 Variation of the specific wear rate, W_s, with slip amplitude for 2024-T3 against a 52100 sphere in air and in a 3.5% salted water for N = 1×10^4 fretting cycles for p_0 = 407 MPa and f =1.0 Hz.

Figure 8 Profilometer traces of the aluminum sample and steel ball prior to cleaning, after (a) 500 fretting cycles, (b) 50,000 cycles for p_0 = 407 MPa and δ_t = 10 μm.

Figure 9 Profilometer traces of the aluminum sample and steel ball after cleaning, after (a) 500 fretting cycles, (b) 50,000 cycles, 20K×, for p_0 = 407 MPa and δ_t = 10 μm.

Figure 10 Profilometer traces of 2024-T3 sample and steel ball prior to cleaning, after (a) 500 fretting cycles, 10K×, (b) 50,000 cycles, 2K×, for p_0 = 407 MPa and δ_t = 25 μm.

Figure 11 Profilometer traces of 2024-T3 sample and steel ball after cleaning, after (a) 5,000 fretting cycles, 10K×, (b) 50,000 cycles, 2K×, for p_0 = 407 MPa and δ_t = 25 μm.

Figure 12 SEM and optical images of (a) 2024-T3 and (b) counterface for 5,000 cycles with a frequency of 1 Hz under p_0 = 407 MPa for δ_t = 10 μm.

Figure 13 SEM image of high magnification for broke joints, showing severe adhesion-related damage.

Figure 14 SEM and optical images of 2024-T3 and (b) the counterface after 5,000 cycles, (b) 50,000cycles with a frequency of 1 Hz under p_0 = 407 MPa for δ_t = 25 μm.

Figure 15 Highly magnified SEM and optical images of (a) 2024-T3 and (b) the counterface for 50,000 cycles with a frequency of 1 Hz under p_0 = 407 MPa for δ_t = 25 μm, showing fatigue cracks.

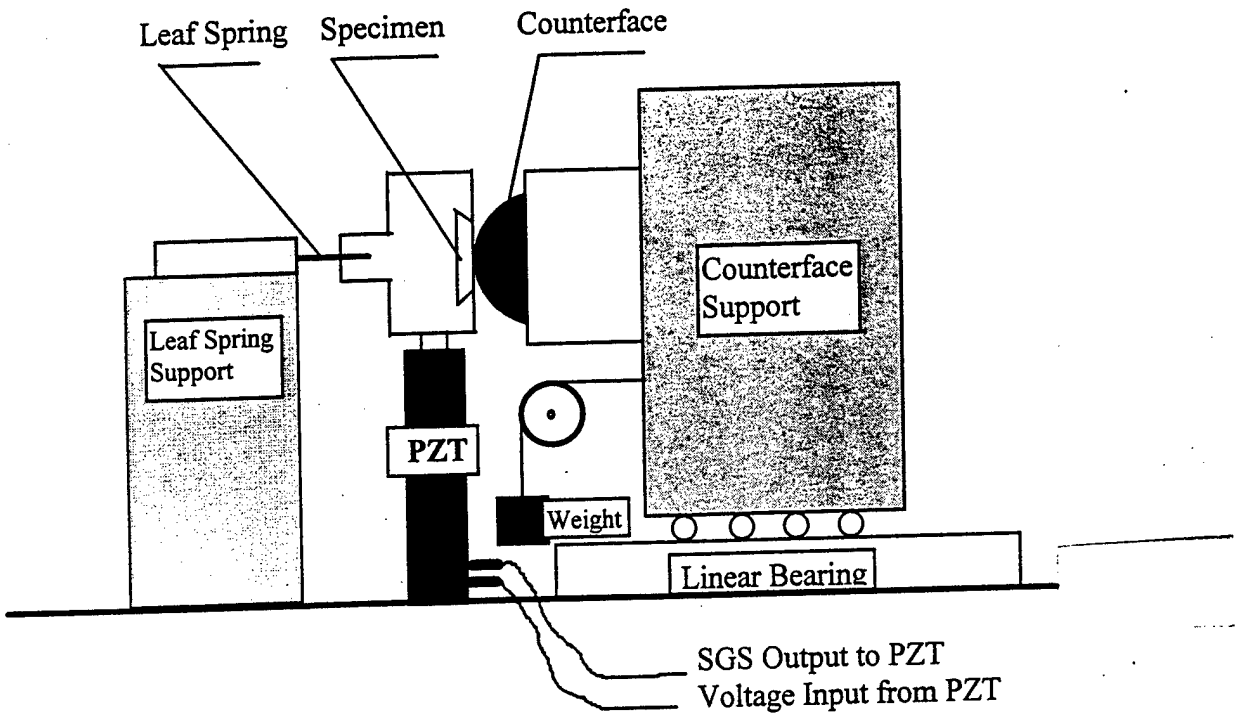

Figure 1 Schematic diagram of the fretting wear machine (mechanical part)

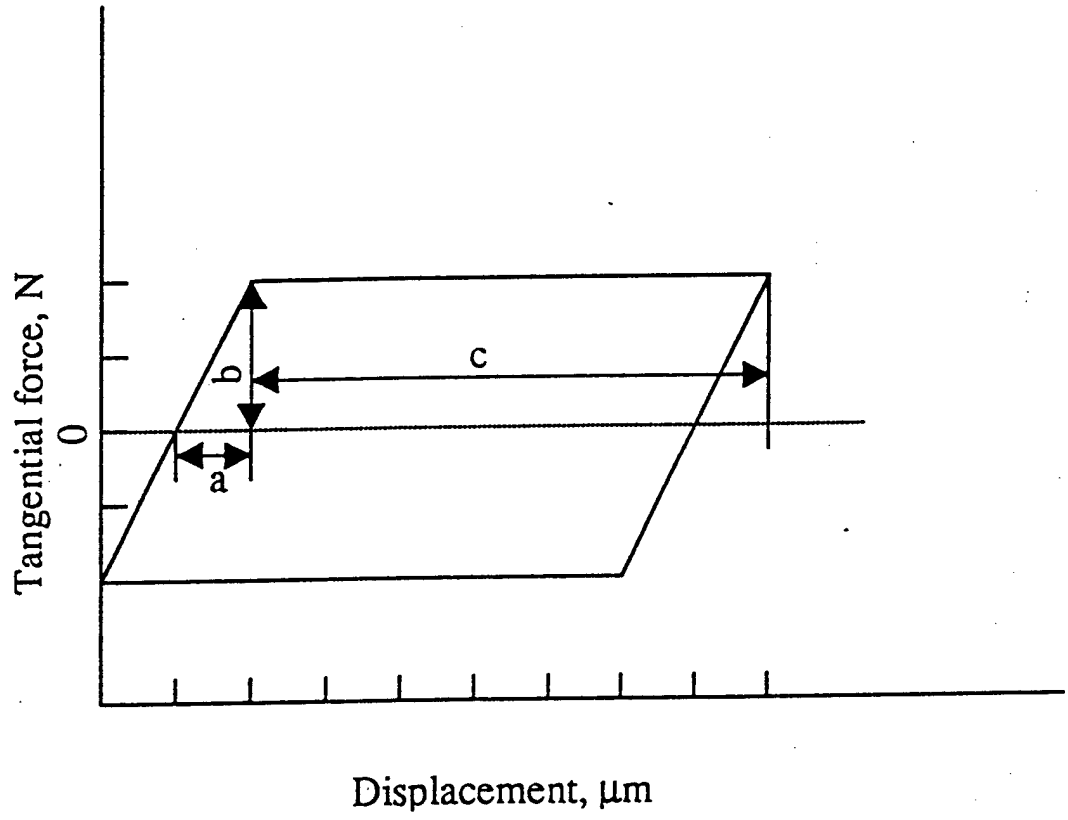

Figure 2 : Schematic drawing of a typical tangential force-displacement (Ft-D) hysteresis loop. a/b defines the system compliance and c is the local slip amplitude.

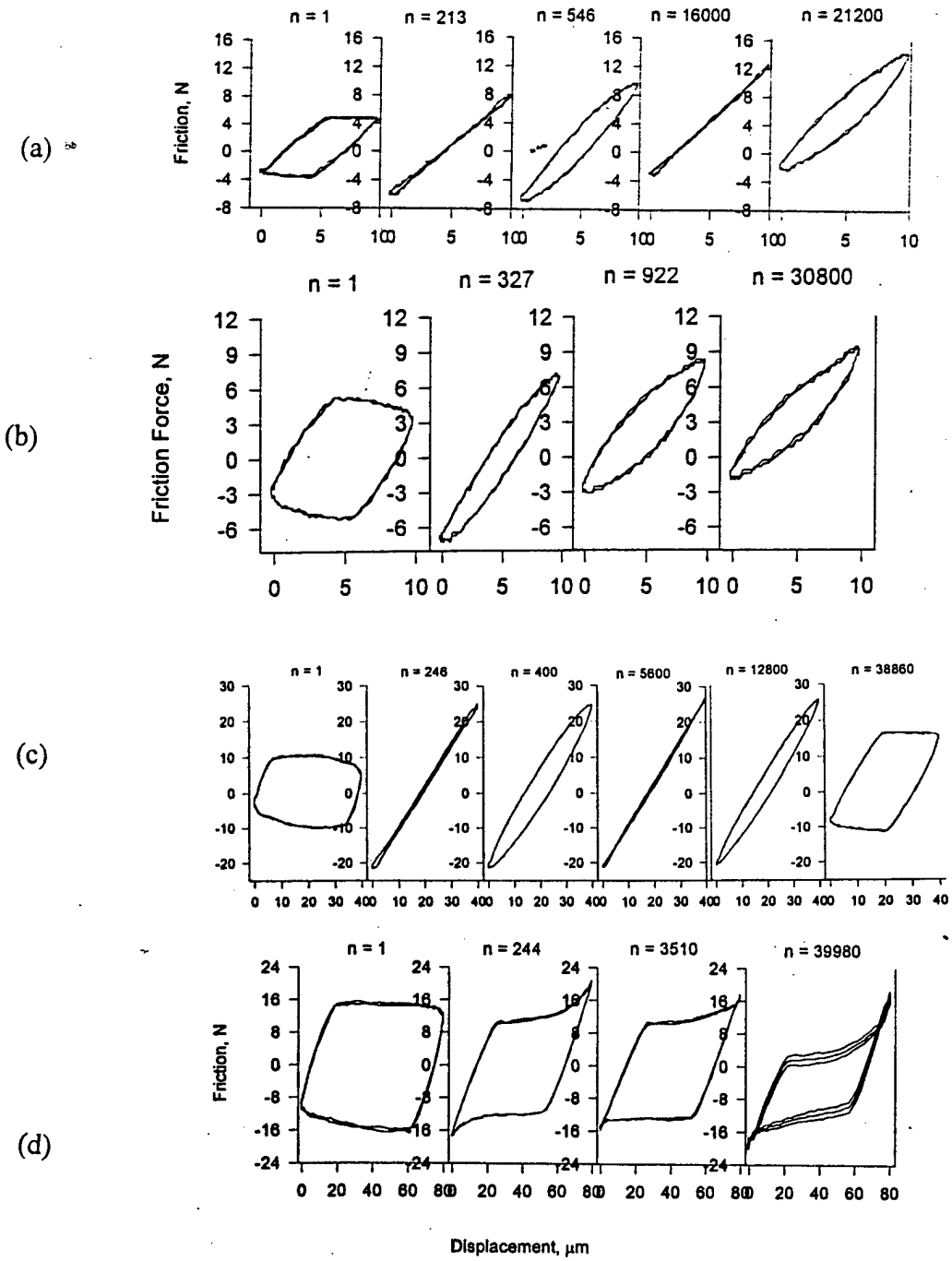

Figure 3 Evolution of friction logs with number of fretting cycles for 2024-T3 vs. steel with f = 1.0 Hz under p_0 = 407 MPa for various displacement: (a) δ_t = 10 μm in ambient air, (b) δ_t = 10 μm in saline solution, (c) δ_t = 40 μm in ambient air, and (d) δ_t = 80 μm in saline solution.

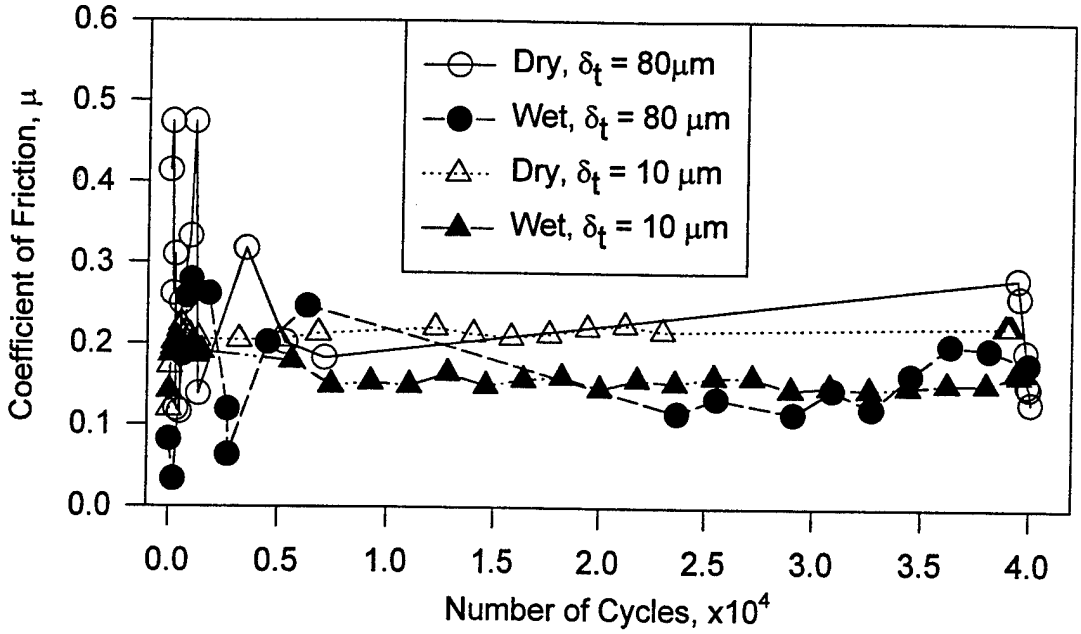

Figure 4 Typical friction coefficient curves as the function of number of fretting cycles for 2024-T3 fretting against a 52100 steel ball in both dry and wet conditions.

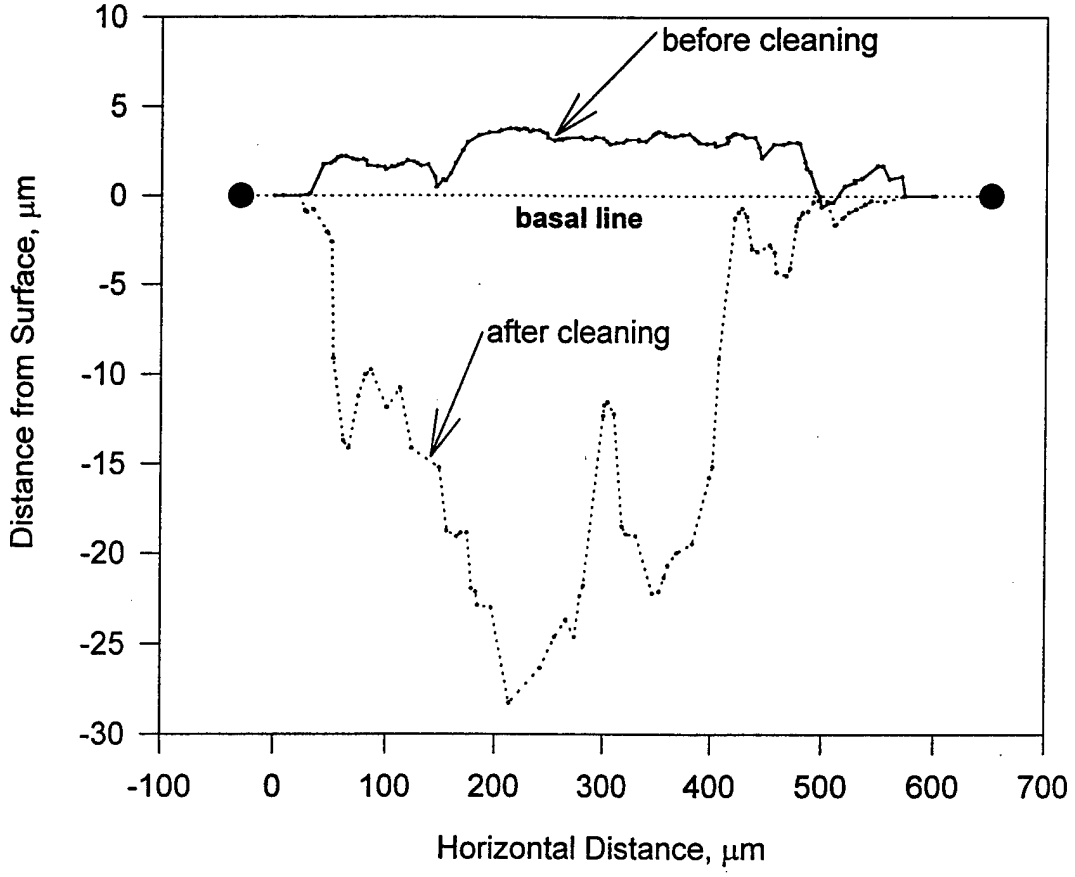

Figure 5 Profilometer measurements of the wear scars produced by $N = 10^4$ fretting cycles for a 2024-T3 sample against a steel ball in ambient air for a contact pressure p_0 = 407 MPa. Fretting produces a build-up of debris. Removal of the debris by washing reveals a 25 μm-deep wear scar.

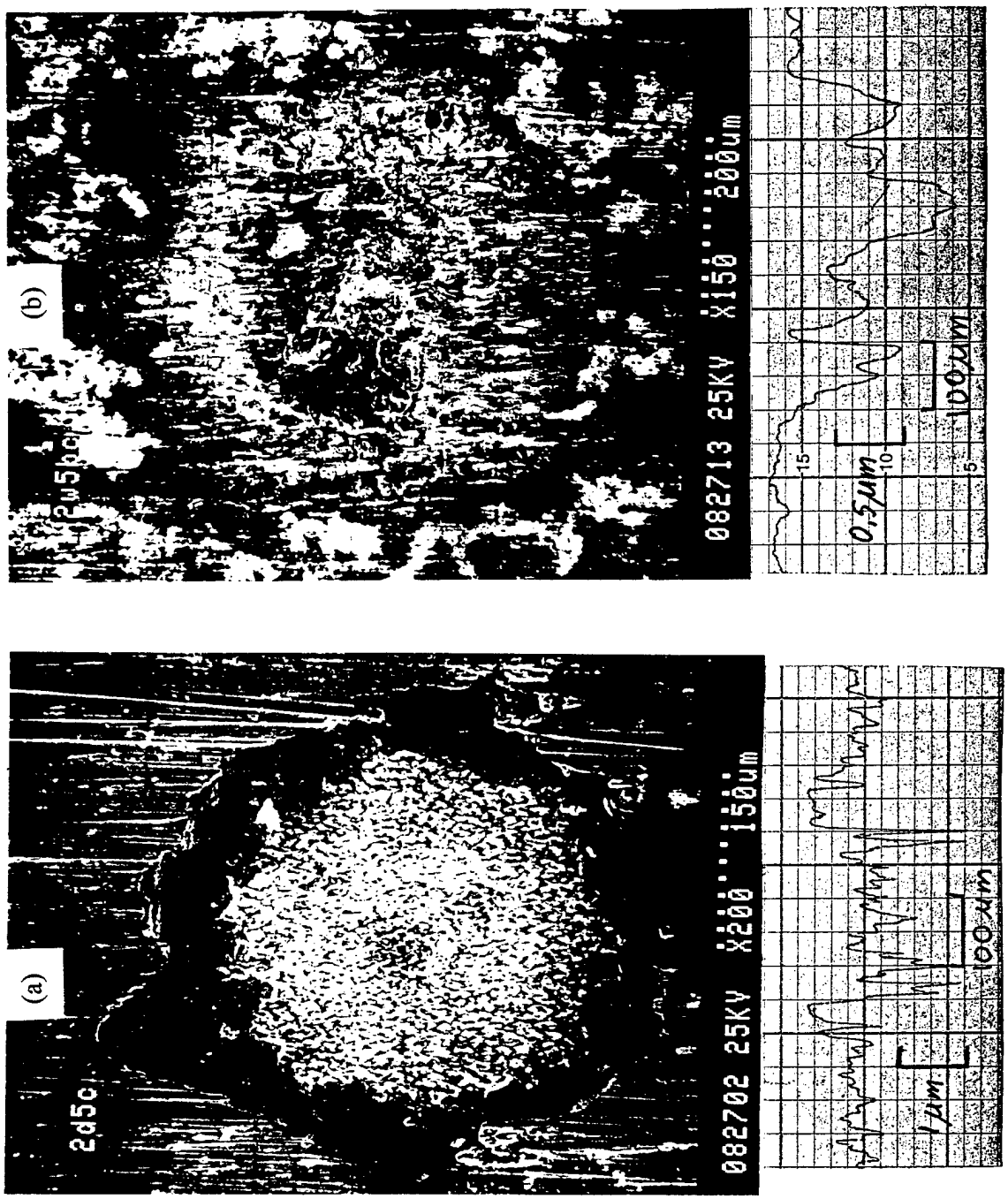

Figure 6 Examples of wear scars and profilometer traces obtained after $N = 1\times10^4$ fretting cycles for $p_0 = 407$ MPa, $\delta_t = 25$ µm and $f = 1.0$ Hz for 2024-T3 against steel: (a) in air, $W_s = 8.5\times10^{-15}$ m^3/Nm, and (b) in saline solution, $W_s = 90\times10^{-15}$ m^3/Nm.

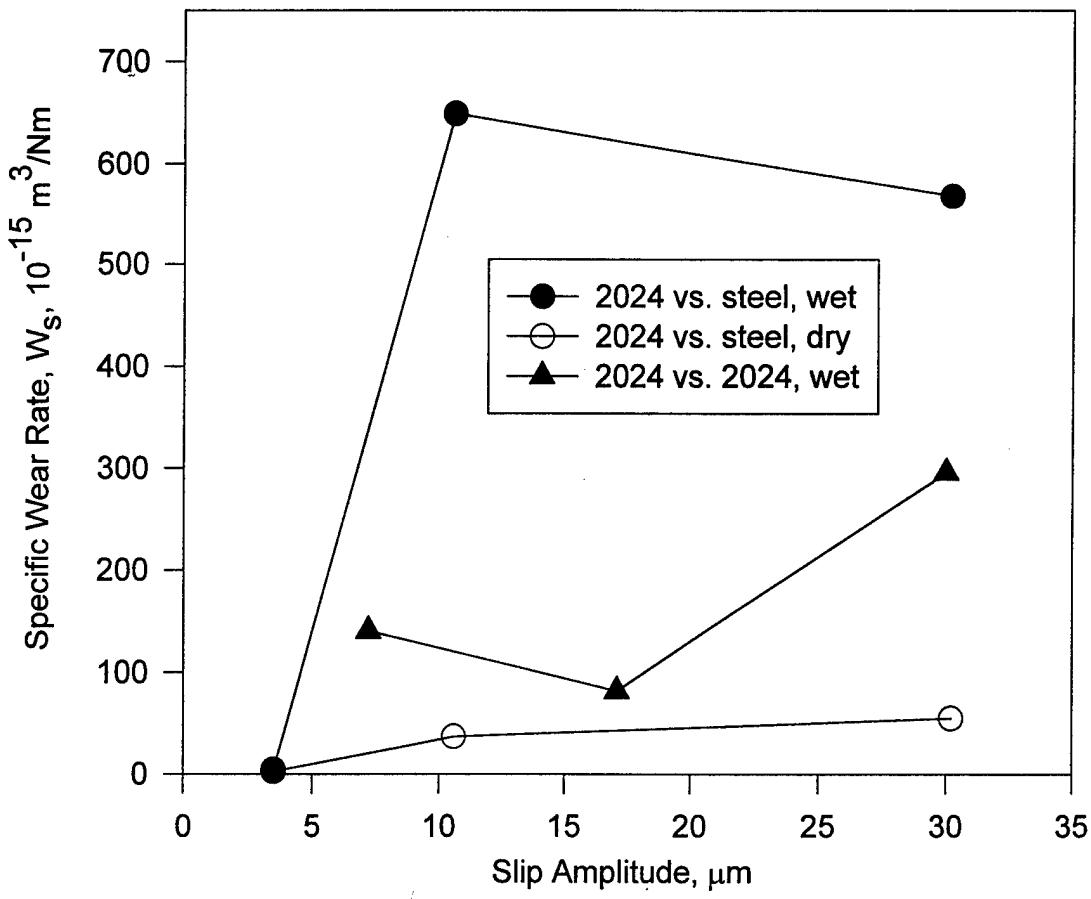

Figure 7 Variation of the specific wear rate, W_s, with slip amplitude for 2024-T3 against a 52100 sphere or 2024-T3 hemisphere in air and in a 3.5% NaCl solution after N = 1×10^4 fretting cycles for p_0 = 407 MPa and f =1.0 Hz.

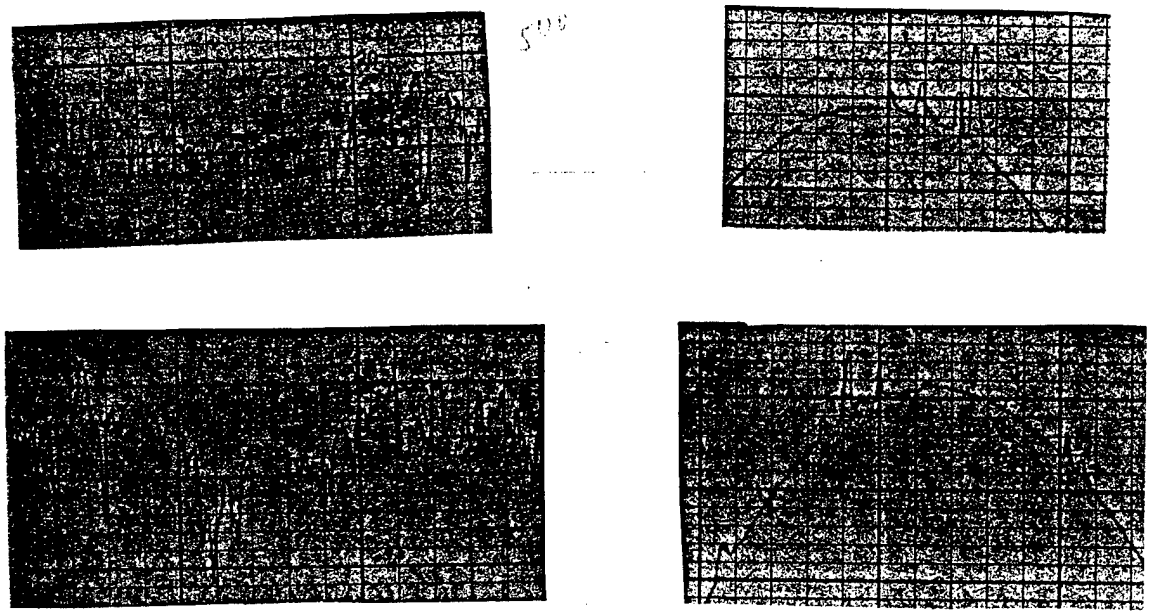

Figure 8 Profilometer traces of the aluminum sample and steel ball prior to cleaning, after (a) 500 fretting cycles, (b) 50,000 cycles, 20K×, for p_0 = 407 MPa, δ_t = 10 μm.

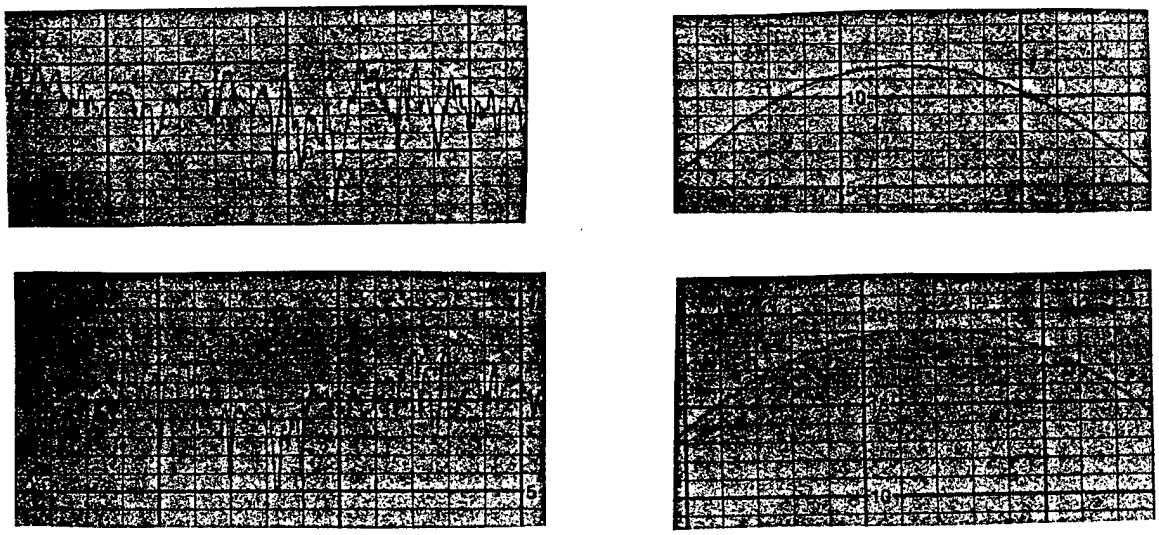

Figure 9 Profilometer traces of the aluminum sample and steel ball after cleaning, after (a) 500 fretting cycles, (b) 50,000 cycles, 20K×, for p_0 = 407 MPa, δ_t = 10 μm.

(a)

(b)

(c)

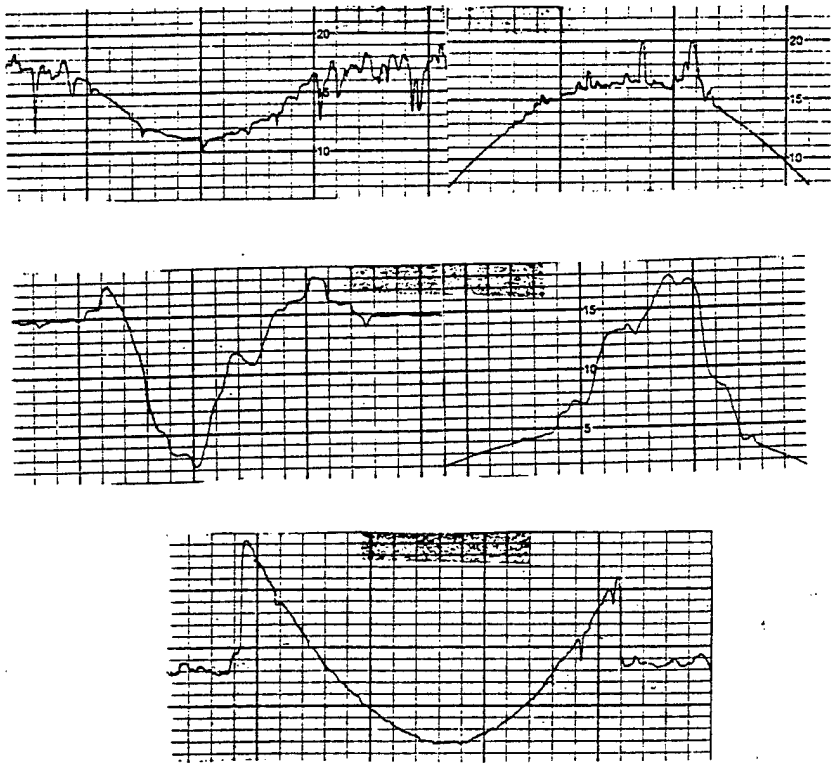

Figure 10 Profilometer traces of 2024-T3 sample and steel ball prior to cleaning, after (a) 500 fretting cycles, 10K×, (b) 50,000 cycles, 2K×, and (c) perpendicular to (b) for p_0 = 407 MPa, δ_t = 25 μm.

(a)

(b)

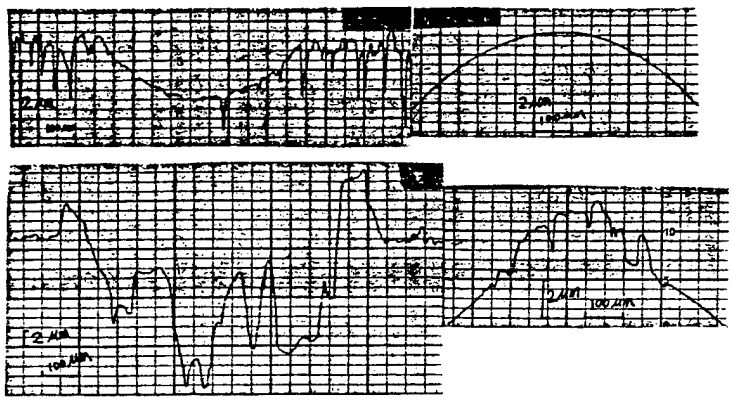

Figure 11 Profilometer traces of 2024-T3 sample and steel ball after cleaning, after (a) 5,000 fretting cycles, 10K×, (b) 50,000 cycles, 2K×, for p_0 = 407 MPa, δ_t = 25 μm.

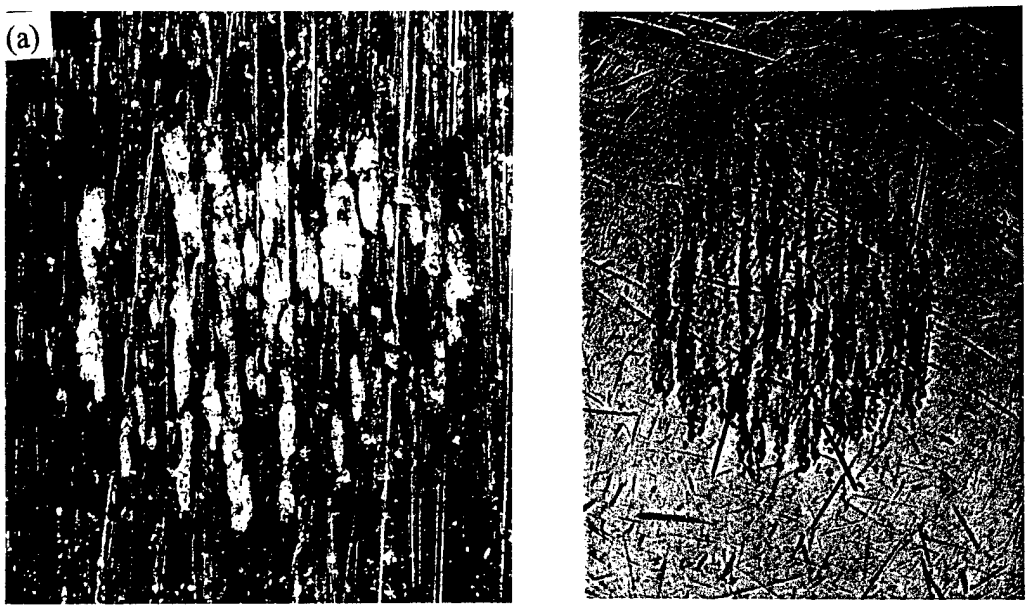

Figure 12 SEM and optical images of (a) 2024-T3, and (b) the counterface for 5,000 cycles with a frequency of 1 Hz under p_0 = 407 MPa for δ_t = 10 μm.

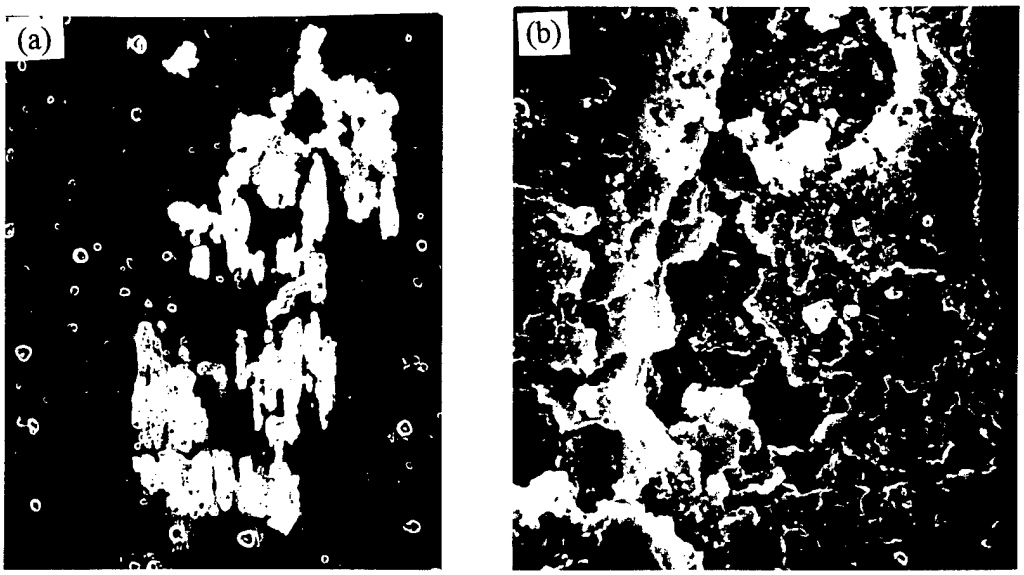

Figure 13 SEM images of asperities after cleaning: (a) low magnification, and (b) high magnification for broke junctures, showing severe adhesion-related damage.

Figure 14 SEM and optical images of 2024-T3 and corresponding counterface after (a) 5,000 cycles, showing mixed stick-slip, (b) 50,000 cycles, showing full slip pattern, with a frequency of 1 Hz under p_0 = 407 MPa for δ_t = 25 μm.

Figure 15 Highly magnified SEM and optical images of (a) 2024-T3, and (b) the counterface after N = 50,000 cycles in ambient air with a frequency of 1 Hz under p_0 = 407 MPa for δ_t = 25 μm, showing fatigue cracks on both surfaces.

APPENDIX E

FRETTING CORROSION OF 7075-T6 ALUMINUM ALLOY

by

M. Xue, J. Wert, P. Bastias, G. Hahn

Center for Materials Tribology

Vanderbilt University

Nashville, Tennessee 37235

Abstract: Fretting corrosion experiments of 7075-T6 were carried out with a unique fretting wear machine in both air and a saline solution. Fretting damage was significantly dependent on slip amplitude, contact pressure and environment. The coefficient of friction is generally higher in air with large total displacement than in saline solution. Specific wear rates were found to be more than 10 to 100 times higher in 3.5% NaCl solutions than those in air due to the synergistic interaction between electrochemical corrosion and fretting wear. The wear mechanisms were also discussed.

Keywords: fretting corrosion, fretting wear, coefficient of friction, specific wear rate, fretting regions, aluminum alloys, wear mechanisms.

Introduction

Fretting is defined as the small-amplitude oscillatory movement that may occur between contacting surfaces nominally at rest (Waterhouse, 1992). When fretting takes place in a corrosive environment, called fretting corrosion, the synergistic interaction between fretting and corrosion can enhance both mechanical and chemical damage to the

contacting materials. Riveted and pinned connections in airframes are susceptible to fretting corrosion problems. As reported by Hoeppner et al. (1995), corrosion and/or fretting have been a contributing factor in at least 687 incidents and accidents on aircraft in the US since 1975. Corrosion produces exfoliation swelling at the rivet and often requires costly repair work. Fretting initiates fatigue cracks, produces wear debris and results in premature failure of riveted and pinned connections. A better understanding of fretting and fretting corrosion will support efforts to reduce damage and unplanned maintenance for corrosion and fretting, and facilitate the early detection of the damage.

Aluminum alloys are notoriously prone to fretting corrosion since the fretting wear disrupts the protective oxide film, and exposes nascent metallic surfaces to further corrosion. Hard oxide particles produced by the fretting action assist the abrasion of the surfaces and produce more debris (Gahr, 1987; Hoeppner and Chandrasekaran, 1994; Waterhouse, 1992). One of the immediate consequences of fretting corrosion of aluminum alloys is the production of black aluminum oxide debris which contains about 23% metallic aluminum (Andrews et al., 1968). Particle sizes range from 1 μm down to less than 0.05 μm, depending on the degree of comminution. The coefficient of friction of aluminum under fretting conditions reported by different researchers ranges from $\mu = 0.05$ to $\mu = 0.7$ (Waterhouse, 1972; Takehira, 1994), and depends on tribosystems. It shows a common trend. Halliday and Hirst (1956) observed that the friction coefficient, μ, increases in the first few cycles and falls to a much lower value, after several hundred cycles, at which value it remains relatively constant. Waterhouse (1992) has summarized the material loss with a variety of contact geometries and methods. The specific wear rate ranges from, $W_s = 10^{-17}$ m^3/Nm to 10^{-13} m^3/Nm, and with a strong dependence on slip

amplitude. Goto, Ashida and Endo (1987) have reported that for the fretting wear of an Al-Zn-Mg alloy in contact with itself the fretting wear rate in wet air is about 3.5 times higher than in dry air. Takehira (1994) found the specific wear rate in distilled and sea water is approximately 100 times the rate in air for all three aluminum alloys tested with a cylinder-cross-cylinder configuration. The maximum wear rate is close to $W_s = 5.0\times10^{-13}$ m^3/Nm. No information has been found from literature on the material loss attending the fretting contact of steel with aluminum.

The interpretation of fretting data is complicated by the many variables--as many as 52--that affect surface damage (Beard, 1982). In recent years, friction logs and fretting maps have been increasingly used to describe the process. Three damage modes (Zhou and Vincent, 1992, 1995, 1997; Blanchard et al., 1995): (1) non-degradation (ND), (2) cracking and (3) particle detachment (PD) have been identified. There correspond with three distinguishable tangential force-displacement loop shapes (F_t-D curves) and active slip conditions: quasi-closed (stick), elliptic (mixed stick-slip) and parallelepiped (full slip), respectively. Two distinguishable fretting maps, i.e., running condition fretting map (RCFM) and material response fretting map (MRFM) (Zhou and Vincent, 1995, 1997), have been proposed and constructed for three aluminum alloys by displaying the specific influence of individual fretting variables on the fretting wear behavior.

In the present paper, the fretting corrosion of 7075-T6 in contact with itself and 52100 steel in both ambient air and saline solution was investigated using a piezoelectric-actuated, fretting wear. The influences of slip amplitude, contact pressure, number of cycles and environments on fretting corrosion were investigated. Tangential force-displacement hysteresis loops (F_t-D curves) were recorded during each experiment to

describe the running condition and also determine the coefficient of friction. Profilometry was used to measure the fretting wear scars and hence to calculate the wear volume and specific wear rate. Both scanning electron microscopy (SEM) and optical microscopy were used to examine the worn surfaces. Energy Dispersive Spectrometry (EDS) was carried out to analyze the elements in the wear debris. The effect of fretting variables and the wear mechanisms are discussed.

Experimental Procedure

Fretting corrosion measurements were performed with a unique fretting wear machine which is more fully described in somewhere else (Xue, et al., to be published). Small, sheet coupons of the test material are mounted in a holder attached to a stack of piezoelectric ceramics which serves as the actuator. In this way, small, and controlled total displacements in the range $\delta_t = 1.0$ μm to range $\delta_t = 100.0$ μm relative to a fixed conterface can be produced with frequencies from 0.05 Hz to 30 Hz. A schematic of the machine is shown in Figure 3.2. The machine can accommodate corrosive media at the contacting interface. The conterface, either a hardened steel sphere or a 7075-T6 hemisphere, is supported by a heavy mass riding on a linear bearing. The normal force between the sample and counterface is generated by 2 dead weights, acting through 2 sets of pulley and levers on the mass supporting the steel or aluminum counterface. The contact force was calibrated by applying known weights, and measuring the normal force generated on a Chatillon force gage normal to the mass. The displacement is regulated by the piezoelectric controller which compensates for hysteresis and drift. The friction force is transformed from the input voltage to the piezoelectric translator. Both the local slip

amplitude and the coefficient of friction are deduced from the friction force-displacement hysteresis loops. A schematic drawing of the typical tangential force-displacement hysteresis loop is demonstrated in Figure 3.4, where a is the elastic deformation, c is the local slip amplitude and (2a + c) is the total displacement, a constant value during each fretting test. The ratio, a/b, defines the system compliance.

Fretting wear and friction measurements were performed on 2.0 mm-thick AA 7075-T6 sheet in the as-received condition. The specimens, 38.1 mm × 17.0 mm rectangular blanks, were hand polished through 600 grit silicon carbide paper. The final polishing direction was parallel to the fretting direction. Specimens were rinsed with acetone in an ultrasonic cleaner before tests. Four types of counterface were used: 38.1 mm- and 6.35 mm-diameter, hardened 52100 balls with a hardness of HRC 62, as well as 19.05 mm- and 6.35 mm-diameter 7075-T6 hemispheres. All tests were conducted at room temperature and a frequency of 1.0 Hz, either under dry condition or with the contact region immersed in the 3.5% NaCl solution. The normal force was usually fixed at P = 37.30 N which yields a peak pressure of 407.0 MPa at the center of a Hertzian, 420 μm-diameter contact patch, though normal force, P = 18.6 N, 34.3N and 65.6 N, were also used. After each fretting test, a Talysurf Profilometer was used to measure the wear scar parallel and normal to the fretting direction, the profile measurements were made through the center of the wear scar prior to cleaning and after immersion for about 2.5 hours ultrasonically agitated action. The specific wear rate, W_s, is deduced from V, the volume of the wear scar revealed by the profilometer trace:

$$W_s = V / (2 \cdot \delta \cdot N \cdot P)$$

where δ is the average local slip amplitude, N is the number of cycles and P is the applied

normal force.

Experimental Results

Tangential Force-Displacement Loops and Coefficient of Friction

Figure 1 shows the tangential force-displacement hysteresis loops for the fretting of 7075-T6 against itself under a peak pressure of 1000 MPa, frequency of 1.0 Hz and in 3.5% NaCl solution. For the total displacement of 25 μm [Figure 1(a)], the friction is initially low, $\mu = 0.21$, till N = 1,500 cycles, then increases to an approximately constant value, $\mu = 0.30$. The tangential force-displacement loops are always symmetric with the shape of parallelepiped. The total displacement is accommodated by both elastic deformation within the testing machine and the relative slip between the contacting surfaces. For larger total displacement of 40 μm [Figure 1(b)], the friction is low, $\mu = 0.29$, at the beginning, then it increases to $\mu = 0.42$ with number of fretting cycles. After about N = 33850 cycles, the friction decreases to a relatively constant value, $\mu = 0.15$, and the stead-state loops are reached. The tangential force-displacement loops are parallelepiped-like shapes with an average slip amplitude of $\delta = 32$ μm throughout the test. The loops were symmetrical before N = 1434 cycles, then became non-symmetrical with rapid increase of friction at the upper end of the fretting displacement. Under the testing conditions, no quasi-closed or elliptic hysteresis loops are observed.

Coefficient of friction values deduced from above tangential force-displacement loops for different total displacements and in both dry and wet conditions are presented as a function of the number of fretting cycles in Figure 2. For 7075-T6 in contact with steel

[Figure 2(a)] under Hertzian pressure P = 407 MPa, the coefficient of friction in dry air is generally higher than in NaCl solution at the tested total displacement. In dry air the coefficient of friction shows two peak values following an initial low value, $\mu = 0.20$, then decreases to a steady state value, $\mu = 0.30$. The form of friction coefficient curves is the typical one observed in fretting wear tests. Alternatively in saline solution the friction coefficient curve shows more peaks with much more fluctuation. For fretting corrosion of 7075-T6 against itself [Figure 2(b)], the coefficient of friction shows similar fluctuation to that of 7075-T6 versus steel ball. The values of friction coefficient are higher at larger total displacement than those of smaller displacement. The steady-state (after 4×10^4 fretting cycles) values of the coefficient of friction are also listed in Table 5.1 for fretting tests of total displacement of 60 μm under three different levels of applied normal forces: P = 18.6 N, 37.3 N and 65.6N (corresponding with Hertzian contact pressures: $p_0 = 323$ MPa, 407 MPa and 491 MPa, respectively). With mediate and high contact pressures, the steady-state coefficient of friction is close to a similar value, i.e., $\mu = 0.22$ in dry, and $\mu = 0.17$ in wet conditions. With lower contact pressure, the steady-state coefficient of friction is relatively high, and is close to, $\mu = 0.33$.

Table 5.1 Coefficient of Friction of 7075-T6 against steel under $\delta_t = 60$ μm and different contact pressures

Hertzian Pressure	Coefficient of Friction	
(MPa)	In air	In saline solution
323	0.327	0.337
407	0.226	0.168
491	0.215	0.166

Wear Scar Profiles and SEM Observations

Figure 3 shows typical profiles of wear scars on 7075-T6 flat samples after fretting corrosion tests in saline solution. Figure 3(a) is the results from 7075-T6 fretting against 7075-T6 under the pressure $p_0 = 1000$ MPa after N = 40,000 cycles. Depending on imposed total displacement, the fretting damage increases significantly. From total displacement $\delta_t = 10$ μm, 25 μm, 40 μm to $\delta_t = 80$ μm, the area and depth of the fretting scars increase by about 6 and 5 times, respectively. The SEM image of the wear scar for test at $\delta_t = 80$ μm is presented in Figure 4(a), where the fretting direction can be easily identified according to the orientation of long score marks. There is also evidence of fretting corrosion debris adjacent to the fretting area. Figures 5.3(b) and 5.4(b) show the profiles and SEM picture of wear scars of the aluminum specimens from fretting corrosion of 7075-T6 against steel under the pressure $p_0 = 1{,}000$ MPa after N = 40,000 cycles. Similar to previous observation, the fretting damage depends strongly on the total displacement. However, the severity of damage is much less than that in the case of

7075-T6 versus 7075-T6. For $\delta_t = 10$ μm, materials loss is limited to pitting whilst for larger total displacement, the damage increases with apparently similar shape of wear scars. The SEM micrograph clearly shows large size of corrosion product which covers both fretted area and non-fretted area.

Specific Wear Rates

Two sets of measured specific wear values at a total displacement $\delta_t = 10$ μm are summarized in Figure 7: (1) 7075-T6 flat in contact with the steel sphere in saline; (2) 7075-T6 flat in contact with 7075-T6 hemisphere in ambient atmosphere. The contact pressures are $p_0 = 407$ MPa for the former and 453 MPa for the latter. These results show that, in both cases, the specific wear rates are high at the beginning of the tests, then dramatically decrease to low values around N = 500 cycles. The specific wear rates are relative constant thereafter, and are $W_s = 6.7 \times 10^{-14}$ m^3/Nm and $W_s = 9.70\times10^{-14}$ m^3/Nm for 7075-T6 against 7075-T6 in air and 7075-T6 against steel in saline solution, respectively.

Specific wear rates have also been plotted against average slip amplitude in Figure 8. The symbols used in the plot stand for: 7--7075-T6; w--in saline solution; d-- in air; p--aluminum against aluminum; b--aluminum against steel; 1--under Hertzian pressure $p_0 = 407$ MPa; and 2--under $p_0 = 1{,}000$ MPa. From this wide range of fretting configurations, it can be stated that the specific wear rates (W_s) is strongly dependent on slip amplitude, and W_s of aluminum versus aluminum is the highest in saline solution, followed by the order of aluminum fretting against steel in saline solution and aluminum in contact with steel in air. The specific wear rates are in the range: 10^{-15} $m^3/Nm < W_s <$

10^{-13} m^3/Nm for dry contact, and 10^{-13} $m^3/Nm < W_s < 10^{-12}$ m^3/Nm for wet contact.

Discussion

Coefficient of Friction

From Figures 5.1, 5.2 and Table 5.1, it is seen that the friction is generally lower in saline solution than in air. This may be due of the lubrication effect of water and softening effect (Gahr, 1987) of the corrosive media surrounding the contact area. Among two sets of tangential force-displacement curves, all hysteresis loops shows a short period of low friction at the beginning of each test, which can be attributed to the lubrication effect of preexisting oxide layer on the surfaces (Halliday and Hirst, 1956). For total displacement of 40 μm, the rapid increase of friction at upper end of the displacement, as shown in Figure 3(b), is due to the ridges (Blanchard et al., 1995; Xue, et al., to be published) formed at the top of the wear scar. The lower part does not show the similar increase in friction, which may be that the ridges are wiped away with the help of fluxing of the corrosive liquid, which eases the egress of the wear debris.

As also shown in Figure 2, the form of friction coefficient curves is the typical one found in fretting tests: an initially very low friction due to the oxide film in the first few cycles, which can be referred to the first hystereis loop of each set of the tangential force-displacement curves in Figure 1, immediately a high friction is observed in the first few hundred cycles because the oxide film breaks down due to fretting disruption, and thus metal-to-metal contact area increases, resulting in high friction. This has been also confirmed by measuring the electric resistance of the fretting pair (Waterhouse, 1972).

After the friction reaches maximum value, it decreases and fluctuates for some cycles and finally reaches the steady-state value. The reason is that in air the newly formed oxide film and the loose oxidized wear debris, i.e., so-called third bodies (Godet, 1984; Godet et al., 1980), accumulate between the contacting surfaces and accommodate the relative slip, which causes a decrease of friction. A typical compacted debris bed is shown in Figure 7. More peaks are attributed to the repeating re-adhesion of wear particles to the parent surface (Endo and Goto, 1978; Goto et al., 1987). This re-adhesion leads to the formation of a pile-up debris layer which acts as an obstruction during fretting motion so that the friction increases up to the second peak value. As the obstacle breaks down, the friction decreases again to a steady state value. The fluctuation of friction coefficient in saline solution implies that adhesion occurs periodically during fretting processes.

Specific Wear Rates

It seems that the initial Hertzian pressure has little effect on the specific wear rates of 7075-T6, as demonstrated in Figure 5. The wear rates of 7075-T6 vs. steel under p_0 = 1000 MPa are not significantly different from that under p_0 = 1000 MPa for all tested slip amplitudes. This observation is consistent with the result of steel against steel in air and seawater (Sato et al., 1986), but disagrees with Bill's review (1982) in which the specific wear rate is proportional to the applied normal load. The reason is that the increase of contact pressure was achieved by reducing the size of the counterface, instead of simply increasing the normal load. In addition, under constant total displacement the increase of applied normal force reduces the local slip amplitude, as demonstrated in Figure 8, which is similar to Waterhouse's observation (1972). This reduced slip amplitude produces less

materials loss and thus lower specific wear rate (Bill, 1982; Waterhouse, 1992). The result for 7075-T6 against 7075-T6 is similar to the findings of Goto, Ashida and Endo (1987) for higher slip amplitudes, e.g., 50 μm to 100 μm which represent the total displacement rather than the local values of slip amplitudes. The values for contact with steel in the saline environment are 5× the highest values reported by Goto et al. (1987). Their results may be lower because they used the profile traces of wear scars without removing wear debris and the total displacement rather than the local slip amplitude.

Aluminum suffers more fretting damage when it frets against itself than against steel, as illustrated in Figures 5.3 and 5.4. This is because similar metals have higher solubility, implying higher coefficient of friction (Hutchings, 1991), and thus produce more severe adhesive wear than dissimilar metal pairs (Rabinowicz, 1968). Under a total displacement of 40 m and p_0 = 407 MPa in air, the steady-state coefficient of friction is μ = 0.44 for 7075-T6 against itself, and μ = 0.28 for 7075-T6 in contact with steel. Profiles in Figure 9 clearly show that much more materials transfer occurs between 7075-T6 vs. 7075-T6 than 7075-T6 vs. steel.

Fretting Wear Mechanisms

It has been accepted that a synergistic interaction exists between fretting wear and corrosion. This synergistic interaction accelerates the wear-corrosion damage and causes severe materials loss. Through examining the changes of profiles and wear scars with increasing number of cycles, the wear-corrosion mechanisms may be identified. For 7075-T6 against steel in saline solution, Figure 10 suggests the aluminum samples

experience progressive surface damage and materials loss. The reason may be the interaction between fretting wear and corrosion through pit formation and growth, and material removal. In Figure 10(a), pits, such as A, B and C, were first formed possibly by adhesion and/or abrasion. After N = 5,000 cycles [Figure 10(b)], both the depth and the number of pits increases, and surface material is gradually removed. Further material removal occurred after N = 50,000 cycles, as shown in Figure 10(c). The bottom of the scar became smooth, and pits were also developed. In contrast, Figure 11, the profiles of wear scars from 7075 fretted against steel in air, indicates neither pits are developed nor large amount of material is lost. A following mechanism is proposed: after initial removal of preexisting oxide layer by abrasion, metal-to-metal contact prevails; then adhesive wear, which undoubtedly occurs in the early stages of fretting, results in materials transfer and introduces mechanical pitting in aluminum. Abrasion may also form microscopic grooves and dents which serve as sites for concentration cell corrosion (Madsen, 1992). In the mean time, corrosion further promotes the growth of these pits [Figures 10(a) and 10(b)] by rapidly dissolving aluminum atoms into the solution due to the unfavorable ratio of anode area to cathode area, as well as the high stress field from the asperity contact (Meletis and Lian, 1991). Microcracks are formed around these pits. Fretting action, such as, abrasion, adhesion and fatigue mechanisms, removes the remaining weakened materials (including the newly formed oxide layer). During the process, new pits are continuously initiated and enlarged by wear and corrosion. This process is facilitated by the localized nature of fretting and corrosion (Meletis and Lian, 1991). Pits and cracks surrounding those pits can be clearly seen in Figure 12(a). This mechanism may explains the observation in Figure 5, where the specific wear rates

decrease with increasing number of fretting cycles. Because pits resulting from adhesion and corrosion act as reservoirs for the saline solution which separates the contact surfaces. While pitting, abrasion and fatigue still continue to remove materials at a somewhat constant rate; adhesion seems not to play an important role in the later stage of the fretting corrosion. Therefore, specific wear rate decreases at the beginning to a constant rate.

For fretting wear in air, the main fretting damage can be attributed to adhesion wear which results in material transfer, as seen in Figure 9(b). Large amount of plastic deformation has occurred locally and changed the contact conditions. Surface cracks and removal of oxide platelets suggest that fatigue and delamination (Waterhouse and Wharton, 1976) are the damage mechanisms. Figure 12(b) is an exemplary picture of the delamination process. Not much difference is found between 7075-T6 and 2024-T3 in the shapes of tangential force-displacement hysteresis loops and forms of coefficient of friction. Therefore, the fretting process for examined 7075-T6 is similar to that for 2024-T3 (Xue, et al., to be pulished), and can be stated as: when two materials are brought together asperities on the weaker material deform plastically and elastically first to accommodate the harder counterface. The fretting motion causes the deformed asperities to suffer further plastic deformation or fatigue damage. The debris, resulting from the breakdown of preexisting oxide layer and adhesive junctures and also delamination of surface layers, fills in the gaps between the strip-shaped asperities and the surface roughness decreases. Wiping the debris produces new metal-to-metal contact, which increases the possibility of juncture formation and growth. However, cyclic displacement may rupture the junctures by either overloading or fatigue mechanism, and result in

material transfer. This material transfer may introduce surface or subsurface microcracks. The formation of surface and subsurface microcracks enhances the possibility of delamination and fatigue.

Conclusion

(1) Only the full slip mode is observed in the fretting corrosion of 7075-T6 aluminum alloy in saline solution, though mixed stick-slip mode appears in fretting experiments conducted in air under the same total displacement. This is a consequence of the lower friction resistance obtained in saline solution. Under full slip mode, severe adhesion and metal transfer occur in the given tribosystem.

(2) Curves of coefficient of friction have the typical form that is usually found in fretting wear tests, but there are two or more peaks and more fluctuation at large total displacement and in saline solution. The value of the coefficient of friction is significantly dependent on slip amplitude, environments and applied normal force.

(3) The specific wear rate is initially high for small amount of fretting cycles, then reduces to an approximately cycle independent value of the order of $Ws = 10^{-13}$ m^3/Nm. Specific wear rates are more than 10 times higher in NaCl solution than in air due to the synergistic interaction of fretting and corrosion. The highest specific wear rate is the highest from 7075-T6 vs. 7075-T6 in saline solution, then followed by 7075-T6 vs. steel in saline solution; the lowest wear rate is from 7075-T6 vs. steel in air.

(4) Abrasion, adhesion and fatigue are the main damage mechanisms involved in the fretting corrosion of 7075-T6 in air. Adhesion, pitting, abrasion and fatigue all contribute to the fretting corrosion of 7075-T6 in saline solution.

(5) A fretting corrosion mechanism was proposed to explain the synergistic interaction of fretting and corrosion for aluminum alloys in various fretting conditions. It states that the initial breakdown of adhesive junctures produces mechanical pits, and abrasion also causes grooves and dents; those pits and dents form corrosion cells and can grow by atom dissolving. Microcracks are initiated around those highly stress/strain concentrated pits, and abrasion wear, fatigue and delamination facilitate the removal of cracked materials directly underneath the counterface.

Acknowledgment

The authors wish to thank Bill Gentry and James Hightower for their assistance in the construction of the fretting wear machine. Dr. Sanjiv Kulkarni is appreciated for his EDS work. This work was supported with a grant from the Air Force Office of Scientific Research (F49620-93-1-0488).

References

AGARD Corrosion Handbook, Vol 1, Aircraft Corrosion: Causes and Case Histories, ed. by Wallace, W., Hoeppner, D. and Kandachar, P., Specialized Printing Services Ltd., 1985.

Bill, R. C., Review of Factors That Influence Fretting Wear. In Material Evaluation under Fretting Conditions, ASTM STP 780, Philadelphia, 1982, 165-182.

Blanchard, P., Colombie, C., Pellerin, V., Fayeulle, S., Vincent, L., "Material Effects in Fretting Wear: Application to Iron, Titanium and Aluminum Alloys", Metall. Trans. A, Vol. 22A, July 1995, p1535-1547.

Gahr, K-H. Z., Microstructure and Wear of Materials, Elsevier, 1987.

Halliday, T. S., and Hirst, W., "The Fretting Corrosion of Mild Steel", Proc. R. Soc.

London, Ser. A, 236 (1956) 411.

Hoeppner, D. W., and Chandrasekaran, V., "Fretting in Orthopedic Implants: A Review", Wear 173 (1994) 189-197.

Hoeppner, D. W., Grimes, A., Hoeppner, A., Ledesma, J., Mills, T. and Shah, A., "Corrosion and Fretting as Critical Aviation Safety Issues", 18th ICAF Symposium, Melbourne, Australia, May 1-5, 1995.

Goto, H., Ashida, M., Endo, K., "The Influence of Oxygen and Water Vapor on the Friction and Wear of An Aluminum Alloy under Fretting Conditions", Wear, Vol. 116, 1987, pp. 141-155.

Takehira, A., "Fretting Wear of An Aluminum and Two Kinds of its Alloys in Marine Environment", Proc. JSME A, Vol. 65, No. 572, April 1994.

Waterhouse, R. B., Fretting Corrosion, Pergaman Press, 1972.

Waterhouse, R. B., "Fretting Wear", ASM Metals Handbook, Vol. 18 (1992) 242-256, ASM International.

Xue, M., Wert, J., Bastias, P., and Hahn, G., "A Piezoelectric-Actuated Fretting Wear Machine", to be published.

Xue, M., Wert, J., Bastias, P., and Hahn, G., "Fretting Corrosion of 2024-T3 Aluminum Alloy", to be published.

Zhou, Z. R., Fayeulle, S., Vincent, L., "Cracking Behavior of Various Aluminum Alloys during Fretting Wear", Wear 155 (1992) 317-330.

Zhou, Z. R., Vincent, L., "Mixed Fretting Regime", Wear 181-183(1995)531-536.

Zhou, Z. R., Vincent, L., "Cracking Induced by Fretting of Aluminum Alloys", Journal of Tribology, Vol. 119, 1997.

LIST OF FIGURES

Figure 1 Schematic diagram of the fretting wear machine.

Figure 2 Schematic drawing of a tangential force-displacement (F_t-D) loop.

Figure 3(a) Evolution of friction logs with number of fretting cycles for 7075-T6 vs. 7075-T6 with f = 1.0 Hz under p_0 = 1000 MPa at a total displacement: δ_t = 25 μm in saline solution.

Figure 3(b) Evolution of friction logs with number of fretting cycles for 7075-T6 vs. 7075-T6 with f = 1.0 Hz under p_0 = 1000 MPa at total displacement: δ_t = 25 μm in saline solution.

Figure 4 Typical friction coefficient curves as a function of number of fretting cycles: (a) 7075-T6 fretting against 52100 steel with δ_t = 40 μm and p_0 = 407 MPa in both air and saline solution, (b) 7075-T6 in contact with itself under p_0 = 1000 MPa at δ_t = 25 μm and δ_t = 40 μm in saline solution.

Figure 5(a) Profilometer measurements of the wear scars produced by N = 4×10^4 fretting cycles for 7075-T6 samples against 7075-T6 in saline solution with p_0 = 1000 MPa, δ_t = 10 μm, 25 μm, 40 μm, 80 μm, respectively.

Figure 5(b) Profilometer measurements of the wear scars produced by N = 4×10^4 fretting cycles for 7075-T6 samples against steel in saline solution with p_0 = 1000 MPa, δ_t = 10 μm, 25 μm, 40 μm, 80 μm, respectively.

Figure 6 Examples of wear scars obtained after N = 4×10^4 fretting cycles for p_0 = 1000 MPa, δ_t = 80 μm and f =1.0 Hz in saline solution for 7075-T6 against: (a) a 7075-T6 hemisphere, (b) a 52100 steel sphere.

Figure 7 Variation of the specific wear rate, W_s, with the number of cycles for 7075-T6 against a 52100 sphere (•) in saline solution, and against 7075-T6 (□) in ambient air for p_0 = 1000 MPa and f =1.0 Hz.

Figure 8 Variation of the specific wear rate, W_s, with slip amplitude for 7075-T6 against 7075-T6 in saline solution with p_0 = 1000 MPa (•), and p_0 = 407 MPa (■); against a steel sphere in saline solution with p_0 = 1000 MPa (O), and p_0 = 407 MPa (▲); and against steel in ambient air for p_0 = 407 MPa (Δ).

Figure 9 SEM picture of uncleaned 7075-T6 sample against a steel ball for δ_t = 25 μm and p_0 = 407 MPa after N = 10^4 cycles, showing compacted debris bed in the center and dispersive, fine debris particles around the contact area.

Figure 10 Plot of fretting ratio, slip amplitude/total displacement (δ/δ_t), as a function of the normal force for 7075-T6 after $N = 4\times10^4$ fretting cycles against 7075-T6 in ambient air (▼) and saline solution (Δ), against steel in air (O) and in saline solution (•).

Figure 11 Profilometer traces of 7075-T6 samples after $N = 4\times10^4$ fretting cycles for p_0 = 1000 MPa and δ_t = 10 μm in ambient air: (a) against a steel sphere, (b) against 7075-T6 hemisphere.

Figure 12 Profilometer traces of cleaned 7075-T6 sample against a steel ball after (a) N = 500, (b) N = 5,000, (c) N = 50,000 fretting cycles in saline solution for p_0 = 407 MPa and δ_t = 40 μm.

Figure 13 Profilometer traces of cleaned 7075-T6 sample against a steel ball after (a) N = 5,000, (b) N = 15,000 fretting cycles in ambient air for p_0 = 407 MPa and δ_t = 80 μm.

Figure 14 SEM images of high magnification for typical wear scars resulted from fretting 7075-T6 against steel in saline solution, showing (a) pits and cracks initiated from these pits, (b) fish scale-liked topography and the delamination of the scales.

LIST OF FIGURES

Figure 1 Schematic diagram of the fretting wear machine.

Figure 2 Schematic drawing of a tangential force-displacement (F_t-D) loop.

Figure 3(a) Evolution of friction logs with number of fretting cycles for 7075-T6 vs. 7075-T6 with f = 1.0 Hz under p_0 = 1000 MPa at a total displacement: δ_t = 25 μm in saline solution.

Figure 3(b) Evolution of friction logs with number of fretting cycles for 7075-T6 vs. 7075-T6 with f = 1.0 Hz under p_0 = 1000 MPa at total displacement: δ_t = 25 μm in saline solution.

Figure 4 Typical friction coefficient curves as a function of number of fretting cycles: (a) 7075-T6 fretting against 52100 steel with δ_t = 40 μm and p_0 = 407 MPa in both air and saline solution, (b) 7075-T6 in contact with itself under p_0 = 1000 MPa at δ_t = 25 μm and δ_t = 40 μm in saline solution.

Figure 5(a) Profilometer measurements of the wear scars produced by N = 4×10^4 fretting cycles for 7075-T6 samples against 7075-T6 in saline solution with p_0 = 1000 MPa, δ_t = 10 μm, 25 μm, 40 μm, 80 μm, respectively.

Figure 5(b) Profilometer measurements of the wear scars produced by N = 4×10^4 fretting cycles for 7075-T6 samples against steel in saline solution with p_0 = 1000 MPa, δ_t = 10 μm, 25 μm, 40 μm, 80 μm, respectively.

Figure 6 Examples of wear scars obtained after N = 4×10^4 fretting cycles for p_0 = 1000 MPa, δ_t = 80 μm and f =1.0 Hz in saline solution for 7075-T6 against: (a) a 7075-T6 hemisphere, (b) a 52100 steel sphere.

Figure 7 Variation of the specific wear rate, W_s, with the number of cycles for 7075-T6 against a 52100 sphere (•) in saline solution, and against 7075-T6 (□) in ambient air for p_0 = 1000 MPa and f =1.0 Hz.

Figure 8 Variation of the specific wear rate, W_s, with slip amplitude for 7075-T6 against 7075-T6 in saline solution with p_0 = 1000 MPa (•), and p_0 = 407 MPa (■); against a steel sphere in saline solution with p_0 = 1000 MPa (O), and p_0 = 407 MPa (▲); and against steel in ambient air for p_0 = 407 MPa (Δ).

Figure 9 SEM picture of uncleaned 7075-T6 sample against a steel ball for δ_t = 25 μm and p_0 = 407 MPa after N = 10^4 cycles, showing compacted debris bed in the center and dispersive, fine debris particles around the contact area.

Figure 10 Plot of fretting ratio, slip amplitude/total displacement (δ/δ_t), as a function of the normal force for 7075-T6 after $N = 4\times10^4$ fretting cycles against 7075-T6 in ambient air (▼) and saline solution (Δ), against steel in air (O) and in saline solution (•).

Figure 11 Profilometer traces of 7075-T6 samples after $N = 4\times10^4$ fretting cycles for p_0 = 1000 MPa and δ_t = 10 μm in ambient air: (a) against a steel sphere, (b) against 7075-T6 hemisphere.

Figure 12 Profilometer traces of cleaned 7075-T6 sample against a steel ball after (a) N = 500, (b) N = 5,000, (c) N = 50,000 fretting cycles in saline solution for p_0 = 407 MPa and δ_t = 40 μm.

Figure 13 Profilometer traces of cleaned 7075-T6 sample against a steel ball after (a) N = 5,000, (b) N = 15,000 fretting cycles in ambient air for p_0 = 407 MPa and δ_t = 80 μm.

Figure 14 SEM images of high magnification for typical wear scars resulted from fretting 7075-T6 against steel in saline solution, showing (a) pits and cracks initiated from these pits, (b) fish scale-liked topography and the delamination of the scales.

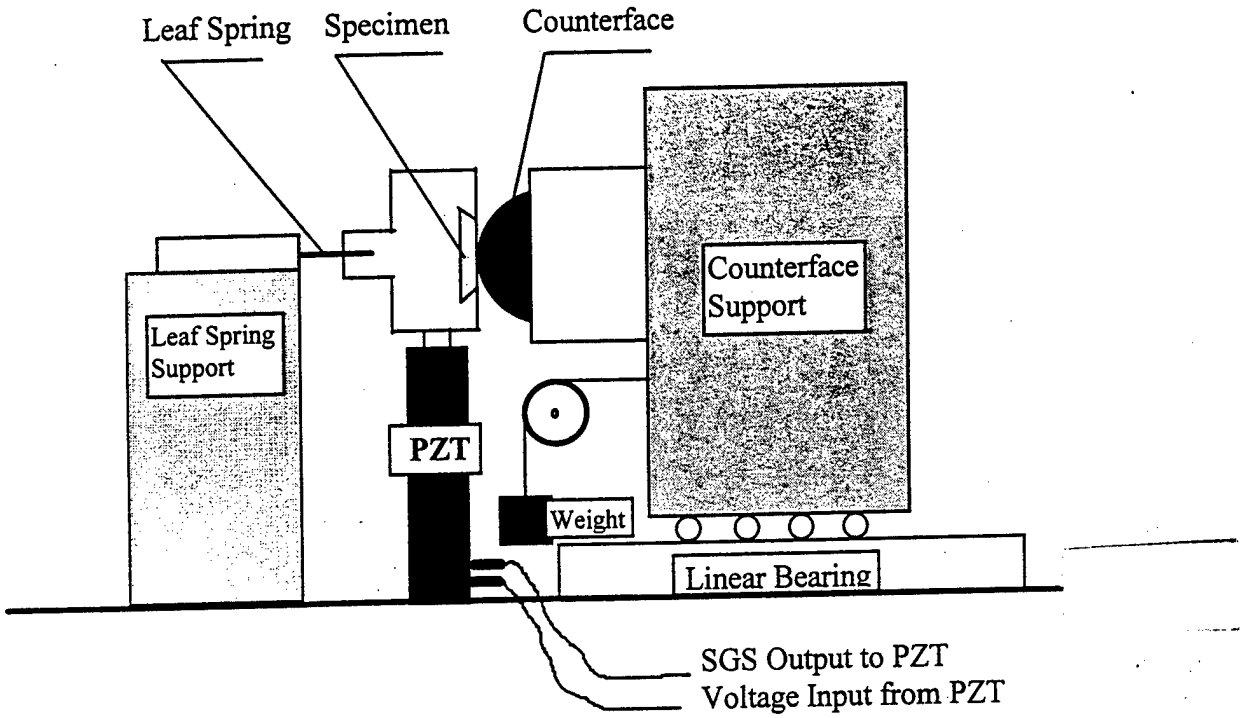

Figure 1 Schematic diagram of the fretting wear machine (mechanical part)

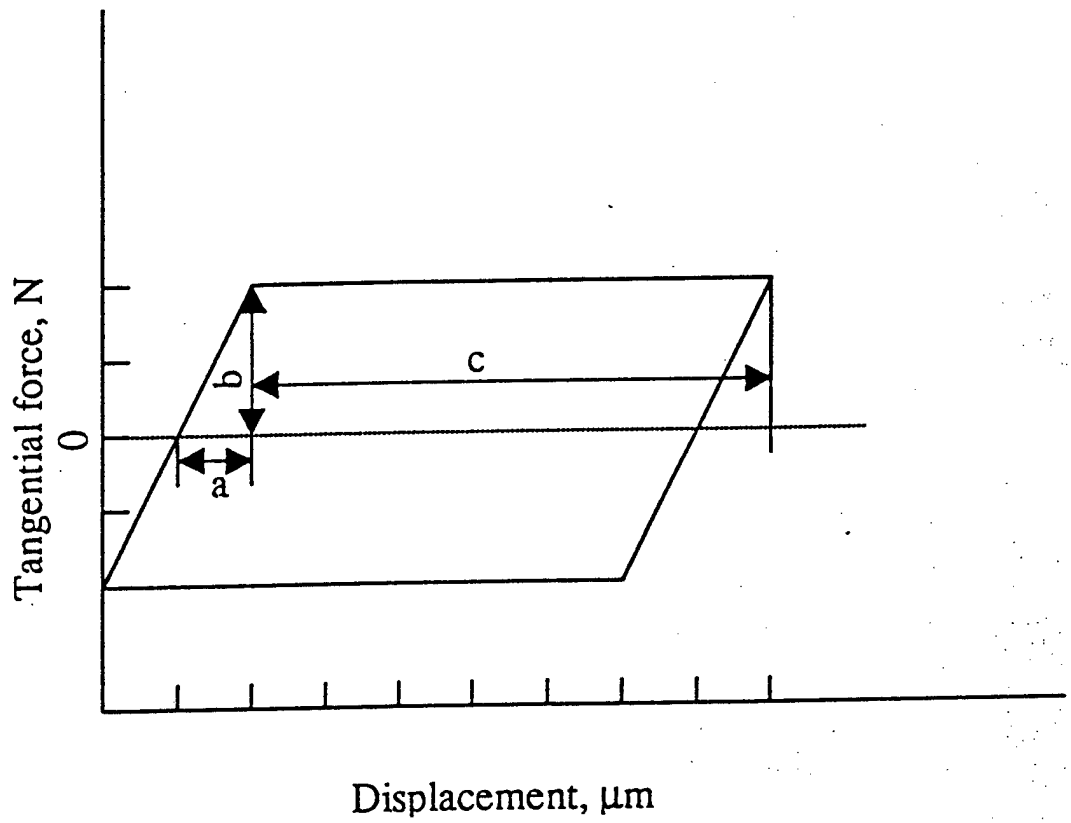

Figure 2 Schematic drawing of a typical tangential force-displacement (Ft-D) hysteresis loop. a/b defines the system compliance and c is the local slip amplitude.

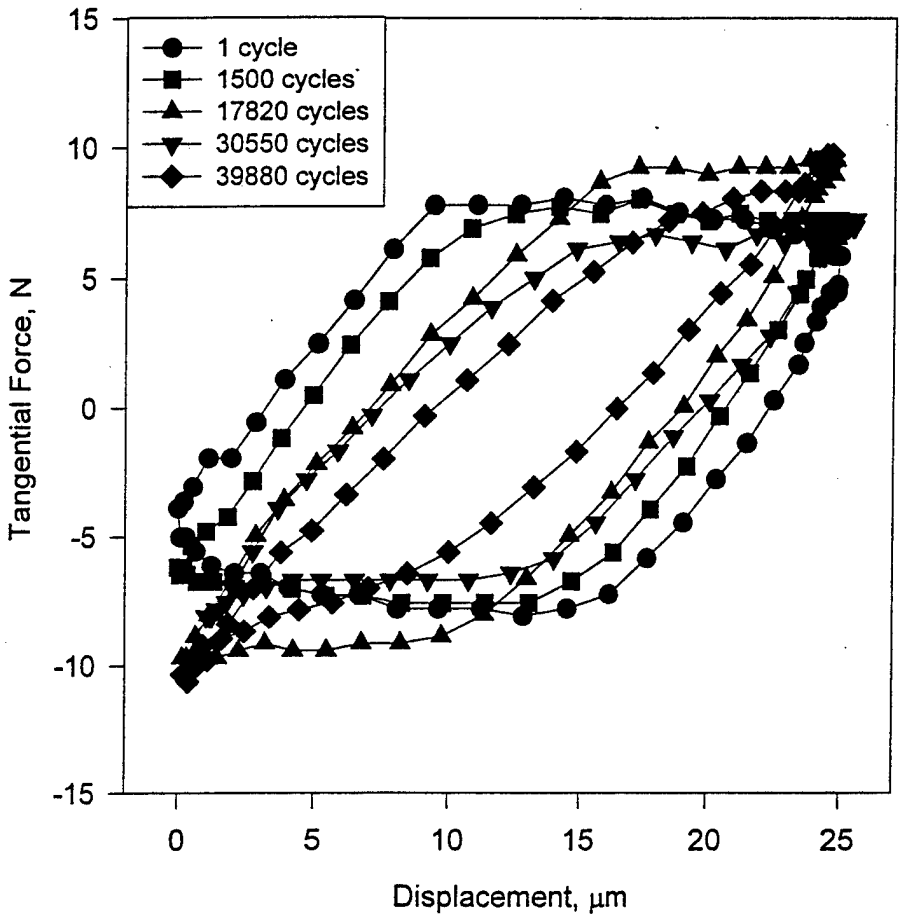

Figure 3(a) Evolution of friction logs with number of fretting cycles for 7075-T6 vs. 7075-T6 with f = 1.0 Hz under p_0 = 1000 MPa at a total displacement δ_t = 25 μm in saline solution.

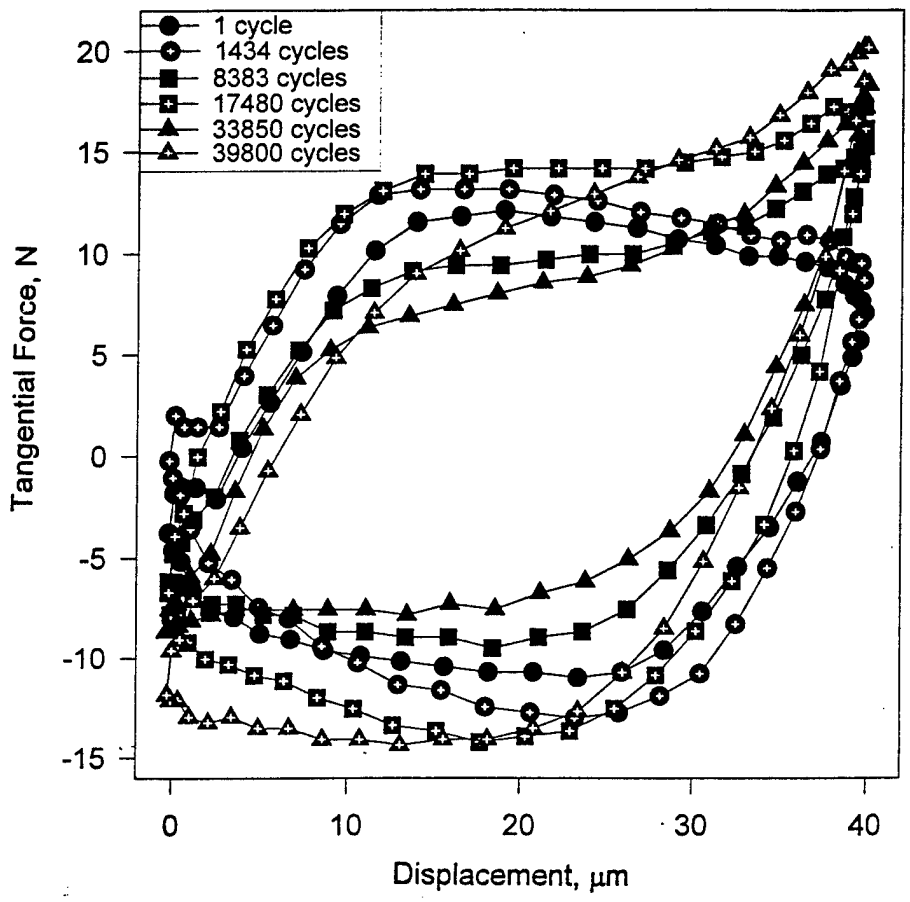

Figure 3(b) Evolution of friction logs with number of fretting cycles for 7075-T6 vs. 7075-T6 with f = 1.0 Hz under p_0 = 1000 MPa at a total displacement δ_t = 40 μm in saline solution.

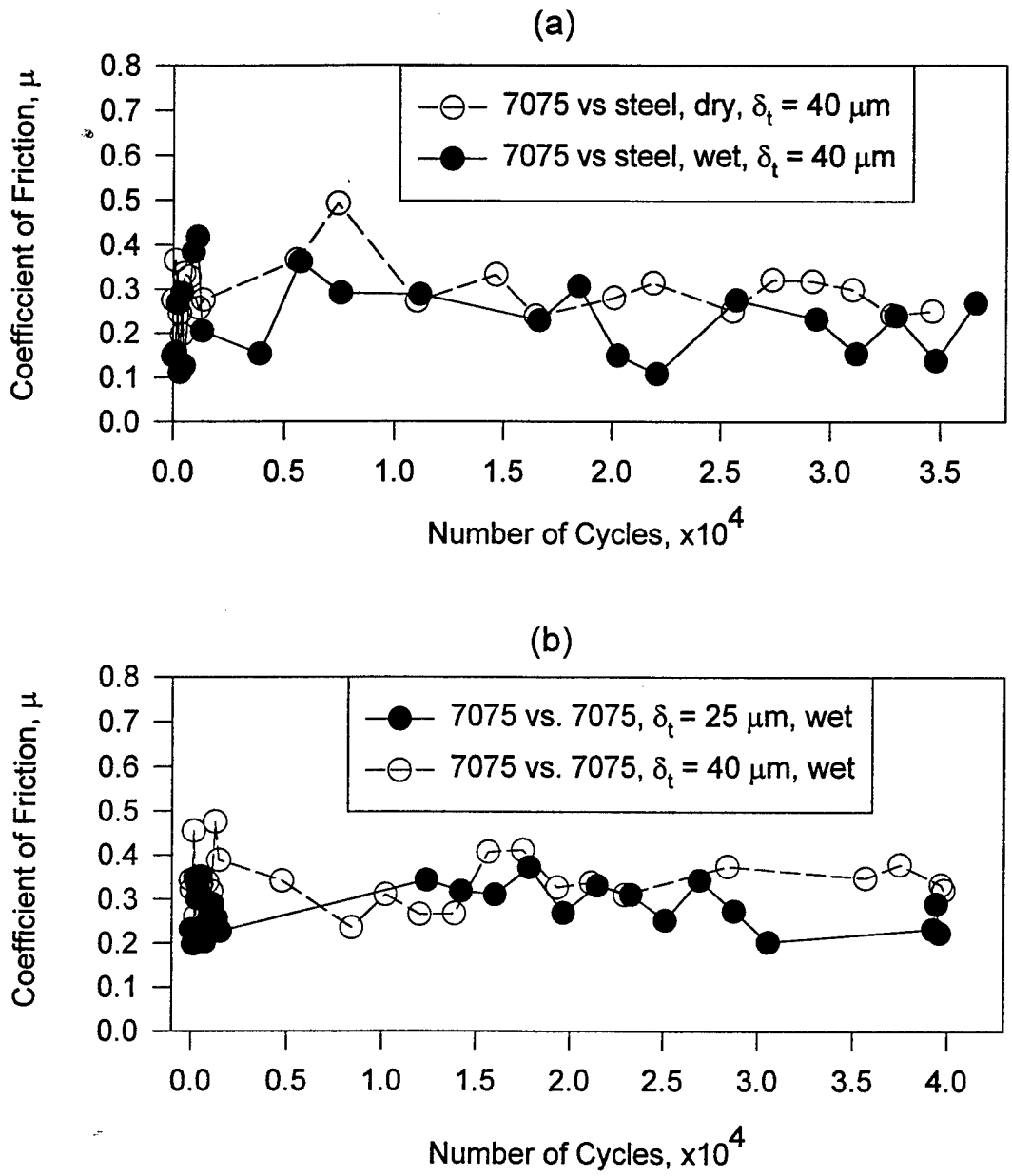

Figure 4 Typical friction coefficient curves as the function of number of fretting cycles: (a) 7075-T6 fretting against 52100 steel in both air and saline solution, (b) 7075-T6 in contact with itself at different total displacement in saline solution.

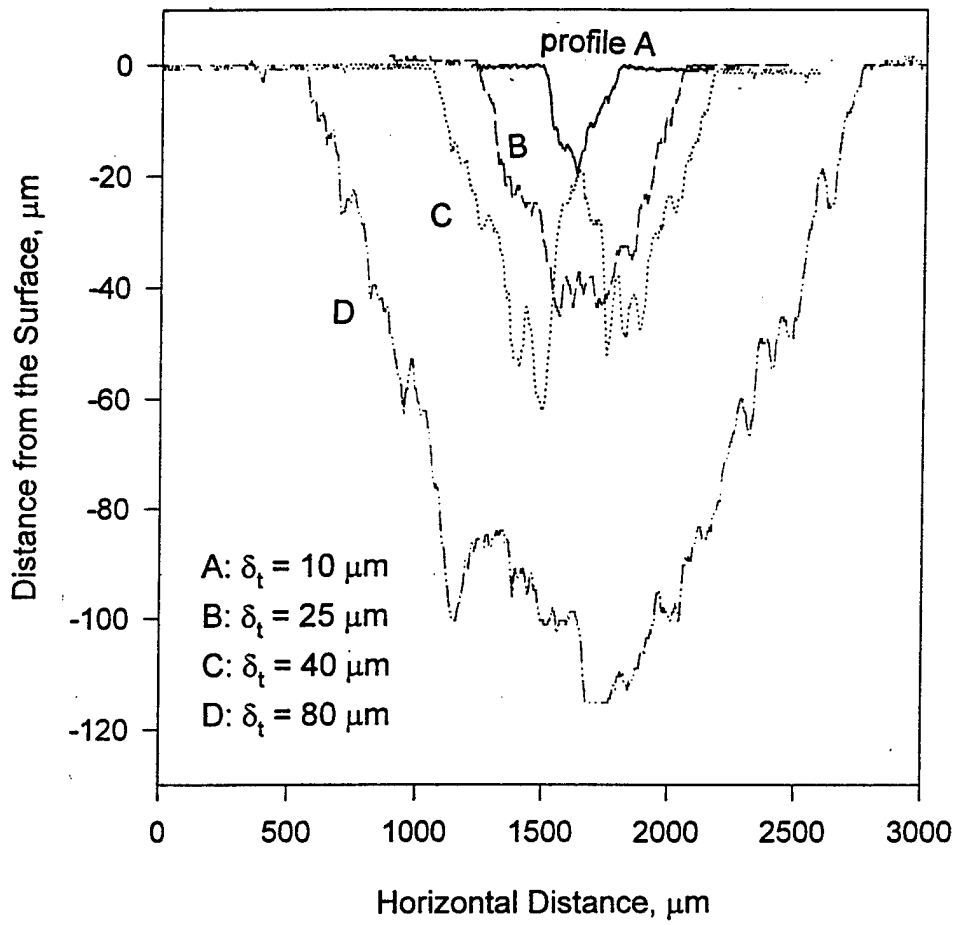

Figure 5(a) Profilometer measurements of the wear scars produced by $N = 4\times10^4$ fretting cycles for 7075-T6 samples against 7075-T6 in saline solution with $p_0 = 1000$ MPa, and total displacement $\delta_t = 10$ μm, 25 μm, 40 μm and 80 μm, respectively.

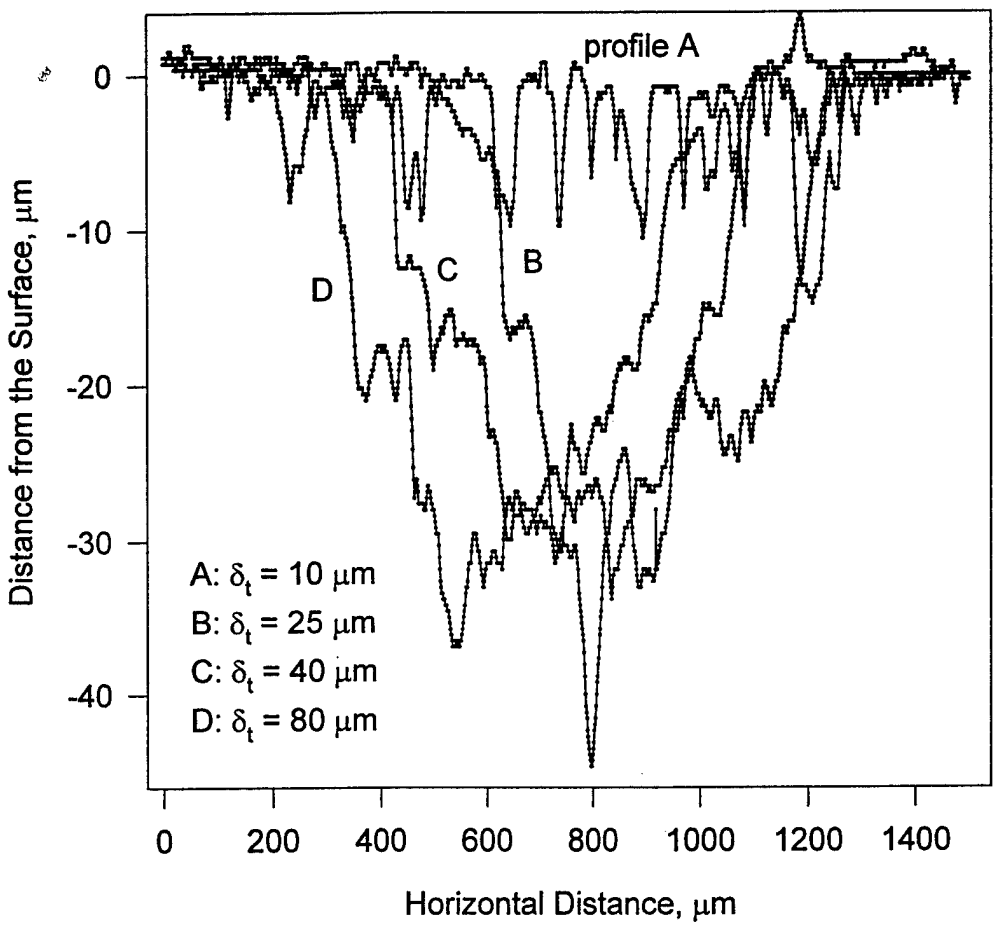

Figure 5(b) Profilometer measurements of the wear scars produced by $N = 4\times10^4$ fretting cycles for 7075-T6 samples against steel in saline solution with $p_0 = 1000$ MPa, and total displacement $\delta_t = 10$ μm, 25 μm, 40 μm and 80 μm, respectively.

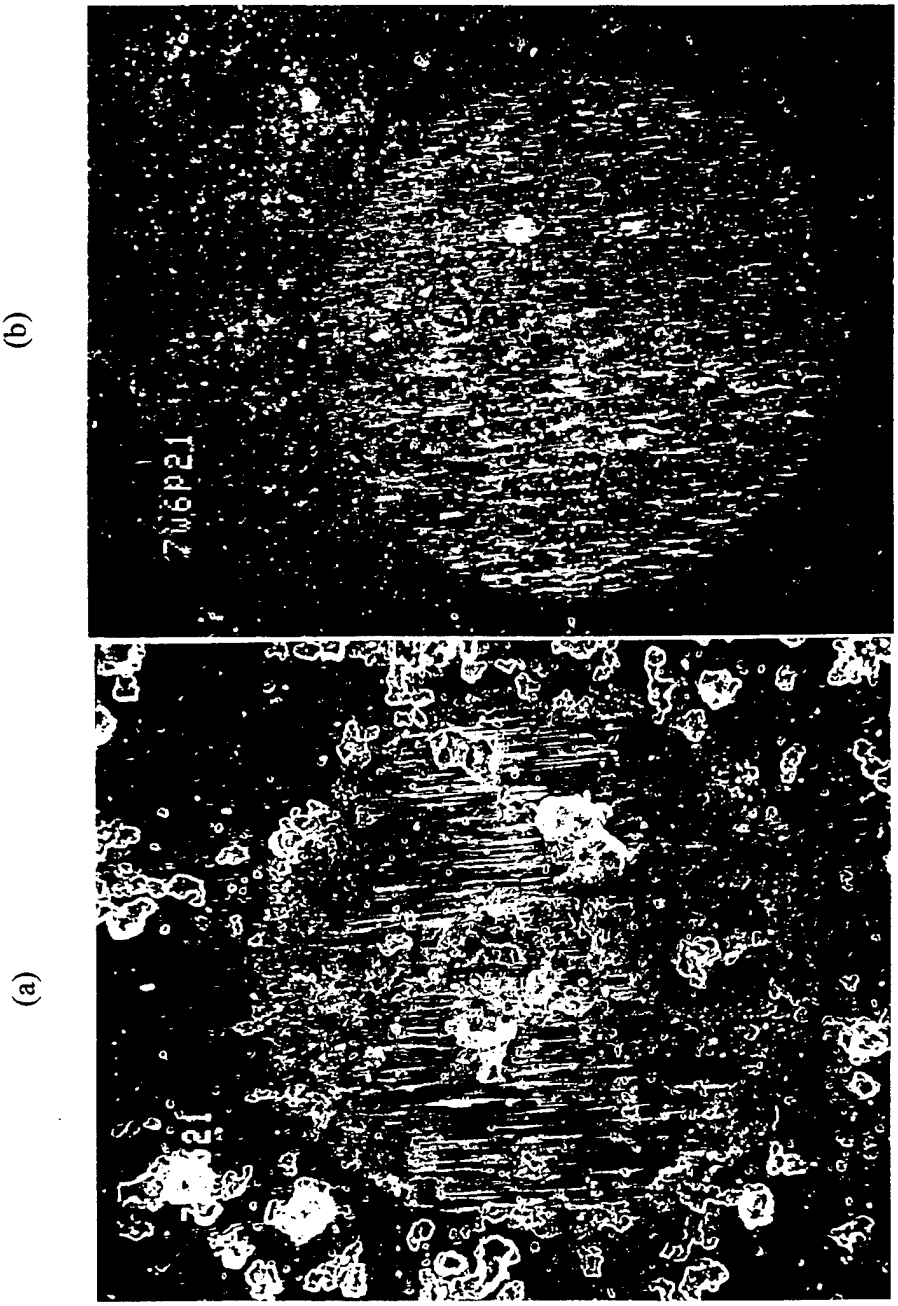

Figure 6 Micrographs of wear scars obtained after $N = 4\times10^4$ fretting cycles for p_0 = 1000 MPa, δ_t = 80 μm and f =1.0 Hz in saline solution for 7075-T6 against: (a) a 7075-T6 hemisphere, (b) a 52100 steel sphere.

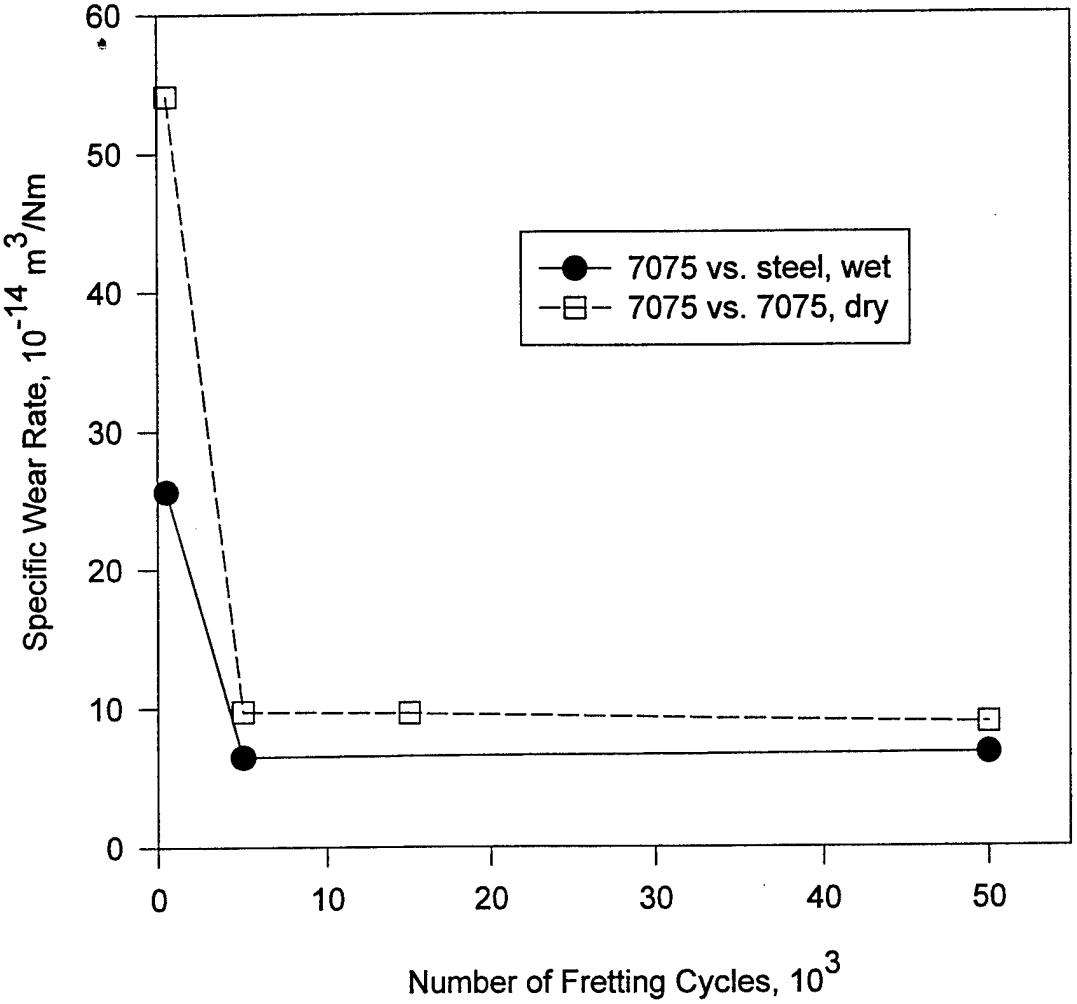

Figure 7 Variation of the specific wear rate, W_s, with the number of cycles for 7075-T6 against a 52100 sphere (•) in saline solution, and against 7075-T6 (□) in ambient air for p_0 = 1000 Mpa, δ_t = 40 μm and f =1.0 Hz.

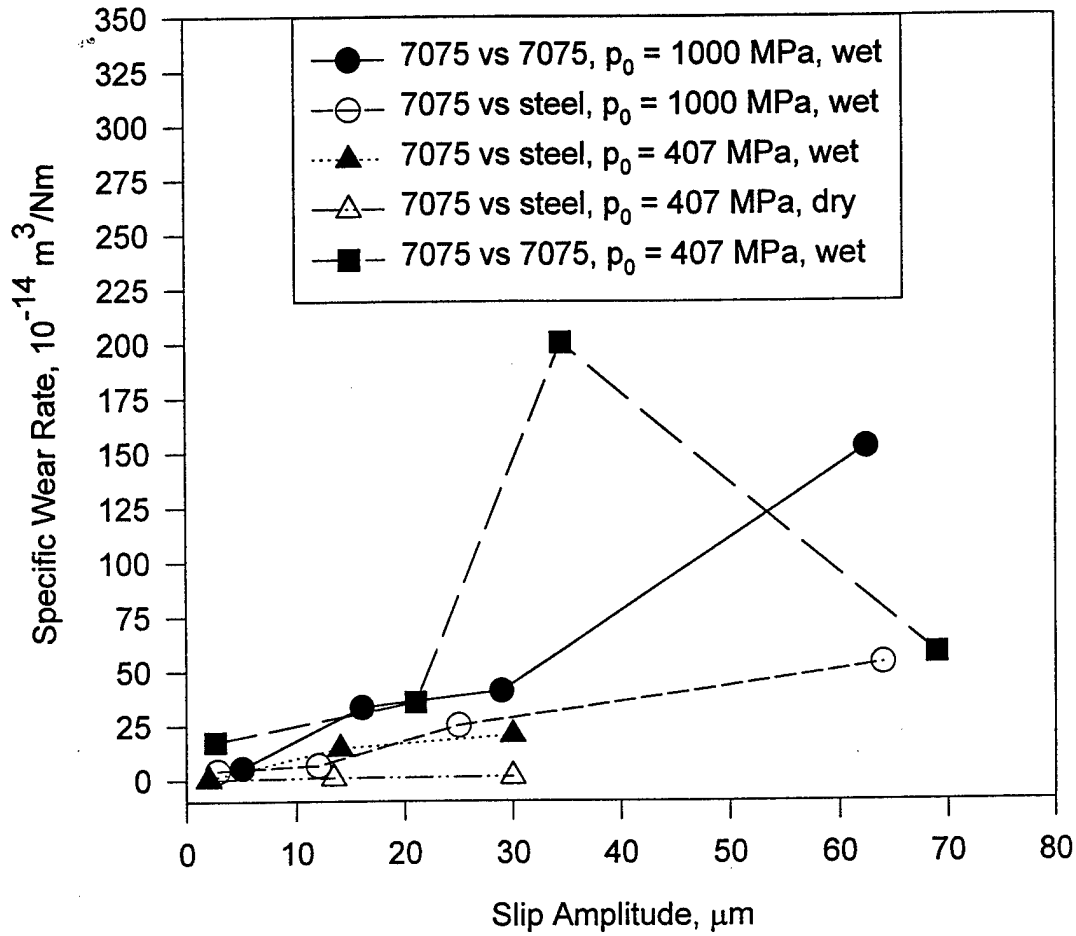

Figure 8 Variation of the specific wear rate, W_s, with slip amplitude for 7075-T6 against 7075-T6 in saline solution with p_0 = 1000 MPa (●), and p_0 = 407 MPa (■); against steel in saline solution with p_0 = 1000 MPa (○), and p_0 = 407 MPa (▲); and against steel in ambient air for p_0 = 407 MPa (Δ).

Figure 9 SEM picture of uncleaned 7075-T6 sample against a steel ball for $\delta_t = 25$ μm and $p_0 = 407$ MPa after $N = 10^4$ cycles, showing compacted debris bed in the center and dispersive, fine debris particles around the contact area.

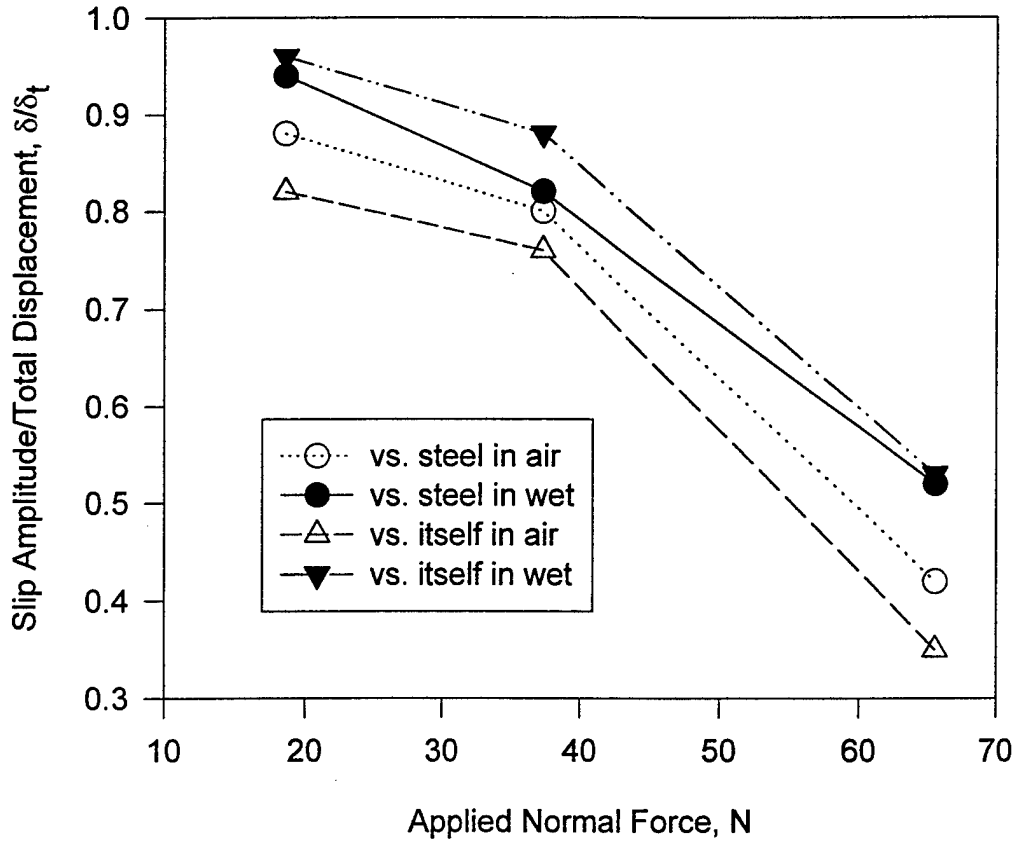

Figure 10 Plot of fretting ratio, slip amplitude/total displacement (δ/δ_t), as a function of the normal force for 7075-T6 after $N = 4\times10^4$ fretting cycles against 7075-T6 in ambient air (▼) and saline solution (Δ), against steel in air (O) and in saline solution (●). Higher normal force leads to smaller local slip amplitude.

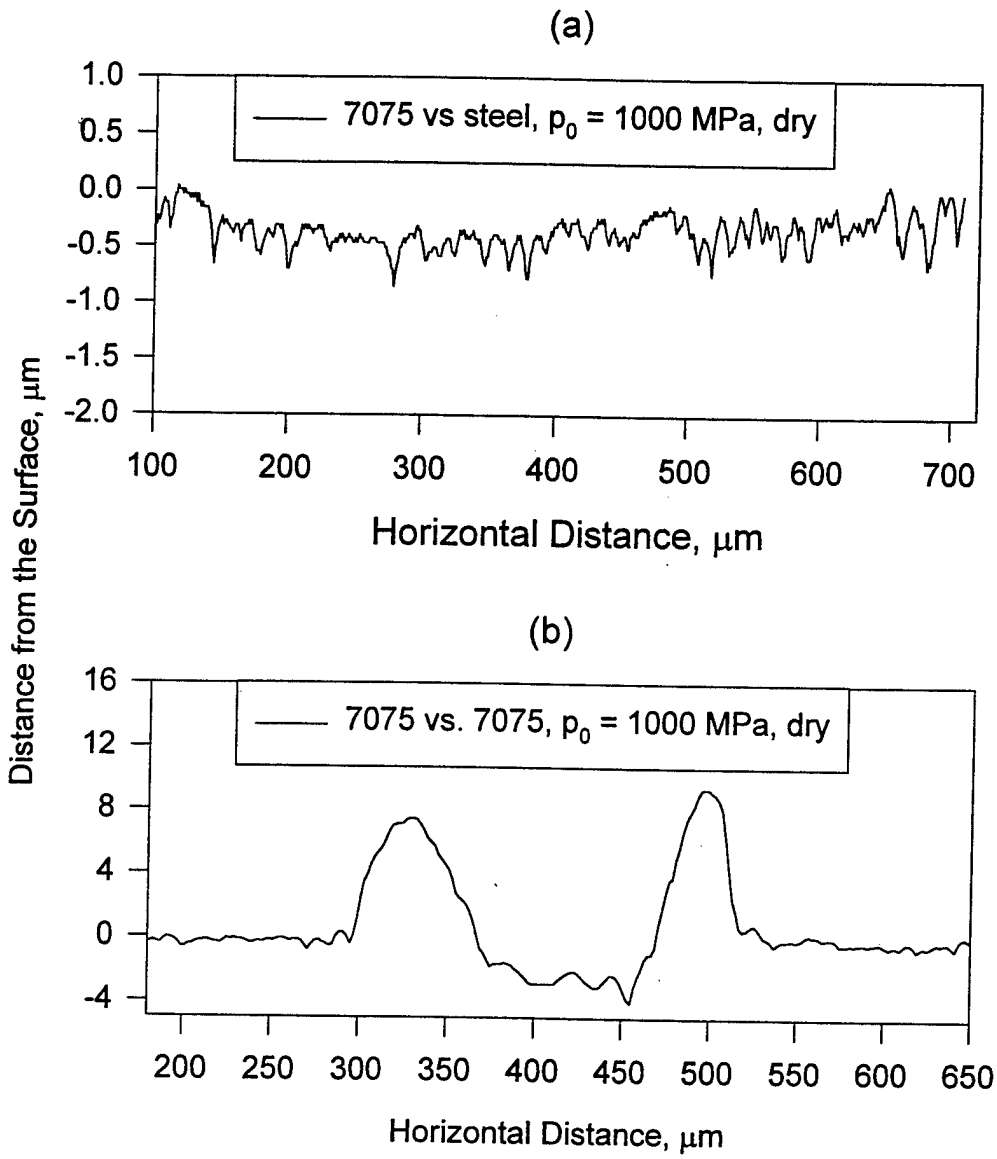

Figure 11 Profilometer traces of 7075-T6 samples after $N = 4\times10^4$ fretting cycles for p_0 = 1000 MPa and δ_t = 10 μm in ambient air: (a) against a steel sphere, showing little wear damage, (b) against 7075-T6 hemisphere, showing severe adhesion occurred.

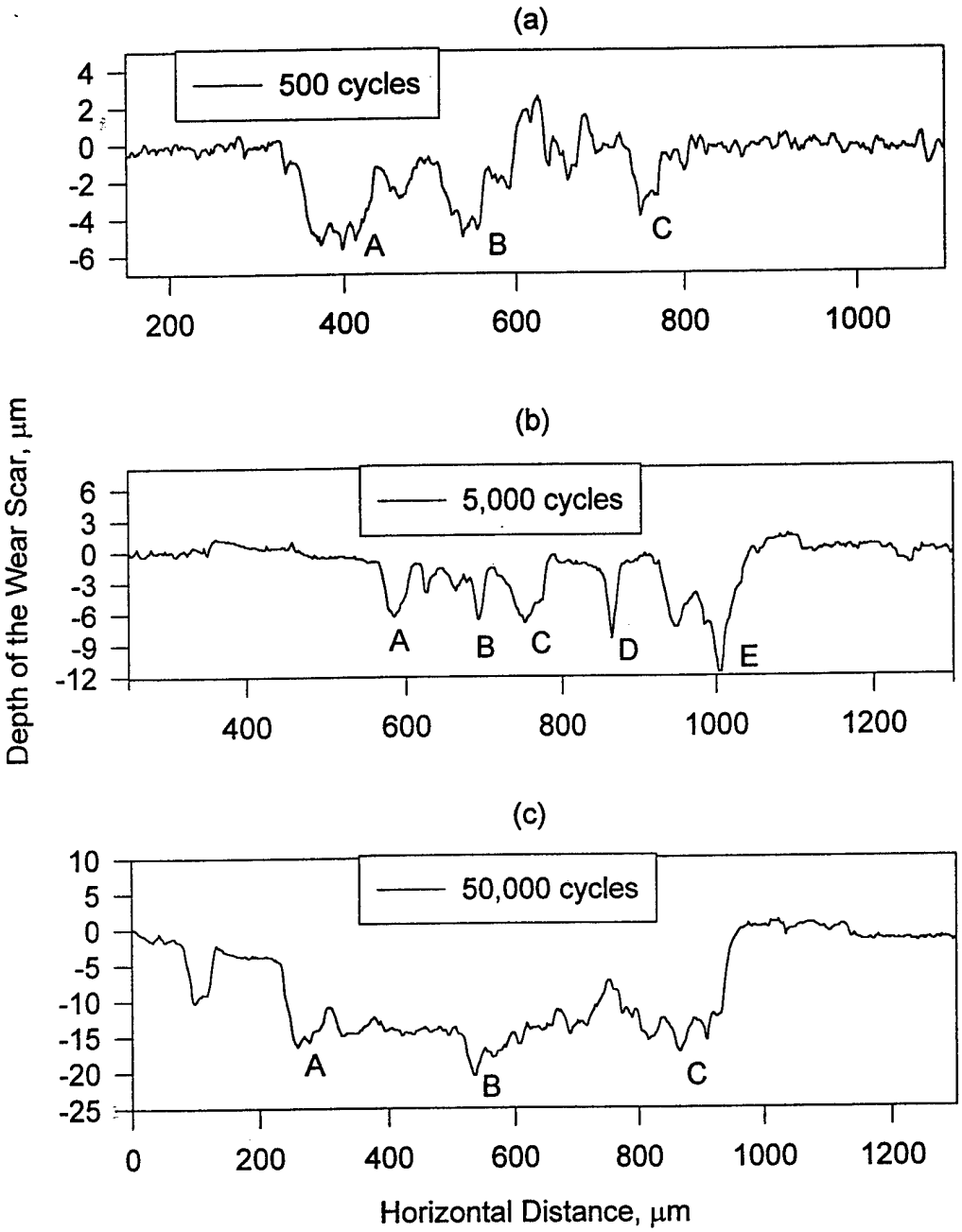

Figure 12 Profilometer traces of cleaned 7075-T6 sample against a steel ball in saline solution after: (a) N = 500, (b) N = 5,000, (c) N = 50,000 fretting cycles, for p_0 = 407 MPa and δ_t = 40 μm.

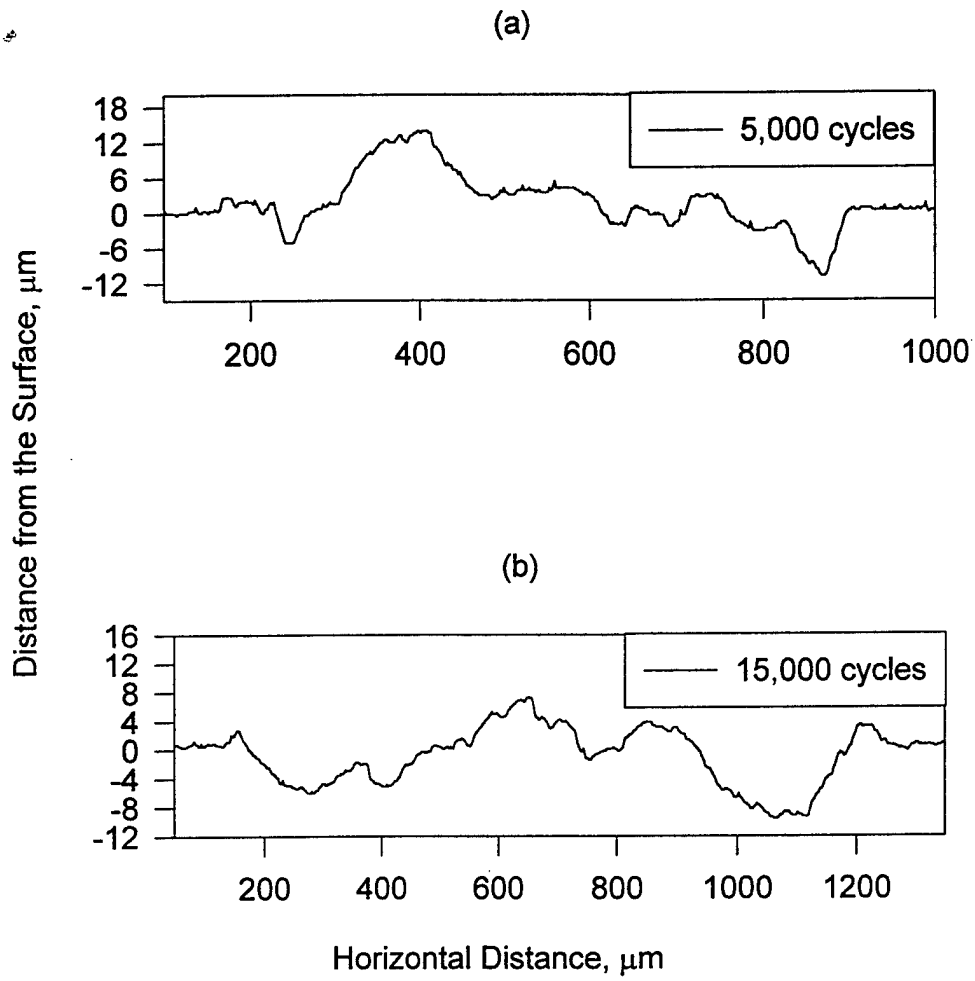

Figure 13 Profilometer traces of cleaned 7075-T6 sample against a steel ball in air after: (a) N = 5,000, (b) N = 15,000 fretting cycles for p_0 = 407 MPa and δ_t = 80 μm.

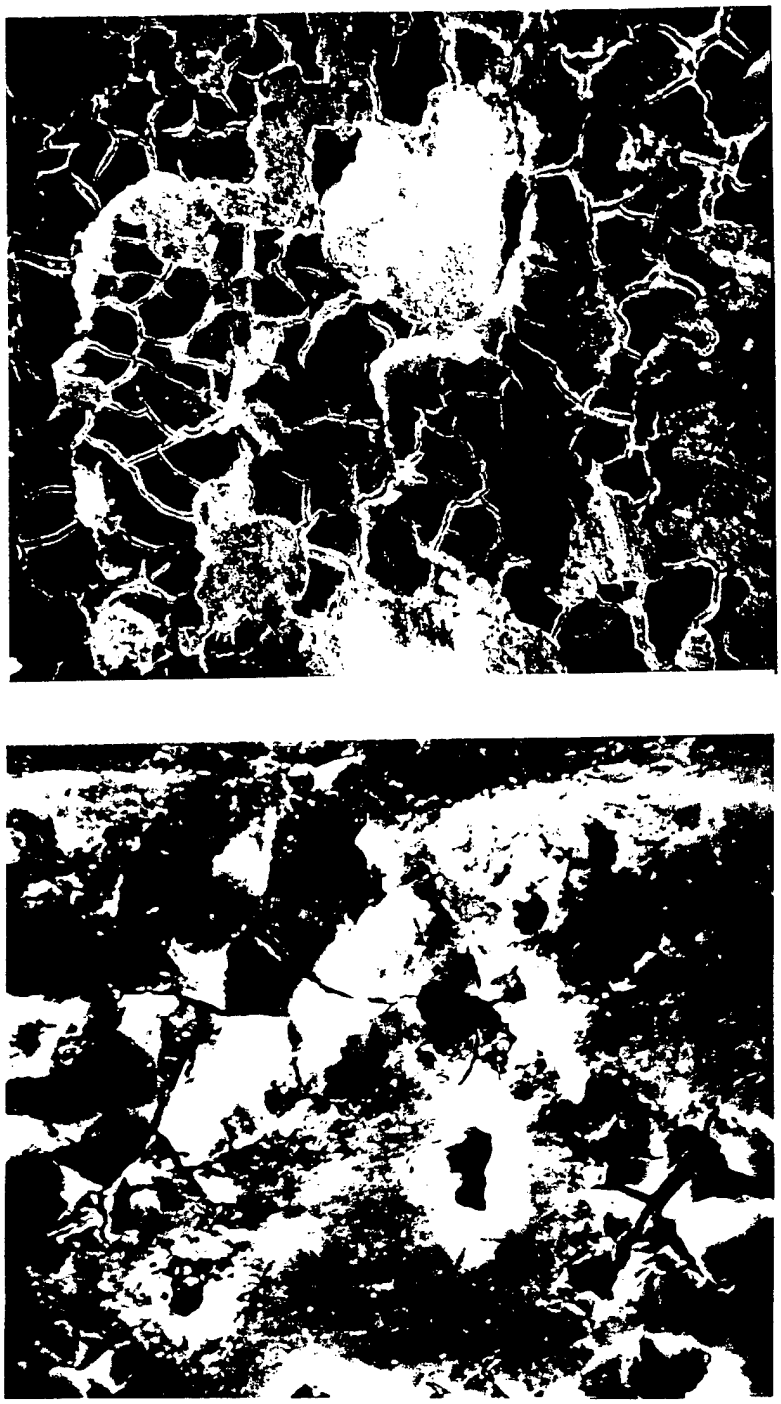

Figure 14 SEM image of high magnification for typical wear scars resulted from fretting 7075-T6 against steel in saline solution, showing (a) pits and cracks initiated from these pits, (b) fish scale-liked morphology and the delamination of the scale.